Printed spark ablation nanoparticle films for microelectronic applications

van Ginkel, H.J.

Important note
To cite this publication, please use the final published version (if applicable).
Please check the document version above.

PRINTED SPARK ABLATION NANOPARTICLE FILMS FOR MICROELECTRONIC APPLICATIONS

Proefschrift

ter verkrijging van de graad van doctor

aan de Technische Universiteit Delft,

op gezag van de Rector Magnificus prof.dr.ir. T.H.J.J. van der Hagen,

voorzitter van het College voor Promoties,

in het openbaar te verdedigen op vrijdag 23 februari 2024, om 12:30 uur.

door

Hendrik Joost VAN GINKEL

Chemisch ingenieur
Technische Universiteit Delft, Nederland,
geboren te Blaricum, Nederland.

Dit proefschrift is goedgekeurd door de

promotor: prof. dr. G.Q. Zhang
copromotor: dr. ir. S. Vollebregt

Samenstelling promotiecommissie:

Rector Magnificus,	voorzitter
Prof. dr. G.Q. Zhang	Technische Universiteit Delft. promotor
Dr. ir. S. Vollebregt	Technische Universiteit Delft, copromotor

Onafhankelijke leden:

Prof. dr. ir. J.M.J. den Toonder	Technische Universiteit Eindhoven
Prof. dr. P.J. French	Technische Universiteit Delft
Dr. ir. M. Tichem	Technische Universiteit Delft
Dr. ir. T.V. Pfeiffer	VSParticle B.V.
Prof. dr. ir. W.D. van Driel	Technische Universiteit Delft, reservelid

Overig lid:

Prof. dr. A Schmidt-Ott	Technische Universiteit Delft

An electronic version of this dissertation is available at
http://repository.tudelft.nl/.

And now for something completely different

Monty Python

CONTENTS

SUMMARY

THIS thesis is about the application and characterisation of spark ablation generated nanoparticles in microelectronics. It opens in chapter 1 with a general motivation of the need for advanced materials and for nanotechnology in particular. It then describes what nanoparticles are and why they are promising materials. Some of their advantages are a high chemical reactivity, a high specific surface area, and the display of quantum effects at that scale. The chapter ends by presenting the research questions and giving the thesis structure.

Chapter 2 provides a technological background for the rest of the thesis based. It describes several applications of nanoparticles within microelectronics not researched during this PhD project: as die-attach materials, chemical sensors, or catalysts. It continues with the description and discussion of several competing nanoparticle synthesis methods and goes in-depth on the theory of spark ablation generation. It describes the effects of various parameters that govern the mass generation rate, particle size, and composition. This theory is important to be able to interpret the results in the other chapters. Impaction deposition is then described in this chapter since it is the method of printing all samples in this thesis. It explains how this method prints dots or lines of nanoparticles, that they have a Gaussian cross-section profile, and how specific deposition parameters affect the deposit. Lastly, the chapter gives a detailed description of the spark ablation synthesis and deposition equipment with which all the experiments in this thesis are performed. The generator, components, gasses, pressures, and materials are all described with diagrams and specifications. Typical synthesis and deposition settings for the generation of Au nanoparticle deposits are given (1 kV, 5 mA, 1.5 L min.$^{-1}$ Ar or N_2 and 1 mm nozzle distance).

The first chapter with results, chapter 3, presents a method to measure the mass deposition rate of the nanoparticle printer. Measuring the mass of microgram scale deposits is challenging due to the high sensitivity required for an accurate measurement. Balances are sensitive to changes in pressure, temperature or humidity that can already give too big errors. One solution already applied in thin film deposition methods is the use of quartz crystal microbalances (QCMs). Their resonance frequency is dependent on their mass, and thus, we can use the frequency shift during deposition to measure a mass change. The Sauerbrey equation that is used for that conversion must be valid, so a special method was developed to comply to all of its conditions. A concentric circular pattern of Au nanoparticles was printed on 10 MHz QCMs to measure the mass deposition rate. It was found that the deposition rate scales linearly with the generation current of the spark, as expected from theory, but also showing the losses in the system are either constant or scale linearly too. The film density was surprisingly constant for all tested synthesis and deposition settings, at 15.95 g cm^{-3}, or a porosity of $\Theta_p = 0.18$. The

density was compared to models presented in literature, and it is proposed that the impaction energy likely compacts the porous structure during deposition until this density is reached. The QCM method can be applied for process monitoring using commercially available equipment and open-source software.

The first applications of printed conducting nanoparticle films are discussed in chapter 4. It describes the conductive properties of such films and the effect of annealing on their conductivity. It was found that an untreated Au film conducts 22 times worse than bulk Au. Several applications are then discussed. Here it was demonstrated that printed Au nanoparticle lines can be applied as interconnect materials as an alternative to wire-bonding. Next, a method was presented to miniaturize the deposits even further by using lithography and lift-off. This reached a line width at the minimum of the lithography equipment available, at 1.2 μm, without significantly changing the nanostructure.

Chapter 5 deals with the application of spark ablation generated nanoparticles as thermoelectric materials. It describes in detail the synthesis and characterization of Bi_2Te_3 nanoparticles and their thermoelectric properties. The main finding was that the thermal conductivity was drastically lower than bulk Bi_2Te_3 and comparable to the state of the art for Bi_2Te_3 nanostructured materials, reaching a minimum of 0.2 W m^{-1} K^{-1} at room temperature. Unfortunately, the electrical conductivity was reduced by at least a factor 1000, easily undoing any efficiency gains from reduced thermal conductivity. Suggestions are given to possibly improve this trade-off. Additionally, this chapter shows how quickly nanostructured materials like the ones in this thesis oxidize after synthesis. From the moment the sample is printed, it gains mass and loses conductivity, so this must be counteracted if a non-noble metal is to be applied.

The final chapter before the conclusions, chapter 6, showcases another application of printed nanoparticles: as UV-sensing material. It shows the results obtained using ZnO nanoparticles to create a UV sensor that is insensitive to visible light. The nanoparticles were deposited over electrodes to fabricate a resistor that has two orders of magnitude electrical resistance reduction when exposed to 265 nm UV light. The response was slow, with 79 seconds to reach 90% of the maximum response and 82 seconds to get back to 10% again. This is attributed to the adsorption and desorption of oxygen under the influence of UV light and can be prevented by packaging the sensor. The contact behaviour between the metal electrodes and ZnO nanoparticles proved to be too unpredictable to reliably create a Schottky diode, which would have had a higher response. This dissertation ends with a list of the conclusions, the answers to the research questions, and finally, some suggestions for future work.

SAMENVATTING

DIT proefschrift gaat over de toepassing en karaterisatie van vonk ablatie gegenereerde nanodeeltjes in micro-elektronica. Het opent in hoofdstuk 1 met de algemene motivatie voor de behoefte aan geavanceerde materialen en voor nanotechnologie in het bijzonder. Er wordt daarna beschreven wat nanodeeltjes zijn en waarom het een veelbelovende klasse van materialen is. Enkele van de voordelen zijn hun hoge chemische reactiviteit, een hoog specifiek oppervlak, en het vertonen van kwantumeffecten op die schaal. Het hoofdstuk eindigt met de presentatie van de onderzoeksvragen en de structuur van het proefschrift.

Hoofdstuk 2 geeft de technische achtergrond voor de rest van het proefschrift. Het beschrijft verschillende applicaties van nanodeeltjes voor micro-elektronica die niet onderzocht zijn tijdens dit promotieonderzoek: als die-attach materialen, chemische sensoren, of katalysatoren. Het gaat verder met een beschrijving en discussie over verschillende concurrerende nanodeeltjes synthese methodes en gaat dieper in op de vonk ablatie generatie theorie. Het beschrijft de effecten van verscheidene parameters die de massa generatie snelheid, deeltjesgrootte, en samenstelling beïnvloeden. Deze theorie is belangrijk om de resultaten in de andere hoofdstukken te kunnen interpreteren. Daarna wordt in dit hoofdstuk impactie depositie beschreven omdat dat de print methode is van alle monsters in dit proefschrift. Er wordt uitgelegd hoe deze methode stippen of lijnen van nanodeeltjes print, dat die een Gaussisch profiel hebben, en hoe bepaalde depositie parameters de depositie beïnvloeden. Als laatste geeft dit hoofdstuk een gedetailleerde beschrijving van de vonk ablatie synthese en depositie apparatuur waarmee alle experimenten in dit proefschrift zijn gedaan. De specificaties en diagrammen van de generator, componenten, gassen, drukken, en materialen worden allemaal gegeven. Typische synthese en depositie instellingen voor de generatie Au nanodeeltjes deposities worden gegeven (1 kV, 5 mA, 1.5 L min.$^{-1}$ Ar or N_2 en 1 mm spuitkop afstand).

Het eerste hoofdstuk met resultaten, hoofdstuk 3, presenteert een methode om de massadepositie snelheid te meten van de nanodeeltjes printer. Het meten van de massa van deposities in de microgram schaal is uitdagend door de hoge gevoeligheid die nodig is voor een accurate meting. Balansen zijn gevoelig voor veranderingen in de luchtdruk, temperatuur, of luchtvochtigheid die al snel te grote meetfouten geven. Een oplossing die al in dunne film depositie technieken wordt toegepast is om een kwartskristal microbalans (QCM) te gebruiken. Die hebben een resonantie frequentie die afhankelijk is van hun massa, dus kunnen we een frequentie verandering tijdens de depositie gebruiken om een massa verandering te berekenen. De Sauerbrey formule die daarvoor gebruikt wordt moet wel toepasbaar zijn, waarvoor een speciale depositie techniek was ontwikkeld om aan alle voorwaarden te voldoen. Een patroon van concentrische cirkels van Au nanodeeltjes werd geprint op 10 MHz kristallen om de massa depositie snelheid te

meten. Het bleek dat de depositie snelheid lineair schaalt met de generatie stroom van de vonk, zoals verwacht uit de theorie, maar dat ook de verliezen lineair moeten schalen of constant zijn. De dichtheid van de films was verrassend genoeg constant voor alle geteste synthese en depositie instellingen, met 15.95 g cm^{-3}, of een porositeit van $\Theta_p = 0.18$. De dichtheid is vergeleken met modellen in de literatuur en het is verondersteld dat de energie tijdens depositie de poreuze structuur van de depositie waarschijnlijk samendrukt tot deze dichtheid is bereikt. De QCM methode is toepasbaar voor proces monitoring via commercieel verkrijgbare onderdelen en open-source software.

De eerste toepassingen van geprinte geleidende nanodeeltjes films worden besproken in hoofdstuk 4. Het beschrijft de geleidende eigenschappen van zulke films en de effecten van verhitting op de geleidbaarheid. Het is bevonden dat een onbehandelde Au film 22 keer minder goed geleid dan bulk Au. Verschillende applicaties worden daarna besproken. Het is gedemonstreerd dat geprinte Au nanodeeltjes lijnen toegepast kunnen worden als interconnectie materiaal als alternatief voor draad-verbinding. Daarna wordt een methode gepresenteerd om de deposities nog verder te verkleinen door gebruik van lithografie en *lift-off*. Een lijn breedte van het minimum haalbare met de beschikbare lithografie apparatuur is succesvol behaald, namelijk 1.2 /mum, zonder significante verandering aan de nanostructuur.

Hoofdstuk 5 gaat over de toepassing van vonk ablatie gegenereerde nanodeeltjes als thermo-elektrisch materiaal. Het beschrijft in detail de synthese en karakterisatie van Bi_2Te_3 nanodeeltjes en hun thermo-elektrische eigenschappen. De belangrijkste vinding was dat de thermische geleidbaarheid drastisch lager is dan die van bulk Bi_2Te_3 en vergelijkbaar met de beste bekende Bi_2Te_3 nanogestructureerde materialen, met een minimum van 0.2 W m^{-1} K^{-1} op kamertemperatuur. Jammer genoeg is de elektrische geleidbaarheid verminderd met ten minste een factor 1000, wat met gemak de efficiëntie winst ongedaan maakt van de gereduceerde thermische geleidbaarheid. Suggesties worden gegeven om deze wisselwerking te verbeteren. Dit hoofdstuk laat bovendien zien hoe snel nanogestructureerde materialen zoals die in dit proefschrift na synthese kunnen oxideren. Zodra het monster is geprint, neemt de massa toe en vermindert de geleidbaarheid, dus dit moet tegen worden gegaan als een niet nobelmetaal toegepast wordt.

Het laaste hoofdstuk voor de conclusie, hoofdstuk 6, toont nog een toepassing van geprinte nanodeeltjes: als UV-gevoelig materiaal. Het laat de behaalde resultaten zien van het toepassen van ZnO nanodeeltjes om een UV sensor te maken die ongevoelig is voor zichtbaar licht. De nanodeeltjes warden gedeponeerd op electrodes om een resistor te maken die twee ordegrootes reductie heeft in de elektrische weerstand onder blootstelling van 265 nm UV licht. De reactietijd was hoog, met 79 seconden om 90% van de maximum respons te bereiken en 82 seconden om terug naar 10% te gaan. Dit wordt toegeschreven aan de adsorptie en desorptie van zuurstof onder invloed van UV licht en kan voorkomen worden door de sensor de verpakken. De aard van het contact tussen de metalen elektrodes en de ZnO nanodeeltjes bleek te onvoorspelbaar te zijn om betrouwbaar een Schottky diode te maken, die een hogere respons zou hebben.

Dit proefschrift eindigt met een opsomming van de conclusies, de antwoorden op de onderzoeksvragen, en als laatste enkele suggesties voor toekomstig onderzoek.

1

INTRODUCTION

Never confuse education with intelligence, you can have a PhD and still be an idiot.

Richard P. Feynman

This dissertation is about nanoparticles: particles thousands of times smaller than the width of a strand of hair. This chapter will introduce nanoparticles, show their potential, and motivate why continued research on their synthesis and applications is needed to solve the challenges of tomorrow. Lastly, this chapter will provide the outline and goals of this thesis.

1.1. MATERIAL SCIENCE AS THE DRIVER FOR TECHNOLOGY

IN our highly technology dependent society, innovation is the main driver for economic growth. Modern society is always looking for better products with increased performance at a lower cost that are at the same time more sustainable and safer. We desire more efficient solar panels, more battery capacity, reduced rare metal use, smaller and faster electronics, faster wireless networks, stronger materials, more durable coatings, less waste production, and much more, all while getting cheaper and more reliable. Continuous technological innovation on many fronts is required to meet these demands.

One scientific field that is at the basis of many products is materials science: the study of how materials work and how they can be improved or adapted for specific applications. From consumer electronics to quantum computing and from greener industry to space exploration, all modern and future technologies require advanced materials to improve or become a reality. As a consequence, the demands on new materials are increasing: Materials need to do more, last longer, be stronger, cheaper, or even have capabilities never seen before. Unsurprisingly, this pushes the limits of what conventional materials, like bulk metals, polymers, and composites can do. To engineer new materials, greater control over material composition, (micro-)structure, and topography is required.

An approach to gain this level of control is to look at materials at the smallest size domain: the nanoscale. At the nanoscale, the laws that govern a material's properties behave differently, and remarkable phenomena emerge that can differ drastically from their macroscale counterparts. This created the field of nanotechnology and has led to the discovery of materials with enhanced performance or unique properties that cannot even exist in bulk materials. Nanotechnology is a diverse field with applications in almost every engineering discipline, but in this thesis, we will limit ourselves to nanoparticles, particularly for use in microelectronics.

The microelectronics field is the foundation of the digital age we live in. We are surrounded by microelectronic devices and a world without them has become unthinkable. Ever since the invention of the transistor and the integrated circuit (IC), there has been an unrelenting drive to increase computational power and keep up with the famous Moore's law: the number of transistors on an IC will double roughly every two years. [1] The semiconductor industry has since kept up with Moore's prediction by exponential miniaturization of microelectronic devices. At some point (some claimed it has happened already), Moore's law must reach fundamental limitations and finally come to an end. When this happens, the performance of a chip is still expected to improve through improved device design, material performance, or by adding more functionality. This last approach concept has become known as the "More than Moore" approach. More than Moore devices cannot only compute using digital ICs but also sense or interact with the environment or have their own power source. Miniaturized sensors, transducers, and actuators must be developed to enable this, which we call "microelectromechanical systems" or MEMS. Fabrication of MEMS requires innovative microfabrication methods and advanced functional materials, and nanomaterials are one of the possibilities. Nanoparticles can, for example, be used as sensing material or for generating or stor-

ing electricity. Besides adding functionality to a chip, nanomaterials can also be used for more advanced packaging of chips. Increased miniaturization and functionalization require advanced packaging solutions to connect the chip to a circuit board, enable 3D integration of chips, or expose a device to the environment it is meant to interact with. Nanoparticle-based solder alternatives and interconnect materials are therefore investigated, as well as nanoparticle printing for additive manufacturing on microchips.

1.2. WHAT ARE NANOPARTICLES AND WHAT CAN THEY DO?

One of the first reports on nanoparticles was by Michael Faraday in 1857, who described that the liquid he used to make gold leaf thinner became red and noted that light was being scattered by the liquid. [2] He concluded the gold had to be suspended in the liquid, even though the particles were not visible with his instruments. Amazingly, his solutions are still the same ruby red colour as when he created them and are on display at The Royal Institution in London. Faraday's experiment shows the surface plasmon resonance effect. This phenomenon gives gold nanoparticles a specific colour depending on their size. One of the many remarkable properties of nanoparticles.

Since Faraday's discovery, many types of nanomaterials have been discovered: nanoparticles, nanowires, nanorods, and nanosheets, to name but a few. They are made of metals, ceramics, pure carbon or organic (soft) matter. The amazing diversity in composition, shape, size, and structure creates endless materials to investigate. The term "nanoparticle" was first coined in the 1970s, but research on them only really took off in the late 90's, as shown in Figure 1.1. The catalysts of this growth were the advancement of electron microscopy and other characterization techniques and the continued development of new, improved synthesis methods at the end of the 20th century that enabled scientists to easier observe and measure nanoparticles. Since then, an explosive growth of nanoparticle research has taken place, to which this work is a humble contribution.
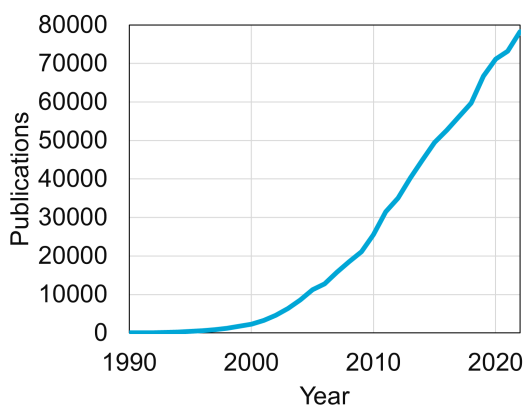
Figure 1.1: Yearly journal publications with *nanoparticle(s)* in their title, abstract or keywords.[3]

A nanoparticle is defined as a particle with all size dimensions below 100 nm.[4] The

composition and structure are not defined, but the research in this thesis is primarily concerned with spherical metal or metal-oxide nanoparticles below 20 nm in diameter. It is at this size range that the peculiar size-dependent properties of these materials become apparent. Nanoparticles have three causes for their remarkable properties: due to quantum mechanical effects, due to the low binding energy of their surface atoms, and due to their geometry. Starting with the latter, their surface-to-volume ratio is incredibly high. Five nm golden nanoparticles, for example, have a surface area of 62 m^2/g, while 1 mm golden particles have a surface area of only 0.00031 m^2/g, two hundred thousand times less! High surface-to-volume ratios are desired when as many surface atoms as possible must be active or accessible. This reduces the amount of material needed in application areas such as catalysis or chemical sensing, which is especially important when using expensive or rare metals. A nanometer scale particle is also able to travel through the bloodstream and into cells, which makes them interesting for medical applications such as drug delivery, imaging, or thermal treatment. [5–8]

Besides such geometric advantages, some thermodynamic size effects also play a role. The surface of a nanoparticle consists of weekly bound surface atoms due to the surface curvature and the low coordination number of a surface atom. Surface atoms are therefore mobile, which reduces the melting point of a nanoparticle. The melting point of gold nanoparticles can get as low as 526 °C for a 2.5 nm diameter nanoparticle, roughly half of that of bulk gold. [9] Soldering material can then be made out of metals that would normally have too high melting points. At the nanoscale, uncommon crystal structures can also become favourable, or strange surface layers can form on the particle, opening up new and exciting chemistry. Black titania (TiO_2), which is normally a common white pigment, is one example. [10]
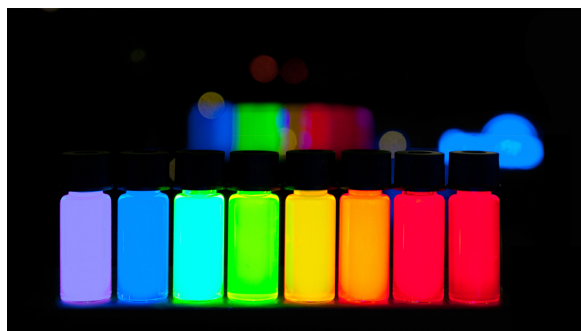
Figure 1.2: A selection of illuminated quantum dots suspended in water exhibiting photo-luminescence. Nanoparticle size increased from purple to red. [11]

The combination of mobile atoms and high surface area makes nanoparticles highly reactive. For example, an unprotected metal particle will almost instantly react with any oxygen available to form its metal oxide. Increased reactivity combined with the increased active surface area makes nanoparticles ideal catalysts. Catalysis is, therefore, one of the oldest applications for nanoparticles, where they have been applied commercially for years. The best example is catalytic converters in cars, which convert the

harmful exhaust gasses into non-toxic and safer compounds, primarily water (H_2O) and carbon dioxide (CO_2). The catalysts inside these catalytic converters are nanoparticles of platinum (Pt), palladium (Pd), or rhodium (Rh), and they are fixed on a porous ceramic carrier through which the exhaust gas flows.

Lastly, quantum size effects give rise to properties that are very different or even absent in the bulk phase. Nowhere is this as clear to see as in quantum dots (e.g. CdSe). Due to their size, they confine electrons in such a tiny space that quantum confinement occurs. This effect makes the band gap discrete and dependent on the nanoparticle size. When an electron in a quantum dot is excited by visible light, it can jump to the conduction band and when it decays back to the valance band, emit light in a process called photo-luminescence. Since the band gap depends on the particle size, it is possible to tune the wavelength of this emitted light by changing the nanoparticle diameter. A smaller particle has a bigger band gap and will emit lower wavelength light. Quantum dots such as the ones in Figure 1.2 are now used in "QLED" TVs to improve the range of available colours.

1.3. THE CHALLENGE OF NANOMATERIALS RESEARCH

Faraday's nanoparticle suspension is also an example of quantum effects, in this case, surface plasmon resonance, which changes the particle's colour depending on its size. By tuning the particle size, one can thus change its properties to fit a specific application. Additionally, by playing around with composition, an endless range of engineered nanomaterials can be created to perform optimally for their application. The enormous possibilities this creates for research directions make it necessary to narrow down the application areas to research. Once an application is chosen to research, one must design the ideal nanoparticle and find a way to apply it commercially. The problem is threefold:

- What is the ideal nanoparticle for this application?

- Can you make it, and how?

- How can you successfully apply this nanoparticle?

The first question is mostly answered by literature research and serves only to define an end goal and desired material properties. Unfortunately, it is usually impossible to make the ideal material because compromises are often unavoidable. There can be conflicting properties (i.e. improving one diminishes the other), fundamental limitations (e.g. physical limits or chemical instability), or synthesis problems (e.g. dangerous processes or extreme conditions). Even when it is possible to overcome these problems, it might not be economically viable. Economic factors like raw material costs, equipment costs, time, or energy requirements can make it entirely impossible to commercialize or even research a material.

A sensible approach is to reverse these three steps and find a cheap, scalable, and safe process. With such a process, you can make a range of potential materials and develop them for specific applications. The second question is then already partially answered and becomes more about optimizing the material and synthesis parameters rather than developing an entirely new process. The third question is now the main focus of a new

1

research project. Application of the material might require some additional processing steps, device design, or some fine-tuning of the synthesis and deposition process and equipment. If a potential application is found and the ideal particle is defined, it becomes an engineering challenge rather than a fundamental scientific problem.

One method to create and deposit nanoparticles in a single production step is spark ablation combined with an impaction printer. Spark ablation generation uses a repeating spark between two opposing metallic electrodes to create a metallic vapour. The supersaturated metal vapour quickly cools down and crystalline nanoparticles form which are carried away by a carrier gas. Spark ablation was invented as a synthesis method in the 80's but has recently been commercialized, initially aimed at the catalysis and chemical sensing markets. [12, 13] However, its combination with impaction printing with a sub-millimeter resolution creates opportunities to use this technology in microfabrication to create functional layers or printed electronics. The high purity of the produced nanoparticles and the complete absence of any chemicals in the synthesis or deposition step allows this production method to be directly inserted in a microfabrication process.

1.4. SCOPE AND OUTLINE OF THIS THESIS

The aim of this thesis project was to investigate the applicability of spark ablation generated nanoparticles in microelectronics. Such a wide research topic requires narrowing down of research areas, and in the end, a few topics were selected to study, and corresponding research questions were formulated:

1. What is the effect of the nanoporous structure on the electrical and thermal properties of a nanoparticle film?

2. Are printed nanoparticle lines applicable as interconnect materials?

3. Can we use semiconductor nanoparticles for thermoelectric or opto-electronic devices?

To answer these questions, a better understanding of nanoparticle films is required. Chapter two describes the synthesis technology central in this dissertation: spark ablation. Both nanoparticle synthesis and deposition are discussed to provide a basis for understanding the rest of the chapters. The next chapter describes a novel method to determine mass deposition rate, density, and porosity. This is needed to be able to quantify the porosity and discuss the effect it has on the properties of the deposit. It deals with using quartz crystal microbalances to determine the mass deposition rate and, by extension of that, the density of a nanoparticle deposit. The rest of the thesis demonstrates some application areas where spark ablation generated nanoparticles can be applied within the field of microelectronics.

Chapter four discusses the use of metal nanoparticles for printed electronics and interconnects. It shows some applications of printed conducting lines and how they perform. It also presents a method to miniaturize the nanoporous film patterns further if the resolution limit of the printer is reached. Chapter five demonstrates the possibility of creating nanoparticle films with a reduced thermal conductivity compared to their macroscale counterpart. This is demonstrated in thermoelectric nanoparticles for

1

energy harvesting. The last application chapter, chapter six, deals with wide band-gap semiconductor nanoparticles for UV photo-detection and shows the properties of such functional devices and the potential for UV sensors. Finally, the conclusions of this thesis are summarized and recommendations for improvement and further research are given.

REFERENCES

[1] G. E. Moore, *Cramming more componentsonto integrated circuits,* Electronics Magazine **38** (1965).

[2] M. Faraday, *X. the bakerian lecture. experimental relations of gold (and other metals) to light.* Philosophical Transactions **147,** 145 (1857).

[3] www.scopus.com, *Publications on nanoparticles(s) per year,* scopus.com (2022), online.

[4] *ISO TS 80004-2,* (2015).

[5] A. Z. Wilczewska, K. Niemirowicz, K. H. Markiewicz, and H. Car, *Nanoparticles as drug delivery systems,* Pharmacological Reports **64,** 1020 (2012).

[6] K. Ulbrich, K. Holá, V. Šubr, A. Bakandritsos, J. Tuček, and R. Zbořil, *Targeted drug delivery with polymers and magnetic nanoparticles: Covalent and noncovalent approaches, release control, and clinical studies,* Chemical Reviews **116,** 5338 (2016).

[7] A. Banstola, F. Emami, J.-H. Jeong, and S. Yook, *Current applications of gold nanoparticles for medical imaging and as treatment agents for managing pancreatic cancer,* Macromolecular Research **26,** 955 (2018).

[8] M. Johannsen, U. Gneveckow, K. Taymoorian, B. Thiesen, N. Waldöfner, R. Scholz, K. Jung, A. Jordan, P. Wust, and S. A. Loening, *Morbidity and quality of life during thermotherapy using magnetic nanoparticles in locally recurrent prostate cancer: Results of a prospective phase i trial,* International Journal of Hyperthermia **23,** 315 (2007).

[9] P. Buffat and J.-P. Borel, *Size effect on the melting temperature of gold particles,* Physical Review A **13,** 2287 (1976).

[10] X. Chen, L. Liu, P. Y. Yu, and S. S. Mao, *Increasing solar absorption for photocatalysis with black hydrogenated titanium dioxide nanocrystals,* Science **331,** 746 (2011).

[11] Antipoff, *Quantum dots with emission maxima in a 10-nm step are being produced at plasmachem in a kg scale.jpg,* (2022).

[12] S. Schwyn, E. Garwin, and A. Schmidt-Ott, *Aerosol generation by spark discharge,* Journal of Aerosol Science **19,** 639 (1988).

[13] A. Schmidt-Ott, *Spark Ablation: Building Blocks for Nanotechnology*, 1st ed., edited by A. Schmidt-Ott (Jenny Stanford Publishing, 2020).

2

NANOPARTICLE APPLICATION IN MICROELECTRONICS AND THEIR SYNTHESIS

Whenever you face a man who's playing your instrument, there's a competition.

Wynton Marsalis

We start this chapter with a short description of some relevant applications within micro-electronics. Before diving into spark ablation theory, other nanoparticle synthesis methods are described and compared. To better understand the other chapters in this dissertation, it is necessary to provide a good description of spark ablation and the setup that was used. This chapter aims to provide this background knowledge as well as the fundamentals of impaction deposition, the central deposition method in this dissertation. Lastly, a detailed description of the nanomaterial printing setup is given with which all samples in this dissertation have been made.

2

2.1. NANOPARTICLE APPLICATIONS IN MICROELECTRONICS

L ET us first identify application areas of interest for nanoparticles. A few applications have been briefly mentioned already in the previous chapter, but these are not necessarily of interest to this dissertation. The focus here is on microelectronics and microelectromechanical systems (MEMS), so we will not discuss applications in other fields. Applications that are delved deeper into at a chapter in this thesis will also not be discussed here but in the corresponding chapter.

DIE ATTACH MATERIALS

The first major application in microelectronics is the use of nanoparticles as a die attach material. Here, the ability of nanoparticles to sinter or even melt when heated to <200 °C is used to create a low-temperature solder alternative. [1, 2] Once sintered, the temperature required to melt the connection is that of the bulk metal, making the bond irreversible. [3] Currently, this application is being commercialized using silver nanoparticle pastes due to their excellent electrical and thermal properties, and resistance to oxidation. [4] Copper would, however, be preferred due to its good thermal and electrical conductivity but much lower price. Cu paste formulations are commercially available but have not found commercial applications yet. [1, 5] One major challenge faced with commercializing this technology is that the particles do not fully melt but sinter. This leaves many grain boundaries and voids in the final film that form mechanical weak points. A second hurdle is oxidation. As mentioned previously, nanoparticles are prone to oxidize and require protection. This requires paste formulation with reducing agents or surfactants to extend the shelf life or oxygen-free production and application environments.

CHEMICAL SENSING

There are many reasons to develop more sensitive or selective sensors to detect certain chemicals in the air or liquids: safety, process control, air quality monitoring, or research. Many sensors are based on adsorption or (reversible) reactions with the sensing layer. The interaction changes the electrical or optical properties of the sensor which are detected. More available surface area means more molecules can adsorb or react with the surface, giving a stronger signal. Increasing surface area could be done by making a larger sensor, but it is both more economical and practical to make smaller sensors. Miniaturization requires a sensing material with a high surface-to-volume ratio, so nanoscale materials are popular material classes to achieve this. [6] Semiconducting metal oxide nanoparticles (e.g. SnO_2, TiO_2, ZnO) are promising candidates for use in gas sensors because they have high sensitivity, can be synthesized from cheap raw materials and have good chemical and thermal stability. [7]

The increased miniaturization of chemical sensors has moved research closer to microelectronics. Adding chemical sensing capability to microelectronic devices enables high sensor and readout electronics integration levels, resulting in more power-efficient sensors and integrated sensor arrays. Nanoparticle or nanostructuring methods compatible with microfabrication are needed to functionalize these sensors.

CATALYST PARTICLES

Another benefit already discussed before of nanoparticles is as a heterogeneous catalyst. Heterogeneous catalysts increase the reaction rate of chemical reactions on their surface without being consumed, such as the catalytic converter in cars. A high specific surface area increases the amount of available catalytic sites and, thus, the reaction rate. In the context of microelectronics, catalytic nanoparticles are used as catalyst layer to grow carbon nanotubes (CNTs) [8], inorganic nanowires [9, 10], or in microreactors [11–13]. The first two applications use them to grow the actual functional material. Easy methods to deposit nanoparticles evenly on a substrate can ease localized 1D material synthesis. Microreactors are miniaturized chemical reactors to synthesize a chemical locally. This is interesting for biomedical lab-on-a-chip applications to analyse a sample or to synthesize microscopic amounts of a drug or chemical.

2.2. NANOPARTICLE SYNTHESIS METHODS

In the past decades, many synthesis methods have been developed for many types of nanoparticles. In this section, we will focus on methods to synthesise metal, metal oxide or ceramic nanoparticles since they are the subject of this dissertation. The chart in Figure 2.1 gives an overview of several available nanoparticle synthesis methods to synthesize metal or ceramic nanoparticles. There are more ways to synthesize nanoparticles that are not included here because of their limited use or inability to synthesize the nanoparticles of this thesis. The methods can be separated into two main categories: physical and chemical methods. We will first discuss the latter since that is the most common, traditional way of making nanoparticles.

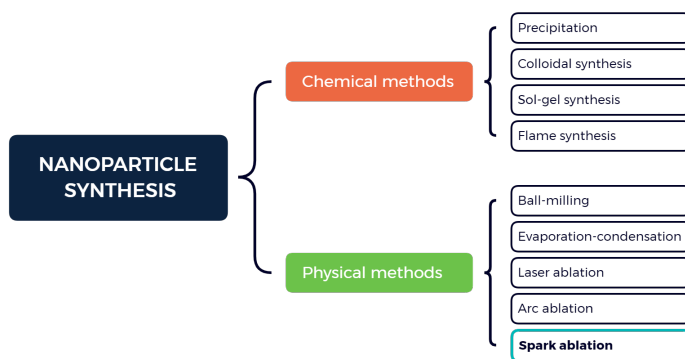Figure 2.1: A chart showing the methods to synthesize inorganic nanoparticles.

2.2.1. CHEMICAL METHODS

Wet chemical methods use chemical reactions to build a nanoparticle. The precursors that are used for that are often salts or metal-ligand complexes. [14–16] Although good control over particle size and composition has been achieved over the years, wet chemical methods have several fundamental drawbacks:

2

- Every new composition or material requires the development of a new recipe or synthesis process. New recipes can take weeks to months to develop, severely increasing development time.

- Extensive purification is often required to use the particles after synthesis. This, in turn, requires many costly process steps and creates a large chemical footprint.

- Nanoparticles are generated in a solution with surfactants and, therefore, always have an unclean surface. One must remove such surfactants or contaminants to use pure particles or accept limited access to the nanoparticle surface.

Most chemical methods are batch-wise production which makes them reasonably scalable. Still, their lack of flexibility and limitation to liquid-based methods is a serious drawback for material screening, high-purity applications or particle surface modifications.

There are many different chemical synthesis routes, but most can be categorised in one of these categories:

- Co-precipitation

- Colloidal synthesis

- Sol-gel synthesis

- Flame aerosol synthesis

Co-precipitation
The simplest nanoparticle synthesis technique is possibly that of co-precipitation. Here, two or more reactants are added to a solvent, react, and yield an insoluble product that will precipitate. The product is then separated from the reaction mixture by centrifugation and washing or filtration. Reactions are usually redox, where the metal ions in the liquid exchange electrons with a second ion and are reduced or oxidised. It is possible to create salts (e.g. $AgCl$) or oxides (e.g. $CoFe_2O_4$) this way. Size control, and to a lesser degree, shape control, can be achieved by tuning the reaction conditions.

Colloidal synthesis
In many ways, colloidal synthesis is similar to a regular precipitation reaction. The key difference is that the reactions in colloidal synthesis need a catalyst and have added surfactants to keep the particles suspended and for better control of the reaction. The basis of colloidal synthesis is adding the metal precursors and a catalyst to a solvent and letting the chemical reaction create nuclei that grow until no reactant is left or the reaction is stopped. The product is a suspension of nanoparticles with surfactants in a liquid: a colloid. This method can create nano-sized crystals (nanocrystals) of sizes between atomic clusters and several hundred nanometers.

The greatest advantage of this method is the high degree of control over particle size, composition, and even shape. Nearly monodisperse size distributions can even be obtained. By choosing the right reaction conditions, one can control the growth process and stop it at the desired moment. This is also one of its biggest downsides; the

reactions are very sensitive to small changes and scaling up can thus be a challenge. Key control parameters are temperature, atmosphere (pressure, composition), catalyst, and, most importantly, the reactants. These reactants are metal-organic complexes (e.g. $[Ag(NH_3)_2]^+$) or metal salts (e.g. $AgNO_3$). Especially the complexes can be highly sensitive to oxidation and require oxygen-free glove boxes and specialised glassware to keep the entire process oxygen-free. Another disadvantage is that the nanoparticles are suspended in the liquid and require several cleaning and purification steps to remove leftover reactants and impurities from the reaction mixture. Besides the additional time and work this needs, purification creates large waste streams of solvents and potentially harmful chemical compounds.

Colloidal synthesis is the main pathway to synthesising photoluminescent quantum dots such as in Figure 1.2 (e.g. CdSe, InP) [16] and perovskite nanocrystals (e.g. $CsPbI_3$) [17] and nanoparticle of particular shapes (cubes or stars).

SOL-GEL SYNTHESIS

Like the name implies, sol-gel synthesis refers to the class of methods that have a solution ("sol") that forms a gel in which a solid will crystallise. It is a widely used commercial process for the production of fine powders of silica, titania and many other oxides. [18] The process has four steps [15]:

1. Hydrolysis of metal precursors to start the reactions

2. Gel formation (or condensation) where the polymer reacts to form a network.

3. Liquid removal (drying or ageing) to make the gel denser or precipitate the solid fraction.

4. Calcination (firing) to remove any organics and water and create a dry powder or porous solid.

Sol-gel processes are popular due to their simplicity and scalability. The reactions are easy to control and require no complex equipment. The calcination step can be done in a simple oven. Another benefit is that this method can be performed on a substrate to have a thin film on a substrate after calcination. [15, 18] Particle sizes start at several nanometers. The main limitation is that due to the calcination step, all metals will oxidise, limiting it so oxide particles. Additionally, doping or complex compositions are hard to make, because of the complex chemistry during gelation.

FLAME AEROSOL SYNTHESIS

Flame aerosol synthesis is the name of a set of methods that employ a flame to burn reactants. Here, precursors and possibly a fuel for the flame are mixed, aerosolised and combusted in a controlled flame. During the combustion process, the reactants are heated and oxidised, and a nanoparticle or agglomerate forms. The resulting aerosol can then be further treated to become dense particles or left as nanostructured agglomerates.

We can distinguish two types of flame syntheses: vapour-fed and liquid fed. Liquid-fed can then be further divided between flame assisted (with an external flame to provide the heat) and flame spray pyrolysis (where the liquid precursors also provide the fuel for

2

the flame). [19, 20] The first method is a the dominant industrial process for the production of carbon black, silica, and titania, with production volumes of over several megatons per year. [21] Carbon black has been produced by burning organic compounds for millennia, but was industrialised during World War II for rubber filler. [20] Shortly thereafter, new formulations were discovered to create many oxide powders.

The main benefit of this method is the scalability and low cost. A reactor needs only a flame and well controlled gas or liquid feed. There is decades of industrial expertise available and production of the simplest oxide powders (e.g. SiO_2, TiO_2, Al_2O_3) are mature processes. Due to the high temperature combustion of the precursors, oxidation can not be avoided and indeed, only oxides are made this way. Secondly, the product has a large size distribution and a high degree of agglomeration. For advanced material applications, this can problematic, but as catalyst carrier, or filler material, this is no issue.

2.2.2. PHYSICAL METHODS

Physical methods do not use chemistry to create a particle from a solution but use electricity, heat or mechanical force to create nanoparticles. The main advantage of using physical processes is the (almost) absence of chemicals. This greatly reduces waste streams, reduces process complexity and allows for higher purity particles. This purity has the drawback that the particles agglomerate and are extremely reactive. [22, 23] Secondly, the processes have only one or a few process steps which reduces process variables and makes screening materials easier. The disadvantage is that you have less control over the particle shape. In this section, we will discuss the most popular physical methods: ball milling, laser ablation, and arc ablation. Spark ablation has its own section because of its central role in this dissertation.

HIGH-ENERGY BALL MILLING

The oldest and simplest way of making a powder is by grinding a material down to dust. In the kitchen, you might use a mortar and pestle to create a fine powder or paste out of your spices. When you want to make nanoparticles, however, much finer milling is needed. Ball milling uses hard ceramic balls inside a rotating chamber to mill a powder to nanopowder. Depending on the mass and speed of the balls, temperature and duration of the milling, one can choose a final size. In its simplest form, ball milling will only create nanoparticles of an existing solid bulk material. When adding two materials to a ball milling machine, the two will mix over time and form an alloy or compound. The distribution of the two materials will be different per particle, but the whole powder will have an average composition identical to the starting mixture. [24–26]. Ball-milling can be done in high purity or reactive conditions to make, for example, oxides or nitrides. [27] It has the advantage that it results in milligram to gram quantities of the material after each batch, but each batch can take days to mill.

EVAPORATION-CONDENSATION

The following methods are gas based aerosol generation methods and work with fundamentally the same mechanism:

1. Creation of supersaturation in the gas phase due to evaporation of a metal

2. Nucleation due to cooling of the gas

3. Nanoparticle growth by metal condensation and coagulation

Evaporation of a metal can be achieved by resistive heating or through an external heat source. The vapour coming from such a metal, such as in a glowing wire generator [28], is carried away by a cool, inert gas flow. The rapid temperature drop causes nucleation and further growth of the nuclei. The aerosol is then carried away to deposition or analysis equipment or to further processing equipment (e.g. for annealing or coating). The metal particles can be oxidized when oxygen is present in the carrier gas. [23]

Generation rates using the evaporation of a heated bulk metal are low due to the low vapour pressures of most metals and high energy requirements to heat the metal to regularly above 1000 K. [23, 29, 30] To reach commercially viable production rates, better methods have been developed to create supersaturated metal vapours. To reduce energy consumption, it would be much more efficient to only heat a small part of the parent metal instead of the whole block or wire. The next methods do exactly that by ablating the material with a local, powerful heat pulse.

LASER ABLATION
Laser ablation uses a pulsed or continuous laser to ablate a metal locally. Similarly to other vapour condensation methods, it works on all metals, but also non-conductive and high melting point materials since temperatures can locally exceed 10000 K. [30, 31] Production rates are in the order of grams per hour for a high power laser. [31] Although it is a versatile and powerful method, the major drawback of laser ablation is the requirement of the high-power laser, which makes scaling up expensive and energy intensive.

ARC ABLATION
Arc ablation and spark ablation use essentially the same phenomenon to ablate metal: a high-power electrical arc. The difference is primarily in that arc ablation uses a continuous arc, while spark ablation has short, pulsed arcs called sparks. Production rates of arc ablation are therefore drastically higher than spark ablation, with reported production rates in the order tens to hundreds gram per hour, at a cost of several kWh per gram. [4, 32, 32] This high production rate makes it harder to control the size, and high degrees of agglomeration are the norm. Arc and spark ablation are somewhat complementary, where arc ablation is better suited for fast production larger nanoparticles (> 20 nm), while spark ablation allows for smaller particles with better control over the composition.

2.3. SPARK ABLATION
The central technology used in this thesis is spark ablation. This section provides a suitable overview of spark ablation for readers of this dissertation, but a complete and extensive overview of the technology can be found in the book of Andreas Schmidt-Ott. [33] The method was first described in 1988 by Schwyn, Garwin and Schmidt-Ott [34], but was not commercialized until recently. The first publication already mentioned its ability to produce 1 nm particles. Initially designed to create a synthetic soot aerosol, spark

ablation has now been demonstrated to work for a wide range of (semi-)conducting materials: metals, oxides, alloys, and ceramics.
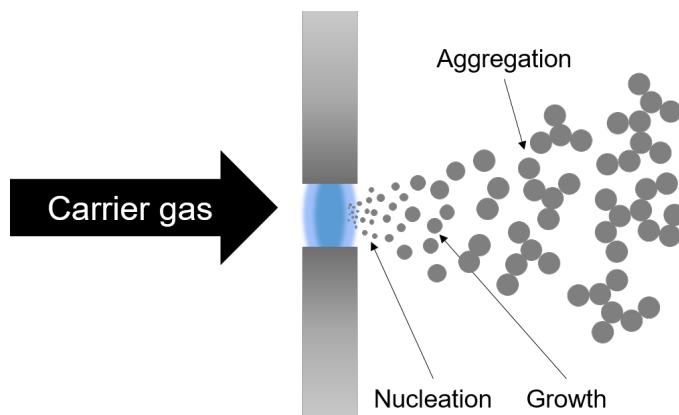
2.3.1. WORKING PRINCIPLE

Figure 2.2: Schematic drawing of spark ablation showing the evolution of the nanoparticles in the reactor chamber.

As drawn in Figure 2.2, spark ablation uses two opposing metal electrodes placed roughly 1 mm apart in a leak-tight chamber at atmospheric pressure. A short ($< 10\mu s$) electric spark ionizes the gas and ablates some material from the electrodes that will rapidly cool down in the carrier gas that flows around the electrodes. During this ultrafast quenching (from 20000 K to room temperature), nuclei form that continue to grow by condensation and later coalesce into nanoparticles below 20 nm in diameter. [22, 33, 35] This sequence repeats itself at a frequency of several hundred Hz, depending on settings. [22, 36] The eventual product is a particle with the same average composition of the electrodes they originate from with a log-normal size distribution. [22, 36] When they have reached their final size and stopped coalescing, the nanoparticles will aggregate and eventually form larger agglomerates. The size distribution and production rate depend on the electrode materials, gas composition and flow, and the spark energy (see section 2.3.1).

A short spark has the advantage that each spark can have approximately the same energy and contains the same amount of ablated material. This gives good control over the ablation process, so spark ablation can consistently produce an aerosol with the same size distribution and composition. Furthermore, the short spark duration prevents the electrodes from becoming so hot that evaporation effects influence the ablation rate or composition when using two different electrodes.

As mentioned above, the ablation occurs by the discharge of a high-voltage spark that creates a plasma. The generators are hence often called spark discharge generators (SDGs). The simple spark generation circuit is shown in Figure 2.3, showing the key components to generate repeating sparks. The elegance of this design is that the elec-
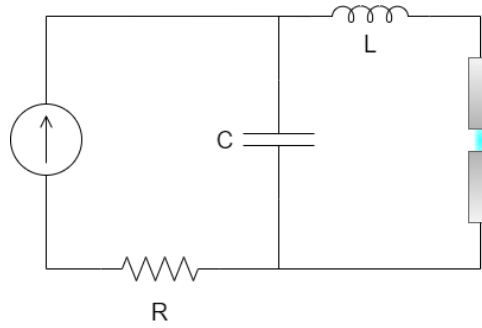
Figure 2.3: The classical spark discharge generator circuit, consisting of a capacitance (C), inductance (L) and resistance (R)

trode gap acts as a switch for the discharge. A capacitor C is charged by a constant power source until a breakdown voltage, V_D, is reached that is high enough to ionize the gas between the electrodes, leading to a discharge, after which the process repeats itself. The frequency of the spark, f depends on the speed at which the capacitors are charged and the energy of a discharge:

$$f = \frac{I}{CV_s} \tag{2.1}$$

Where I is the charging current and V_s is the mean discharge voltage. V_D can vary due to small fluctuations in the gas pressure and temperature or the location on the electrode where the spark occurs, so the precise frequency should be measured rather than calculated. When calculating the mean frequency, a mean voltage, V_s should therefore be used.

The duration of a spark is up to 10 μs depending on the components and settings used, so f is theoretically limited to almost 100 kHz, but in practice, this circuit is limited to a maximum of 500 Hz, at which point spark formation is too much influenced by the previous spark, creating large variations in V_D and irregular sparking. [22, 33, 36] To avoid this, a high-frequency switching circuit has been developed by Pfeiffer et al. that decouples the charging and discharging of the capacitors and fixes the discharge voltage. [22] This results in a spark that always has the same discharge energy, enabling frequencies of up to 25 kHz. The system in this dissertation uses the already commercialized modified version of the simple spark circuit of Figure 2.3.

MASS PRODUCTION RATE AND PARTICLE SIZE
The spark energy E_s depends on the capacitance and spark voltage according to:

$$E_s = \frac{1}{2}CV_s^2 \tag{2.2}$$

The ablated mass per spark is however not directly proportional to E_s, due to energy losses in the system represented by the minimal energy required to ablate material, E_0. The ablated mass per spark can then be expressed as equation 2.3, with C_{mat} a material

constant that is dependent on the heat capacity of the solid (c_{ps}), liquid (c_{cl}), melting and boiling points (T_m and T_b) and enthalpies of melting and evaporation (H_m and H_v) according to equation 2.4. [35, 37] α is an empirically determined constant that is determined by the electrode mass loss measurement during ablation.

$$\Delta m = \alpha * C_{mat} * (E_s - E_0) \tag{2.3}$$

$$C_{mat} = \frac{1}{c_p s(T_m - T) + c_p l(T_b - T_m) + H_m + H_v} \tag{2.4}$$

Because of the requirement to do empirical measurements to calibrate this formula for a specific setup, Δm can only be calculated as an estimate for the production rate. Feng et al. have shown that $\alpha = 0.0018$ for spark ablation generators in the same configuration as the one in this thesis. [35] We will therefore use this value in further calculations. An α of 0.0018 means that only 0.18% of the energy of a spark goes into the ablated spot.

Since the mass ablation rate $m = \Delta m * f$, we can calculate the theoretical mass production rate for an SDG. Using the example of Au nanoparticles generated in N_2 with typical settings of $C = 20$ nF, $V_s = 1$ kV, and $I = 8$ mA, we get an ablated mass per spark of 8.3 μg per spark at $f = 400$ Hz and a production rate of 12 mg h^{-1}. This is the theoretical mass ablation rate, not the nanoparticle production rate or even the mass deposition rate further downstream of the generator. A significant portion of the mass remains in the chamber due to turbulence, re-deposition of the mass on the electrodes, or is lost on the tubing walls in the system. This will be discussed later in this chapter in the description of the experimental setup and in chapter 3.

It follows from the previous section that to increase the mass production rate, one must maximize ΔM or f. C is typically fixed, so we control the production rate by adjusting V_s and I only: the spark power. The elegance of this is that only two well-controllable parameters have to be tuned to control the entire process. Controlling I is done by adjusting the power supply input, while V_s depends solely on the electrode gap and gas composition. V_s can therefore be controlled by adjusting the electrode distance.

Controlling the primary nanoparticle size is achieved by adjusting the mass loading of each spark event (i.e. the amount of material that can evaporate per spark) and the quenching rate (i.e. the speed at which the nanoparticles form). High gas flow increases the quenching rate and dilutes the vapour cloud, leading to smaller nanoparticles. Higher spark power (higher V_s or I) increase the mass loading per spark. An excellent empirical overview of the effect of many parameters in spark ablation has been published by Tabrizi et al. [36], while an analytical model for particle growth is presented by Feng et al. [35]

NANOPARTICLE COMPOSITION

SDGs use only the electrodes and a carrier gas (commonly N_2 or Ar), so they produce clean, uncontaminated particles when the proper precautions are taken. [33] It is even possible to generate pure metallic nanoparticles, even from reactive elements such as

Mg when extensive anti-oxidation measures are taken. [38] Using two different elec-
trodes makes it possible to create binary particles with alloys. [39, 40] Adding more
elements to the parent electrodes allows the synthesis of alloys that only exist on the
nanoscale. [41] The operation of two SDGs in series or in parallel can result in decorated
particles or agglomerates. Figure 2.4 shows the four modes of mixing. Atomic mixing
refers to the internally homogeneous composition of a nanoparticle, although the indi-
vidual nanoparticle composition can differ within the aerosol. [22] The combinations
of different metals and alloys are nearly endless. One can imagine that high throughput
screening of compositions will identify superior compositions in, for example, catalysis
or gas sensing.
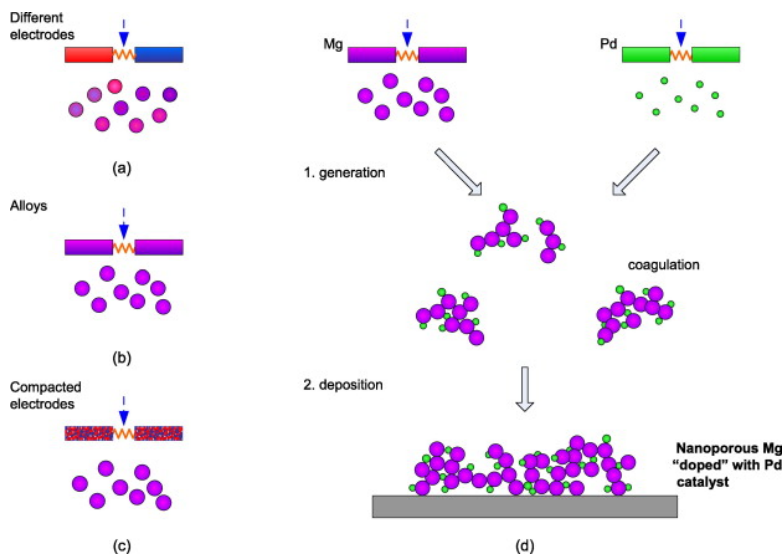
Figure 2.4: The different modes to create mixtures and compositions using spark ablation. Atomic mixing in a)
to c) and decoration using two generators in d). From Pfeiffer et al. (2014) [22]

The unprotected surface of the nanoparticles makes them highly reactive with oxy-
gen. It has been a recurring problem in spark ablation research that samples oxidize
rapidly during or after synthesis. To minimize the oxidation rate, a few precautions can
be taken. Firstly, flushing the system extensively with clean gas to remove residual air
after opening is necessary to bring down oxygen levels to ppm levels. To reduce the oxy-
gen and water levels further, oxygen and water traps can be installed at the gas inlet to
purify the incoming gas. This already assures a sufficiently low oxidation rate for some
metals. Still, for highly reactive metals, or applications where oxidation must be kept to
the absolute minimum, two extra measures can be taken. Vons et al. demonstrated suc-
cessful Mg nanoparticle synthesis with a thin oxide shell that formed after deposition.
[38] This was possible after baking out the setup under vacuum to remove water and
oxygen from the walls and after several hours of runtime. By running the setup for hours
before collecting a sample, the generated nanoparticles that attach to the inner walls of
the spark generator and tubing will collect the residual oxygen in the system and act as

2

getter material. [38, 42]

Lastly, since it is time-consuming and difficult to bake out a system or run it for hours without production, one can create a reducing atmosphere to suppress the oxidation reaction. This was first shown by Hallberg et al. for several metals by adding H_2 to the carrier gas. [43] They showed this effectively prevents oxidation at a H_2 concentration of only 5%. Because of the simplicity of this method, it has been employed extensively in this thesis to minimize oxidation. However, it is impossible to prevent oxygen contact after deposition unless one packages the material immediately after deposition.

ENVIRONMENTAL FOOTPRINT

The absence of any reactants during synthesis makes the nanoparticle surface free of any contaminants, so no cleaning or purification step is required. The chemical footprint of spark ablation is minimal, only the gas and electrode material are needed. Furthermore, spark ablation requires no storage and is used on-demand with minimal warm-up time, reducing wasted materials and waste energy. The energy footprint is approximately 0.13 g kWh^{-1} for Cu in N_2 [33], considerably lower than the energy use for arc ablation (1.5 g kWh^{-1} [32]) and comparable to laser ablation (0.28 g kWh^{-1} [44]), but these values are for drastically larger particle sizes. Lower ionization energy gasses lower the energy consumption per gram, with Ar, for example, lowering it by a factor of 2.6. [33]

2.4. NANOPARTICLE DEPOSITION

Aerosols can not be used in products unless they are deposited. Applications require either a thick powder coating, sparse decoration of a surface by nanoparticles, or a thin film. There are a few methods that are relevant for application in microelectronics, but we will focus on impaction since that is the only one applied in this thesis. Other methods, such as filtration or drop coating, are also applicable in microelectronics but are not as versatile or efficient.

Filtration captures the aerosol on a filter placed in the gas flow to create a powder, but this still needs to be transferred to a device. Alternatively, a device is placed in the gas flow, and particles land on it by diffusion. This is suitable for ultra-low loading of an active area but requires precautions to prevent coating of other areas (e.g. covers or masks). Liquid-based deposition methods all suffer from optimising the viscosity, evaporation rate, surfactant (and other additives) contamination and limited shelf life. Drop coating and dip coating expose a substrate to a nanoparticle suspension in a volatile liquid such that after evaporation, a thin film of nanoparticles remains. This is scalable, and multiple coats can control the thickness, but it requires nanoparticles in liquid and the correct formulation of this solution to have the best performance. Ink-based methods, such as ink-jet printing, are far more precise and accurate, but ink formulation is not trivial, so switching to different nanoparticles can be time-consuming.

2.4.1. IMPACTION

Impaction or aerosol jet deposition is one of the few methods that directly deposits nanoparticles from the aerosol to a substrate. It works by accelerating a gas through an orifice towards a surface at sufficiently high velocities that nanoparticles have enough

inertia on impact to immobilise them on the surface. [45–47] The nanoparticles follow the gas streamlines closely due to the low speed, so contraction of the gas through the nozzle causes the aerosol to be collimated. After exiting the nozzle, the nanoparticles will, due to their inertia at these speeds, remain in a collimated jet while the gas expands. [46, 48] This phenomenon is called aerodynamic focusing and is illustrated in Figure 2.5. If a sample is placed at a short enough distance, the collimated nanoparticle beam will not have slowed down enough, and nanoparticles impinge on the surface. At further distances, the nanoparticles will have slowed down enough to follow the gas flow again, and no deposition will occur. The resulting deposit has a Gaussian profile, as seen in Figure 2.6. With particles this small, there is an effect of the Brownian motion, but this affects primarily the nanostructure of the deposit, not the deposit shape or beam width. [48, 49]
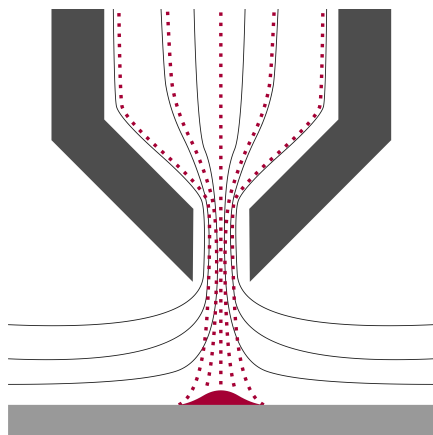
Figure 2.5: Sketch of the particle trajectories (dotted lines) and gas streamlines (solid lines) in a nozzle illustrating aerodynamic focusing and the resulting deposit below. Note that this is not a cross-section of the nozzles used in this thesis because the manufacturer did not disclose the shape.
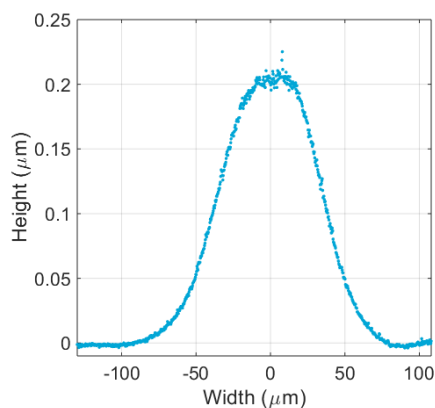
Figure 2.6: Cross section profile of an Au nanoparticle line printed by an impactor.

Impaction is possible at downstream pressures of several millibars or lower and occurs completely at room temperature, so it is compatible with a wide range of materials. It has been demonstrated to work on hard materials like glass and silicon and softer materials like paper or polymers. The main limiting factor is the force of the impaction jet itself. Small, fragile structures or too malleable materials can be damaged or warped due to the supersonic speed of the gas. This can be mitigated by placing the sample further away from the nozzle, but this widens the deposit and might reduce the collection efficiency (the percentage of captured particles) of the impactor.

By moving the substrate relative to the nozzle, by using a programmable XYZ-stage, it is possible to write with the nanoparticle beam. The impactor can thus be used as a printer for nanostructured films. In combination with spark ablation, it is a powerful tool that can print nanostructures on demand of a wide range of compositions and on many

substrates. In microelectronics, it enables the fabrication of complex patterns without a shadow mask or lithography.

2.5. SETUP DESCRIPTION

2.5.1. GENERATOR

Figure 2.7: Picture of the generator in through-flow configuration with a viewing window. Courtesy of VSParticle B.V.

The SDG in this setup is a first generation VSP-G1 configured in a cross-flow configuration with the gas flow perpendicular to the electrodes, similar to Figure 2.2. The gas inlet is positioned 2 cm from the electrode gap. The generator (see Figure 2.7 has two settings to adjust: current and voltage. It controls the voltage by moving the electrodes further (higher V) or closer (lower V) to each other, and it adjusts for fluctuations in the voltage by adjusting the distance continuously.
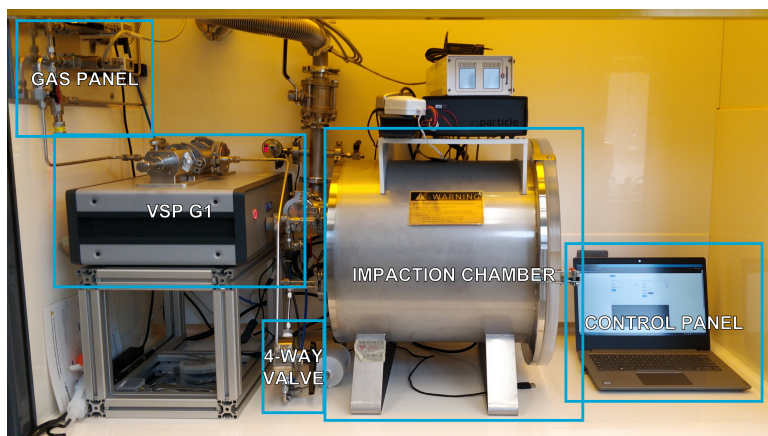
2.5.2. PROTO-0 SETUP

Figure 2.8: Picture of the setup as installed in the fumehood, with the main components labelled.

The Proto-0 setup of VSParticle B.V. is a prototype nanoparticle printing setup that consists of a VSP-G1 and an impaction chamber. The system consists of several main

components, as shown in Figure 2.8. During operation, it is a closed system with the impaction chamber under vacuum. The system is connected to three gas supplies, as shown in Figure 2.9, with programmable mass flow controllers (MFCs) for each gas. The VSP-G1 can be connected to the impaction chamber by turning the 4-way-valve. This diverts the gas flow from going directly to the exhaust to the impaction chamber. Not all gas that enters the impactor is used for deposition, a large fraction only flows past the nozzle towards the filter and is wasted. This is due to the choked flow inside the nozzle, which limits the gas flow to the nozzle throughput. The gas flow rate through the setup when printing is limited to max. 3 L min.$^{-1}$ due to pressure buildup caused by the small tubing inside the chamber. Increasing the flow above this can cause irregular sparking and should be avoided. At too low gas flows, the electrode gap is not flushed fast enough to have independent sparks, so a minimal gas flow of 1.5 L min.$^{-1}$ was set.

To control the printing, a switching mechanism was used that uses a flushing gas that enters the printing gas flow just after the aerosol inlet into the impactor. [50] As long as the flow of this gas is higher than the nozzle flow rate and the pressure higher than the aerosol gas flow, the nozzle will be filled with clean gas and stops depositing. The impactor will at all times have a gas jet, so no start-up or stopping effects are observed due to turbulence and pressure changes are kept to a minimum too.
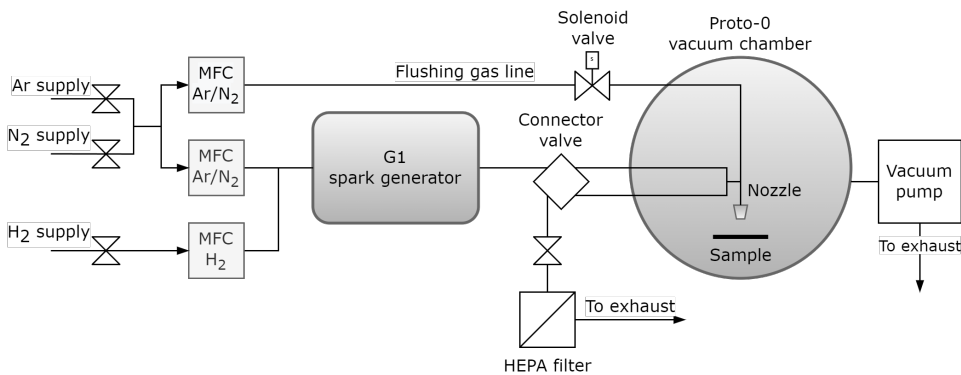
Figure 2.9: Diagram of the components and gas connections in the Proto-0 setup. The gas is supplied from the lab's supply lines and enters the setup at 1 bar.

DEPOSITION PARAMETERS AND PROGRAMMING

The system is controlled using a control panel to input and log the gas flow rates and generator voltage and current. It is also the interface for the printer controls in the G1 language and controls the solenoid valve for the flushing gas to switch deposition on or off. After starting up, complex scripts can be run with programmed start and endpoints.

The gasses are all at a 99.999% purity and come from the lab's main gas supply network. The setup operates at atmospheric pressure before the nozzle, while the downstream pressure in the impaction chamber depends on the nozzle used. There were three available nozzles: 0.1, 0.33 or 1.0 L min.$^{-1}$ that give a downstream pressure of 0.4, 0.7, or 1.6 mbar, respectively. This is low enough to ensure 100% collection efficiency for 2 nm

Ag nanoparticles at 1.0 mm nozzle to sample distance. [45]

2.6. SUMMARY

The applications of nanoparticles in microelectronics have been discussed. Their property of having a low melting point makes them interesting materials for die-attach applications and printed electronics. With a suitable printing method, nanoparticles can be applied as functional layers too, such as for gas sensing and catalysis.

Next, various methods to synthesize nanoparticles have been discussed. They can be split up into chemical and physics based methods. Brief overviews of several common synthesis methods were given, with special attention to the physical methods, as they are direct competitors of spark ablation, the method used in the rest of this thesis. The background and theory of spark ablation have been presented to give a good foundation for understanding the rest of this thesis. Compared to laser ablation and arc ablation, it is a more versatile and flexible synthesis method with a lower production cost. Deposition of nanoparticles can be done using filters or by transferring the particles to a liquid which is dried. In this thesis, impaction is used to deposit the nanoparticles and a description of this method and the resulting films is given.

Lastly, the equipment and experimental setup used to synthesise every deposit in this thesis is described. All components, the gas setup, and process parameters are disclosed. Later chapters will therefore have a shorter method section containing mostly the deviations to the standard operating conditions.

REFERENCES

[1] B. Zhang, A. Damian, J. Zijl, H. van Zeijl, Y. Zhang, J. Fan, and G. Zhang, *In-air sintering of copper nanoparticle paste with pressure-assistance for die attachment in high power electronics,* Journal of Materials Science: Materials in Electronics **32**, 4544 (2021).

[2] K.-S. Moon, H. Dong, R. Maric, S. Pothukuchi, A. Hunt, Y. Li, and C. P. Wong, *Thermal behavior of silver nanoparticles for low-temperature interconnect applications,* Journal of Electronic Materials **34**, 168 (2005).

[3] K. S. Siow, ed., *Die-Attach Materials for High Temperature Applications in Microelectronics Packaging* (Springer International Publishing, 2019).

[4] H. Zhang, G. Zou, L. Liu, H. Tong, Y. Li, H. Bai, and A. Wu, *Synthesis of silver nanoparticles using large-area arc discharge and its application in electronic packaging,* Journal of Materials Science **52**, 3375 (2016).

[5] A. Zinn, R. Stoltenberg, A. Fried, J. Chang, A. Elhawary, J. Beddow, and F. Chiu, *nanocopper based solder-free electronic assembly material,* Nanotech **2**, 71 (2012).

[6] T. Liyanage, A. Z. Qamar, and G. Slaughter, *Application of nanomaterials for chemical and biological sensors: A review,* IEEE Sensors Journal **21**, 12407 (2021).

[7] B. Saruhan, R. L. Fomekong, and S. Nahirniak, *Review: influences of semiconductor metal oxide properties on gas sensing characteristics,* Frontiers in Sensors **2** (2021), 10.3389/fsens.2021.657931.

[8] L. N. Sacco, H. J. van Ginkel, and S. Vollebregt, *Synthesis of carbon nanofibers (CNFs) by PECVD using Ni catalyst printed by spark ablation,* in *2022 IEEE 22nd International Conference on Nanotechnology (NANO)* (IEEE, 2022).

[9] P. McIntyre and A. F. i Morral, *Semiconductor nanowires: to grow or not to grow?* Materials Today Nano **9**, 100058 (2020).

[10] E. R. Hemesath, D. K. Schreiber, E. B. Gulsoy, C. F. Kisielowski, A. K. Petford-Long, P. W. Voorhees, and L. J. Lauhon, *Catalyst incorporation at defects during nanowire growth,* Nano Letters **12**, 167 (2011).

[11] C. G. Frost and L. Mutton, *Heterogeneous catalytic synthesis using microreactor technology,* Green Chemistry **12**, 1687 (2010).

[12] S. Kataoka, Y. Takeuchi, A. Harada, T. Takagi, Y. Takenaka, N. Fukaya, H. Yasuda, T. Ohmori, and A. Endo, *Microreactor containing platinum nanoparticles for nitrobenzene hydrogenation,* Applied Catalysis A: General **427-428**, 119 (2012).

[13] Z. Wu, G. Yang, E. Mu, Q. Wang, S. A. Meijer, and Z. Hu, *Nanofire and scale effects of heat,* Nano Convergence **6**, 5 (2019).

[14] K. Park, J. S. Son, S. I. Woo, K. Shin, M.-W. Oh, S.-D. Park, and T. Hyeon, *Colloidal synthesis and thermoelectric properties of La-doped SrTiO3 nanoparticles,* J. Mater. Chem. A **2**, 4217 (2014).

[15] M. Parashar, V. K. Shukla, and R. Singh, *Metal oxides nanoparticles via sol–gel method: a review on synthesis, characterization and applications,* Journal of Materials Science: Materials in Electronics **31**, 3729 (2020).

[16] B. O. Dabbousi, J. Rodriguez-Viejo, F. V. Mikulec, J. R. Heine, H. Mattoussi, R. Ober, K. F. Jensen, and M. G. Bawendi, *(CdSe)ZnS core-shell quantum dots: Synthesis and characterization of a size series of highly luminescent nanocrystallites,* The Journal of Physical Chemistry B **101**, 9463 (1997).

[17] A. Dey, J. Ye, A. De, E. Debroye, S. K. Ha, E. Bladt, A. S. Kshirsagar, Z. Wang, J. Yin, Y. Wang, L. N. Quan, F. Yan, M. Gao, X. Li, J. Shamsi, T. Debnath, M. Cao, M. A. Scheel, S. Kumar, J. A. Steele, M. Gerhard, L. Chouhan, K. Xu, X. gang Wu, Y. Li, Y. Zhang, A. Dutta, C. Han, I. Vincon, A. L. Rogach, A. Nag, A. Samanta, B. A. Korgel, C.-J. Shih, D. R. Gamelin, D. H. Son, H. Zeng, H. Zhong, H. Sun, H. V. Demir, I. G. Scheblykin, I. Mora-Seró, J. K. Stolarczyk, J. Z. Zhang, J. Feldmann, J. Hofkens, J. M. Luther, J. Pérez-Prieto, L. Li, L. Manna, M. I. Bodnarchuk, M. V. Kovalenko, M. B. J. Roeffaers, N. Pradhan, O. F. Mohammed, O. M. Bakr, P. Yang, P. Müller-Buschbaum, P. V. Kamat, Q. Bao, Q. Zhang, R. Krahne, R. E. Galian, S. D. Stranks, S. Bals, V. Biju, W. A. Tisdale, Y. Yan, R. L. Z. Hoye, and L. Polavarapu, *State of the art and prospects for halide perovskite nanocrystals,* ACS Nano **15**, 10775 (2021).

2

[18] H. Schmidt, *Considerations about the sol-gel process: From the classical sol-gel route to advanced chemical nanotechnologies,* Journal of Sol-Gel Science and Technology **40**, 115 (2006).

[19] W. Y. Teoh, R. Amal, and L. Mädler, *Flame spray pyrolysis: An enabling technology for nanoparticles design and fabrication,* Nanoscale **2**, 1324 (2010).

[20] S. Liu, M. M. Mohammadi, and M. T. Swihart, *Fundamentals and recent applications of catalyst synthesis using flame aerosol technology,* Chemical Engineering Journal **405**, 126958 (2021).

[21] K. Wegner and S. E. Pratsinis, *Scale-up of nanoparticle synthesis in diffusion flame reactors,* Chemical Engineering Science **58**, 4581 (2003).

[22] T. Pfeiffer, J. Feng, and A. Schmidt-Ott, *New developments in spark production of nanoparticles,* Advanced Powder Technology **25**, 56 (2014).

[23] M. T. Swihart, *Vapor-phase synthesis of nanoparticles,* Current Opinion in Colloid & Interface Science **8**, 127 (2003).

[24] C. Dhand, N. Dwivedi, X. J. Loh, A. N. J. Ying, N. K. Verma, R. W. Beuerman, R. Lakshminarayanan, and S. Ramakrishna, *Methods and strategies for the synthesis of diverse nanoparticles and their applications: a comprehensive overview,* RSC Advances **5**, 105003 (2015).

[25] Z.-H. Ge, B.-P. Zhang, Y.-X. Chen, Z.-X. Yu, Y. Liu, and J.-F. Li, *Synthesis and transport property of Cu1.8S as a promising thermoelectric compound,* Chem. Commun. **47**, 12697 (2011).

[26] S. Ballikaya, H. Chi, J. R. Salvador, and C. Uher, *Thermoelectric properties of Ag-doped Cu2Se and Cu2Te,* J. Mater. Chem. A **1**, 12478 (2013).

[27] J. de Carvalho, S. de Medeiros, M. Morales, A. Dantas, and A. Carriço, *Synthesis of magnetite nanoparticles by high energy ball milling,* Applied Surface Science **275**, 84 (2013).

[28] C. Peineke, M. Attoui, and A. Schmidt-Ott, *Using a glowing wire generator for production of charged, uniformly sized nanoparticles at high concentrations,* Journal of Aerosol Science **37**, 1651 (2006).

[29] K. Wegner, B. Walker, S. Tsantilis, and S. E. Pratsinis, *Design of metal nanoparticle synthesis by vapor flow condensation,* Chemical Engineering Science **57**, 1753 (2002).

[30] M. Ullmann, S. K. Friedlander, and A. Schmidt-Ott, *Nanoparticle formation by laser ablation,* Journal of Nanoparticle Research **4**, 499 (2002).

[31] N. G. Semaltianos, *Nanoparticles by laser ablation,* Critical Reviews in Solid State and Materials Sciences **35**, 105 (2010).

[32] M. Stein and F. E. Kruis, *Optimization of a transferred arc reactor for metal nanoparticle synthesis,* Journal of Nanoparticle Research **18** (2016), 10.1007/s11051-016-3559-y.

[33] A. Schmidt-Ott, *Spark Ablation: Building Blocks for Nanotechnology,* 1st ed., edited by A. Schmidt-Ott (Jenny Stanford Publishing, 2020).

[34] S. Schwyn, E. Garwin, and A. Schmidt-Ott, *Aerosol generation by spark discharge,* Journal of Aerosol Science **19**, 639 (1988).

[35] J. Feng, L. Huang, L. Ludvigsson, M. E. Messing, A. Maisser, G. Biskos, and A. Schmidt-Ott, *General approach to the evolution of singlet nanoparticles from a rapidly quenched point source,* The Journal of Physical Chemistry C **120**, 621 (2015).

[36] N. S. Tabrizi, M. Ullmann, V. A. Vons, U. Lafont, and A. Schmidt-Ott, *Generation of nanoparticles by spark discharge,* Journal of Nanoparticle Research **11**, 315 (2008).

[37] F. L. Jones, *Electrode erosion by spark discharges,* British Journal of Applied Physics **1**, 60 (1950).

[38] V. Vons, A. Anastasopol, W. Legerstee, F. Mulder, S. Eijt, and A. Schmidt-Ott, *Low-temperature hydrogen desorption and the structural properties of spark discharge generated Mg nanoparticles,* Acta Materialia **59**, 3070 (2011).

[39] J. H. Byeon, J. H. Park, and J. Hwang, *Spark generation of monometallic and bimetallic aerosol nanoparticles,* Journal of Aerosol Science **39**, 888 (2008).

[40] N. S. Tabrizi, Q. Xu, N. M. van der Pers, and A. Schmidt-Ott, *Generation of mixed metallic nanoparticles from immiscible metals by spark discharge,* Journal of Nanoparticle Research **12**, 247 (2010).

[41] J. Feng, D. Chen, P. V. Pikhitsa, Y. ho Jung, J. Yang, and M. Choi, *Unconventional alloys confined in nanoparticles: Building blocks for new matter,* Matter **3**, 1646 (2020).

[42] V. A. Vons, L. C. P. M. de Smet, D. Munao, A. Evirgen, E. M. Kelder, and A. Schmidt-Ott, *Silicon nanoparticles produced by spark discharge,* Journal of Nanoparticle Research **13**, 4867 (2011).

[43] R. T. Hallberg, L. Ludvigsson, C. Preger, B. O. Meuller, K. A. Dick, and M. E. Messing, *Hydrogen-assisted spark discharge generated metal nanoparticles to prevent oxide formation,* Aerosol Science and Technology **52**, 347 (2017).

[44] W. T. Nichols, J. W. Keto, D. E. Henneke, J. R. Brock, G. Malyavanatham, M. F. Becker, and H. D. Glicksman, *Large-scale production of nanocrystals by laser ablation of microparticles in a flowing aerosol,* Applied Physics Letters **78**, 1128 (2001).

[45] J. F. de la Mora and A. Schmidt-Ott, *Performance of a hypersonic impactor with silver particles in the 2 nm range,* Journal of Aerosol Science **24**, 409 (1993).

[46] S. Rennecke and A. P. Weber, *A novel model for the determination of nanoparticle impact velocity in low pressure impactors,* Journal of Aerosol Science **55**, 89 (2013).

2

[47] C. Li, N. Singh, A. Andrews, B. A. Olson, T. E. Schwartzentruber, and C. J. Hogan, *Mass, momentum, and energy transfer in supersonic aerosol deposition processes,* International Journal of Heat and Mass Transfer **129**, 1161 (2019).

[48] X. Wang, F. E. Kruis, and P. H. McMurry, *Aerodynamic focusing of nanoparticles: I. guidelines for designing aerodynamic lenses for nanoparticles,* Aerosol Science and Technology **39**, 611 (2005).

[49] G. J. Lindquist, D. Y. Pui, and C. J. Hogan, *Porous particulate film deposition in the transition regime,* Journal of Aerosol Science **74**, 42 (2014).

[50] K. Weber, M. Koole, and T. V. Pfeiffer, *Switching device, deposition device comprising the switching device, method for switching a fluid flow, and method for depositing particles onto a substrate,* (2020).

3

QUANTIFYING MASS AND POROSITY OF A NANOPARTICLE DEPOSIT

Door meten tot weten.

Heike Kamerlingh Onnes

It is difficult to quantify the mass of a nanoporous deposit made using spark ablation because the resulting mass is too low for conventional mass balances. However, mass is crucial to measure to understand nanoporous films better. Knowing how much material is deposited improves reproducibility and process control, while mass is also a quantity used to calculate other properties. Film density is such a derivative of mass and an important variable in calculations such as those for electrical and thermal conductivity. Developing a reliable method to measure the mass deposition rate of spark ablation generated nanoparticles using impaction was therefore highly desired. In this chapter, a solution is presented to measure the deposition rate by using a quartz crystal microbalance. The theory of quartz crystal microbalances and how to use them in impaction deposition chambers is explained, after which the results of this method are presented. Finally, the density and, by extension, the porosity was calculated and compared to literature.

3.1. MEASURING SMALL VOLUMES AND MASSES

WITH the advancement of nanotechnology come opportunities to discover new materials that can outperform conventional materials. However, this requires accurate measurements of the performance and of both intrinsic and extrinsic material properties. In particular, extrinsic properties are challenging since it becomes difficult to measure them on the nanoscale because probes are too large, the equipment is not accurate enough, or the amount of material is just too small to give a sufficient response.

For nanoparticle or nanoporous films, like the ones in this thesis, one of the most difficult problems is the quantification of density. [2] This requires accurate measurements of the deposited mass and volume or an accurate direct way to measure the density and, by extension of that, porosity. Small masses in the microgram range are extremely difficult to measure with a mass balance since small changes in air pressure, humidity, or temperature can already create large errors in the same order of magnitude as the mass itself. Deposition rates are often not precisely known or hard to measure or estimate. For direct porosity measurements, the most popular method is gas adsorption based on the Brunauer–Emmett–Teller (BET) method. Although this can directly measure the adsorption volume, it requires larger quantities for accurate measurement and is inaccurate for nanoscale pores. [2, 3] Hence, to quantify mass, density, or porosity, we need alternative methodologies.

When we look at thin-film deposition equipment, such as sputter coaters or evaporators we see that they measure the deposited mass and calculate the film thickness using the known density, assuming the film is non-porous. They do this using a quartz crystal microbalance (QCM), a device that changes resonance frequency when loaded with a mass. QCMs are particularly convenient because they require no calibration, can achieve nanogram resolution, and are cheap. Their operation requires a simple circuit and specifically cut quartz crystals that are commonly available. For decades now, QCMs have been employed in process control in metal evaporators, sputter coaters [4], or atomic layer deposition (ALD) equipment [5] Günther Sauerbrey first described QCMs in his 1959 paper [6], but since then QCM theory has been improved to allow for more accurate devices and more application possibilities. [7–12] They have since been used in thin film deposition process monitoring [4, 5], as gas sensors [13–15], as biochemical sensors [16, 17], and even atmospheric aerosol sampling [18–20].

In this chapter, it is demonstrated that QCMs can be applied as mass balances for nanoporous films too and that they can provide process monitoring for nanoparticle film deposition. Next, we combine the mass measurement with volume data to calculate the density and porosity. We validate the method for use with metal nanoparticle aerosol deposition and discuss the effect of the impaction deposition on the QCM response.

3.2. QUARTZ CRYSTAL MICROBALANCE THEORY

3.2.1. WORKING PRINCIPLE

Piezoelectric crystals have the ability to deform when exposed to an electric field. When exposed to an oscillating electric field, the crystal will start oscillating at its resonance frequency. Depending on the size, shape, crystal orientation, and composition, each

crystal has a specific natural resonance frequency. This property has been applied extensively in electronics to create or stabilize constant frequency signals or provide clock signals. The most common crystal oscillator material is quartz (a form of SiO_2) because of its low price, mechanical hardness, and excellent frequency stability. The majority of quartz oscillators are the so called AT-cut crystals, which are cut at a 35.25° angle from the z-axis of the crystal.
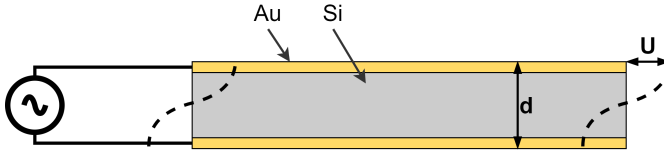

Figure 3.1: Diagram showing the side view of a quartz crystal with Au electrodes (in yellow) on the top and bottom. The shear oscillation, indicated by the dotted lines, has an amplitude U.

It was Günter Sauerbrey who first proposed to use quartz discs as mass balances in 1959. [6] He used the fact that a well-defined quartz disc has a resonance frequency dependent on its thickness according to eq. 3.1.

$$f = \frac{v}{2d} = \frac{N}{d} \tag{3.1}$$

With f the frequency of the crystal, v the wave propagation speed (i.e. the speed of sound), and d the frequency. N is the so called natural frequency constant, defined as $v/2$ and is 1670 kHz mm for AT-cut quartz. Next, from the inverse relation between f and d, it logically follows that

$$\frac{\Delta f}{f_0} = \frac{-\Delta d}{d_0} \tag{3.2}$$

Where f_0 and d_0 are the original resonance frequency and thickness respectively. If we then substitute d according to eq. 3.3, we obtain eq. 3.4.

$$d = \frac{m}{A\rho_q} \tag{3.3}$$

$$\frac{\Delta f}{f_0} = \frac{-\Delta m}{A\rho_q d_0} \tag{3.4}$$

With A as the surface area of quartz disc and ρ_q the density of quartz (2.648 g cm^{-3}). Finally, if we then substitute eq. 3.2 for d_0 and rewrite it to isolate Δf, we obtain the Sauerbrey equation:

$$\Delta f = -\frac{f_0^2}{NA\rho_q}\Delta m \tag{3.5}$$

Using eq. 3.5, we can now directly convert frequency change to mass change if the resonating area is known. Note that everything in front of Δm is constant and only depends on the properties of the quartz. Sauerbrey, therefore, introduced a constant, C_f,

for simplification, as seen in eq. 3.6. For AT-cut quartz with a resonance frequency of 10 MHz, C_f is 0.2264 Hz ng^{-1} cm^{-2}. It is thus possible to measure masses with near nanogram accuracy, especially when the oscillating area is reduced. z

$$\Delta f = -C_f A \Delta m \tag{3.6}$$

3.2.2. VALIDITY OF THE SAUERBREY EQUATION
The Sauerbrey equation is valid if two conditions are met:

1. The deposited mass is uniformly distributed over the entire oscillating area. In other words, a uniform height increase (Δd).

2. The deposited material has the same acousto-elastic properties as the quartz. Impedance or elasticity decouples the resonance change from the mass increase, invalidating equation 3.1.

Obviously, no material has the same exact properties as the oscillator, so the Sauerbrey equation is only an approximation. Lu and Lewis (1972) have shown that the Sauerbrey equation is valid for small masses of < 2% of the initial quartz mass, and that higher loading gives a larger error. [9] They propose a more precise equation that works up to 15% mass loading. In the measurements presented in this chapter, deposited masses never approach this 2% limit so the simple Sauerbrey equation can be used.

3.2.3. RESPONSE DISTRIBUTION
In the previous section, we established that the size of the oscillating area has an effect on the sensitivity based on the Sauerbrey equation (eq. 3.5). This is because this equation is based on a uniform height increase of the oscillating area. Essentially, the Sauerbrey equation gives the average response of a QCM over the whole electrode area, but a local deposit can cause a vastly different frequency change. A non-uniform mass distribution will therefore cause an error in the measurement. The cause of this sensitivity distribution is the displacement amplitude of the oscillations. Sauerbrey himself already described this and determined a round crystal has a Gaussian mass sensitivity distribution with the peak at the centre of the oscillating area, as shown in Figure 3.2. [6, 21] As a consequence, it is impossible to calculate the mass change of local deposit(s) without knowing the exact mass distribution.

The amplitude decays to zero outside the electrode area, but, especially for small electrode areas, deposition in this region can still significantly contribute to the frequency response. [12] The response decreases with distance r from the center, as described in equation 3.7, with the amplitude *U(r)* being a Bessel function, see equation 3.8. [12, 21]

$$S_f(r) = \frac{|U(r)|^2}{\int_0^\infty r\,|A(r)|^2\,dr} C_f \tag{3.7}$$

$$r^2 \frac{\partial^2 U}{\partial r^2} + r \frac{\partial U}{\partial r} + (r k_r)^2 U = 0 \tag{3.8}$$
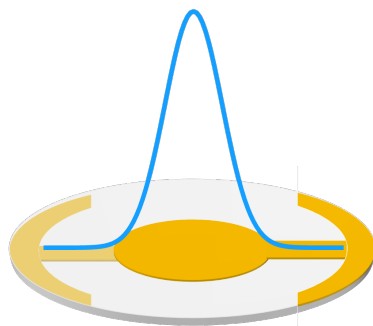
Figure 3.2: Diagram showing the sensitivity distribution (blue line) above a quartz crystal microbalance. The gold center is the oscillating electrode area which is connected to gold contacts at the edge. The bottom electrode contacts are visible on the left side.

It follows that there are rings on the QCM with equal mass sensitivity. This property can be used to design QCMs with a more uniform sensitivity distribution, as demonstrated by Jiang and Tang (2021). [12] It must be noted that there also exists a ring at a radius where the sensitivity is the same as the average sensitivity of the whole electrode, but this requires precise deposition and is, therefore, impractical. Knowing that the responsivity of a QCM is location dependent helps us to interpret the results of a localized deposition method such as impaction printing. We expect a decaying response when printing further from the centre, even if the deposition rate remains constant. However, the result should be the average of the whole area if the printing is uniform.

3.3. NANOPARTICLE MASS MEASUREMENT USING A QCM

Now that we understand how a QCM works and what the results should look like, we can apply this knowledge and measure the mass of nanoparticle deposits. This section will list the equipment and components and describe the procedure for using them.

3.3.1. COMPONENTS AND SOFTWARE

The QCMs used for these experiments are 10 MHz crystals with a 14 mm diameter supplied by Novaetech S.r.l. They have 6 mm diameter gold electrodes deposited on the front and back side with connectors on the edges. It is placed in an OpenQCM quartz holder and soldered to two coax cables, as seen in Figure 3.3. The wires are connected to a vacuum feed-through and connected to an OpenQCM Arduino shield that drives the QCM and reads the frequency. An Arduino Micro board is mounted on this shield with preinstalled OpenQCM software. The default software samples once per second, giving it an accuracy of 1 Hz by averaging the response over that 1 second. It was edited to sample five times per second, but this logically must reduce the maximum sensitivity to 5 Hz, or 6.2 ng. This compromise was deemed necessary to improve the response time and to more accurately observe the deposition behaviour. All OpenQCM hardware and software is open source. The full Arduino code is disclosed in appendix B with the Matlab script to read the serial data and plot it during measurement.
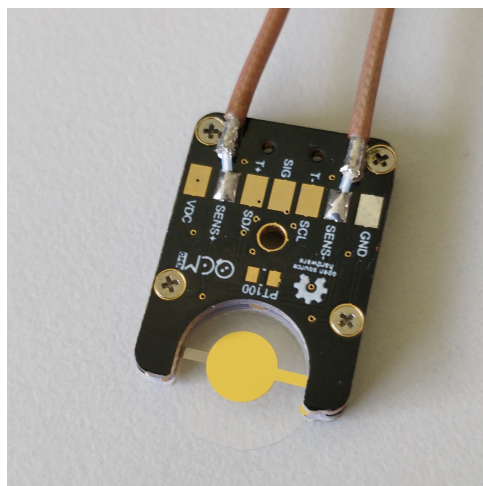
Figure 3.3: The QCM holder with a 10 MHz QCM mounted in it.

3.3.2. QCM MEASUREMENT PROCEDURE

Synthesis and deposition were done using the same equipment as described in chapter 2. To demonstrate this method, Au electrodes were used with $1.5\,l\,min^{-1}$. N_2 gas because there is no oxidation. Furthermore, Au is a well understood metal to deposit, simplifying the interpretation of the data. To satisfy the conditions to apply the Sauerbrey equation, a printing pattern consisting of overlapping concentric circular deposits was designed such that the entire electrode area would be covered with a thin nanoparticle film. This ensures that the deposition is rotationally symmetrical and as uniform as possible to minimize any location effects. The pattern is shown in Figure 3.4. The printing speed was set at a speed at which the deposited mass will never exceed 2% of the QCM mass. Total deposition time with a printing speed of $50\,mm\,min^{-1}$. is 159.96 s.
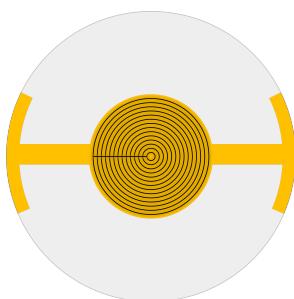
Figure 3.4: The QCM printing pattern as seen from the top. Printing starts with a 0.2 mm diameter circle and continues outward, starting on the left side. After the final circle with a 2.8 mm diameter is printed, the nozzle then moves back to the center. The motion between circles and back to center is with $200\,mm\,min^{-1}$.

After the first tests, it was clear the impaction jet has a considerable effect on the QCM frequency. Therefore, a baseline was established during one minute before and

after moving the nozzle above the QCM to have a well defined beginning and end point. To obtain reliable data, the average of the first and last 5 seconds of a measurement are used as beginning and end frequency. Before and after deposition, the nozzle waits one minute (with clean gas flow) at the electrode centre before starting or stopping deposition to clearly show the effect of the jet without deposition. More details on the effect of the gas jet can be seen in section 3.4.1.

3.4. Mass deposition results

Here, the results of deposition on a QCM are shown. First, the frequency response is explained and the effect of the gas jet is shown. A mass deposition rate is then extracted for different synthesis settings and compared to literature.

3.4.1. Influence of the gas jet
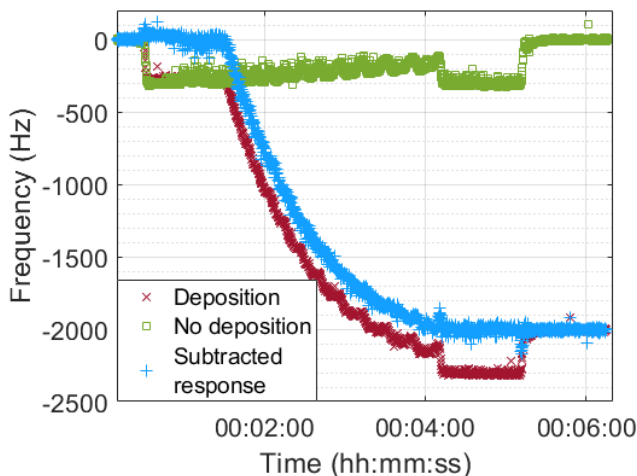
Figure 3.5: Typical QCM frequency shift during deposition. The green curve shows the effect of the gas jet without deposition. The blue line is the result of subtracting the green curve from the red, eliminating the jet effect. This sample was made at 5 mA, 1 kV G1 settings, and 1 mm nozzle distance.

The most notable feature of the graphs obtained during QCM measurement is the effect of the gas jet. As shown in Figure 3.5, without any nanoparticle deposition, the frequency shifts considerably and changes over time during nozzle movement. Two effects cause this phenomenon. First, the force of the jet causes stress and slight warping of the QCM, causing the resonance frequency to change. This is the cause of the jump up when the nozzle above the crystal and the jump back when it moves away from the crystal. The second effect is due to the QCM sensitivity distribution. The nozzle starts moving over the substrate at a constant speed but in increasingly larger circles. As explained in section 3.2.3, the QCM response is radially dependent, causing a stronger frequency shift in the middle. This results in an apparent gradual decrease of the deposition rate. This location dependency is most clearly visible when the nozzle moves back to the middle

of the electrode area, causing a fast drop in frequency around 4:10 in Figure 3.5. When the nozzle is moved away from the QCM, we can observe a shift back to the original resonance frequency, showing the gas jet has no lasting effects on the QCM. Additionally, this proves that the nozzle has no measurable deposition in the *off* state when only clean gas goes through the nozzle.

Due to the circular pattern, we see a wave pattern emerge. With the increase of circumference for each consecutive circle, the period of this wave pattern increases. The peak of a wave coincides with the nozzle being on the left side of the electrode. The wave is not perfectly sinusoidal due to the inhomogeneous effect of the gas jet caused by the holder geometry, nozzle tilt relative to the electrode area, and a possible slight offset of the circles to the electrode centre. The gas effect is therefore not identical for each measurement or crystal. Fortunately, we are not interested in the local sensing behaviour but are looking to obtain the average response of the QCM. When subtracting the curve without deposition from the curve with deposition, as done in Figure 3.5, we can completely remove the gas jet effect from the data. The resulting curve (blue) shows the exact behaviour one would expect with slightly more noise. Although it would be possible to do this subtraction for all measurements, it is unnecessary and time-consuming. The beauty of QCM measurements is that they require no calibration. For quantifying the deposited mass, it suffices to use the beginning and end of each curve and ignore the deposition process entirely.

3.4.2. MASS DEPOSITION RATE

The effect of several synthesis parameters was tested, starting with the effect of the generator current. According to spark ablation theory, as explained in chapter 2, spark frequency, f_s, is directly proportional to the generator current, I, according to equation 3.9. [22–25] Assuming mass ablation per spark remain constant, mass generation rate is directly proportional to the current too.

$$f_s = \frac{I}{2CV_S} \tag{3.9}$$

Figure 3.6 confirms that this relation is valid for the deposition rate. We can see a good linear relationship between the current and deposition rate. Deposition rates are not equal to generation rates in the G1. Not only does this nozzle have a throughput of 0.32 l min^{-1}, just 21% of the flow through the generator, but there is also material loss by adhesion to the tubing. Due to turbulent gas flow around the electrodes inside the generation chamber, not all ablated material even reaches the tubing but remains inside the generator as a black powder coating on the chamber and electrodes. To measure the ablation rate solely, one must either quantify these losses or measure the mass change of the electrodes, as was done in previous publications. [22, 24, 26] Tabrizi found an electrode mass loss of 0.0705 mg h^{-1} f$_s^{-1}$ (at 2 nF, 1 mm electrode distance, and 0.8 l min^{-1}), giving a mass production rate of 8.81 mg h^{-1} at 125 Hz for Au in Ar. [22] Our setup operates at 125 Hz at 5 mA (with 20 nF and 1 kV) and we see a deposition rate of 0.75±0.22 μg min^{-1}, as seen in table 3.1. Correcting for the 0.32 l min^{-1} nozzle, we find a generator output of 212±60 μg h^{-1}.
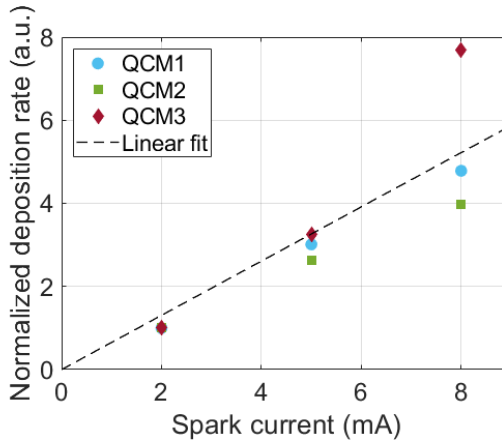
Figure 3.6: Deposition rate plotted as a function of generator current for three QCMs. The dotted line represent a linear fit through these points. The data was normalized for better comparison, removing production fluctuations between sessions. All data was collected in the same session for each QCM and with a 1 mm nozzle distance.

Table 3.1: Deposited mass and deposition rates at 1 mm and the corresponding calculated G1 output for three generation currents.

Current (mA)	Spark frequency (Hz)	Mass (μg)	Printing rate ($\mu g \, min^{-1}$.)	Calculated GI output ($\mu g \, h^{-1}$)
2	50	0.62 ± 0.05	0.23 ± 0.02	65 ± 5
5	125	2.01 ± 0.69	0.75 ± 0.22	212 ± 60
8	200	4.35 ± 1.04	1.63 ± 0.39	459 ± 110

We can think of several reasons for this discrepancy with Tabrizi's value. Firstly, the value does not include material losses as discussed above, she estimates a loss of 62-78% when she compares electrode mass loss with a deposited mass on filter papers. Secondly, although the frequency is the same, the operating conditions are not. We used N_2 gas, which has a factor 2.6 lower ablation efficiency than Ar [25], combined with the estimated loss, and this brings the "deposition rate" to roughly $0.75 \, mg \, h^{-1}$. the gas flow is also lower, while the energy per spark is higher. As she reports, this leads to the formation of large particles that account for a considerable fraction of the ablated mass, but lower spark energy (by lowering V_s) could avoid that. [23] We have not observed such large particles during deposition. Lastly, the setups are different. The chamber, the electrodes and their holders, and the tubing are different, causing different generation efficiencies and losses in the setup. Interestingly, although the losses are not easily quantifiable, they seemingly scale with the generated mass linearly because the mass deposition rate scales linearly with the current, precisely like the generation rate.

$$\Delta m = C_{mat}(E_s - E_0) \tag{3.10}$$

$$E_s = \frac{1}{2}CV_s^2 \tag{3.11}$$

According to Feng et al. (2015), ablated material per spark is given by equation 3.10 and multiplication with the spark frequency gives the production rate. [26] He calculated E_0 to be 1.98 mJ, C_{mat} to be 8.33×10^{-7}gJ^{-1} for Ar, and 2.6 times lower for N$_2$ at 3.2×10^{-7} g J^{-1} [25, 26]. Using equation 3.11, the ablation rate of Au in N$_2$ at 5 mA and 1 kV and 20 nF is 17.7 mg h^{-1}, nearly two orders of magnitude higher than found here and double that of Tabrizi's. This is partly because Feng's value is an idealized model for ablation rate, not deposition rate. It accounts for no mass loss during transportation to the deposition chamber or other inefficiencies in a system. Each system has its own transport or deposition efficiency; even different electrode sets will behave slightly different. For these reasons, it will always be necessary for practical applications to measure deposition rate rather than calculate it or use the electrode mass loss. Correlating found deposition rates like the ones presented here to a synthesis model such as Feng's will always be instrument-dependent and can never be applied without calibration. For this reason, it is not done here since this is a unique prototype instrument that will be improved in newer generations.
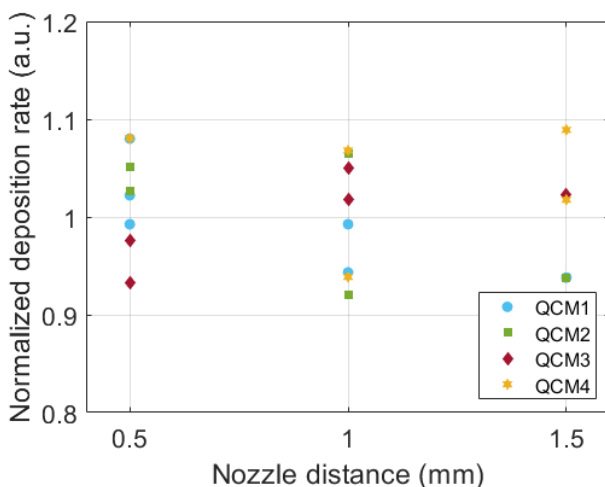
Figure 3.7: Deposition rate plotted versus nozzle distance. The data is normalized to the mean of each QCM for better comparison because the absolute values differ per QCM.

The second relation to be tested was the influence of the nozzle distance versus deposition rate. Impaction energy is inversely proportional to nozzle distance, so by moving the nozzle further away, we could see a loss in deposition rate. This appears not to be the case for the distances tested here, as shown in Figure 3.7. No trend can be identified,

not even within a single QCM. This shows equal collection efficiencies at those heights, suggesting 100% impaction efficiency at all tested heights. De la Mora and Schmidt-Ott(1993) used an impactor operated at 1.4 Torr with a 0.3 mm nozzle diameter (d_n) and determined the collection efficiency for <5 nm Ag nanoparticles generated by spark ablation at various nozzle distances (L). [27] They found that at $L/d_n = 4$, or 1.2 mm distance, they would collect 100% of 2.3 nm Ag nanoparticles. Considering our impactor operates at 0.53 mTorr, that Au has a higher density than Ag and therefore more momentum, and that our nanoparticles are mostly agglomerated and thus have a higher aerodynamic mobility diameter (>5 nm), we expect better collection efficiency in this system. We can therefore safely assume a 100% collection efficiency at all tested heights. This assures that we are not measuring collection efficiency variations due to operating conditions or alignment errors but solely mass output changes. It also improves the operating range of the deposition method.

3.5. Density results

Density is mass over volume, so we can use our previously acquired mass values to calculate the density of a deposit. All we need is a way to determine the volume of a deposit. Unfortunately, this is, again, not straightforward for thin, porous films. Here we show a method to do this and present the densities we obtained using this method. By dividing this value by the density of the bulk material, we create a relative density, which in the case of porous solids is the porosity.

3.5.1. Profile measurement

The thickness of a single deposit on a QCM, combined with the large surface area to be measured, make it challenging to measure its volume accurately. Mechanical profilometers only measure a line, and optical profilometers are ill-suited for thin, porous films due to scattering effects or semi-transparency. Therefore, it is necessary to deposit a thicker sample on another substrate immediately after a QCM measurement. For this, a line of 3 mm was printed at 0.5 mm min^{-1}. A Dektak 150 physical profilometer with a 12.5 μm stylus was used to measure the cross-sectional area of this line, and by multiplying this area by 0.5 mm, we obtained a volume for one minute of deposition.

Figure 3.8 shows one of these cross-sections projected on a SEM image. The mean volume of a sample made at 5 mA and 1 mm nozzle distance is $4.46 \times 10^{-8} \pm 1.82 \times 10^{-8} \mu m^3$. The typical shape of a printed line has Gaussian slopes and a flattened off peak. Shorter deposition time or smaller nozzles give an almost perfect Gaussian cross-section. The deposits are not completely symmetrical due to turbulence in the gas jet and imperfections in the nozzle. In the optical microscope image, many black specs are scattered on the deposit, which are brighter spots in the SEM image. These specs are large clusters of nanoparticle debris which accumulate over time. Their origin is unclear, but such clusters are rare at high printing speeds, suggesting they are a byproduct of the deposition process.
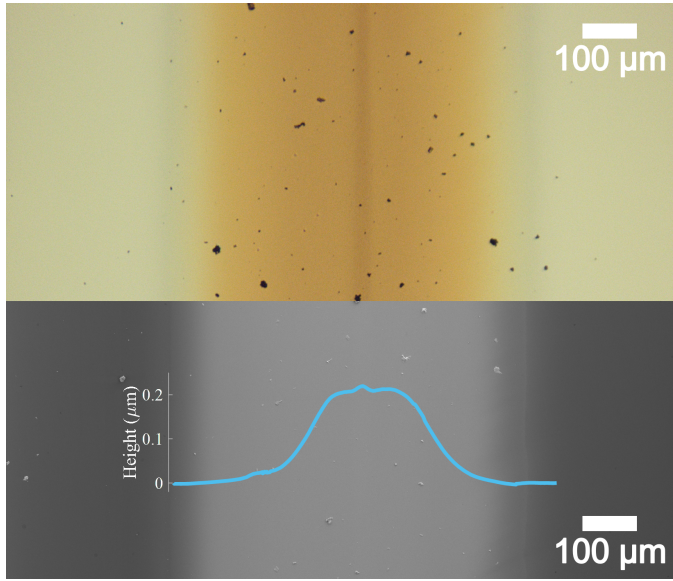
Figure 3.8: Compound image of an optical and scanning electron microscope image (taken at 5 kv) of a printed line on an Al surface. In blue is the average profile of two profile measurements overlaid on the SEM image with the same horizontal scale and at the approximate location. Nozzle distance of 1 mm, 0.5 mm min^{-1}. writing speed, 5 mA generator current.

3.5.2. POROSITY RESULTS

The porosity, Θ_p, of a solid is defined as the volume fraction that is not occupied by the material itself, but by a liquid, air, or vacuum: $\Theta_p = V_{film}/V_{total}$. Often, the volume of the solid is not known, because it can be difficult to quantify the pore volume inside a material. In this case, the relative density can be used:

$$\Theta_p = 1 - \rho_{film}/\rho_{Au} \tag{3.12}$$

ρ_{film} is the density of the film and ρ_{Au} the density of bulk gold, 19.32 g cm^{-3}.

Figure 3.9 shows samples printed at different generation currents. The slope of the trendline is the density: 15.95 g cm^{-3}. This gives us a porosity of $\Theta_p = 0.18$. Considering these samples were made with different generation settings on different days, and all show a similar density indicates the tested experimental conditions have barely an effect on the density. If we look at spark ablation theory (see chapter 2), the settings we adjusted do not change the nanoparticle size distribution much and mostly change the generation rate. The agglomerate structure should therefore be similar for all samples, and they should then form a similar porous structure. Furthermore, if the volume stays proportional to the mass added, the porosity of the layer must be constant in all stages of the film growth.

SEM images such as the ones in Figure 3.10 support this concept of a porosity independent of film thickness. We can see a continuous, rather dense film with no apparent
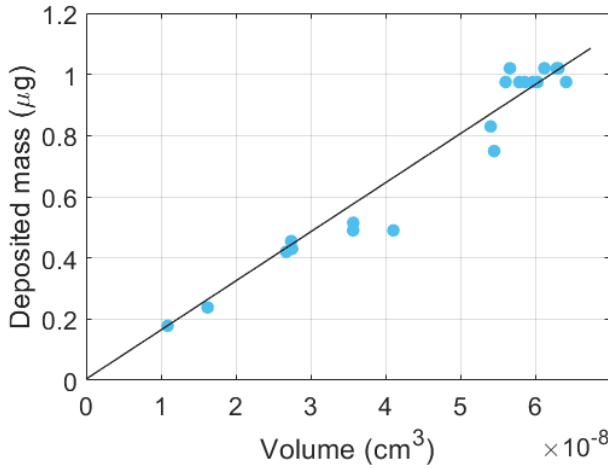
Figure 3.9: Deposited mass plotted versus measured volume of a one minute deposit. All tested generation currents and all nozzle distances are displayed here. A good linear fit through zero (R^2=0.95) shows the density is independent of the deposition settings.

change in density over its height. Previous models on impaction and density show much higher porosities. Lindquist et al. [28] and Mädler et al. [29] modelled ballistic deposition of equally sized spheres and calculated a porosity of 0.84. There are several notable differences between their models and the deposition done here that can explain the discrepancy with the results obtained here. They assume unagglomerated equal-sized spheres without inter-particle interactions. This are logical simplifications to make the modelling less computational intensive, but will give differences with reality. Lindquist et al. identified three regions with different porosities in their films. [28] Region I (close to the substrate) and III (the surface) are finite in size, but the middle region II keeps growing as the layer thickens. With increasing film height, the porosity of region II will start to dominate. The final reported porosity eventually approaches that of region II, but they note that at the beginning of deposition, up to 50 particle radii, when most of the film is in region I, the film approaches zero porosity.

For our films, this corresponds to 300-500 nm, higher than the peak in fig. 3.8. Hence, if we apply Lindquist's model to our process, the samples should have a porosity significantly smaller than 84%, and that porosity should actually increase while the layer grows. However, our experiment indicates that the layer density and therewith its porosity is constant. We believe that the lacking match between the simulations cited and the experiment originates from the fact that the process of impaction causes compaction of the film. Intuitively, a constant porosity induced by impaction pressure is not surprising, because portions with a higher porosity are more fragile and are compacted more strongly.

Additionally, if the impaction energy is high enough, the kinetic energy can heat and deform the nanoparticle upon impact and induce sintering. [23, 30] The models do
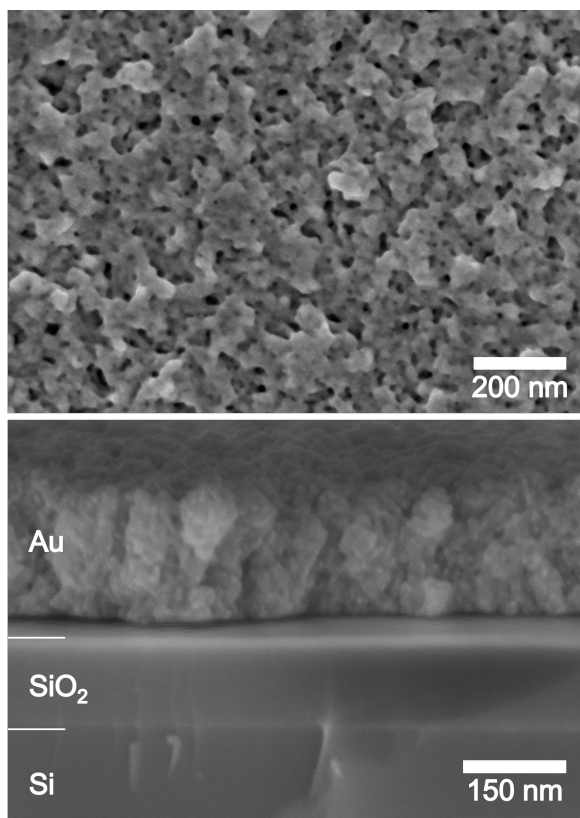
Figure 3.10: Tilted SEM images (at 5 kV) of a line (1 mm min^{-1}., 1 mm nozzle distance, 5 mA generator current). The top image shows a high degree of nanoparticle coalescence and a porous structure on the surface. The bottom image shows a cross-section of a cleaved sample. The Si and SiO$_2$ layers are marked and labelled. This nanoparticle film shows a 150 nm thick uniform film consisting of a dense nanoparticle structure.

not include any compaction or deformation, but the pristine surface of spark ablation generated Au nanoparticles make sintering likely upon impact. The surface atoms are mobile and reactive due to the absence of any surfactants or contaminants to stabilize them. The SEM images in Figure 3.10 support this. They show the nanoparticles have extensively coalesced and formed a dense network of nearly indistinguishable primary nanoparticles. The golden colour of the films, visible in Figure 3.8, also indicates that the nanoparticles are fused together and optically act as bulk gold. Unsintered agglomerates of 5 nm 20 nm Au nanoparticles would appear black. [25]

3.6. Conclusions and outlook

The method described in this chapter enables an accurate measurement of the deposition rate of nanoporous thin films. It was found that the deposition rate scales linearly with generation current in the spark ablation generator, as the theory described previ-

ously. There is no deposition rate change at different heights, validating the method up to 1.5 mm nozzle distance, but further distance are likely valid too, but not commonly used. Furthermore, after extraction of the volume, the density was calculated and was found to be 15.95 g cm^{-3}, or $\Theta_p = 0.18$, at all settings tested here. It is shown the films have a constant porosity independent of film thickness.

The porosity is significantly lower than previous models predicted and we attribute this discrepancy to compaction and sintering of the film during deposition. The simulations do not include any restructuring of the film, but our results show that at supersonic impaction, there is extensive restructuring. The fractal-like structures reported in those models are not seen here, because they primarily form in softer depositions, i.e. at lower impaction speeds.

The setup presented here uses cheap, off-the-shelf components that are readily available and straightforward to integrate in any impaction setup. Now that mass and density of printed nanoporous Au films are measurable, this method can be validated and applied to different metals, oxides or ceramic nanoparticles. This data can then be used to have more reproducible results or even in process control.

Further improvement of the method could be achieved by improving the sensitivity, potentially creating real-time rate monitoring. This can be achieved with optimized code and a more sensitive QCM. Better integration into a deposition chamber can enable process control during the printing of a sample. To achieve this, one needs a QCM that can be coated by a parallel (set) of calibrated, low throughput nozzles in the deposition chamber.

REFERENCES

[1] H. J. van Ginkel, S. Vollebregt, A. Schmidt-Ott, and G. Q. Zhang, *Mass and density determination of porous nanoparticle films using a quartz crystal microbalance,* Nanotechnology **33**, 485704 (2022).

[2] W. Yu, C. Batchelor-McAuley, Y.-C. Wang, S. Shao, S. M. Fairclough, S. J. Haigh, N. P. Young, and R. G. Compton, *Characterising porosity in platinum nanoparticles,* Nanoscale **11**, 17791 (2019).

[3] P. Sinha, A. Datar, C. Jeong, X. Deng, Y. G. Chung, and L.-C. Lin, *Surface area determination of porous materials using the brunauer-emmett-teller (BET) method: Limitations and improvements,* The Journal of Physical Chemistry C **123**, 20195 (2019).

[4] R. D. Kolasinski, J. E. Polk, D. Goebel, and L. K. Johnson, *Carbon sputtering yield measurements at grazing incidence,* Applied Surface Science **254**, 2506 (2008).

[5] M. Leskelä and M. Ritala, *Atomic layer deposition (ALD): from precursors to thin film structures,* Thin Solid Films **409**, 138 (2002).

[6] G. Sauerbrey, *Verwendung von schwingquarzen zur wëgung dünner schichten und zur mikrowëgung,* Zeitschrift für Physik **155**, 206 (1959).

[7] C. van der Steen, F. Boersma, and E. C. van Ballegooyen, *The influence of mass loading outside the electrode area on the resonant frequencies of a quartz-crystal microbalance,* Journal of Applied Physics **48**, 3201 (1977).

[8] E. Benes, *Improved quartz crystal microbalance technique,* Journal of Applied Physics **56**, 608 (1984).

[9] C. Lu and O. Lewis, *Investigation of film?thickness determination by oscillating quartz resonators with large mass load,* Journal of Applied Physics **43**, 4385 (1972).

[10] G. Fischerauer and F. L. Dickert, *A simple model for the effect of nonuniform mass loading on the response of gravimetric chemical sensors,* Sensors and Actuators B: Chemical **229**, 618 (2016).

[11] Q. Chen, S. Xu, Q. Liu, J. Masliyah, and Z. Xu, *QCM-D study of nanoparticle interactions,* Advances in Colloid and Interface Science **233**, 94 (2016).

[12] H. Jiang and L. Tang, *Uniformization of QCM's mass sensitivity distribution by optimizing its metal electrode configurations,* IEEE Sensors Journal **21**, 9008 (2021).

[13] P. Sun, Y. Jiang, G. Xie, X. Du, and J. Hu, *A room temperature supramolecular-based quartz crystal microbalance (QCM) methane gas sensor,* Sensors and Actuators B: Chemical **141**, 104 (2009).

[14] B. Ding, J. Kim, Y. Miyazaki, and S. Shiratori, *Electrospun nanofibrous membranes coated quartz crystal microbalance as gas sensor for NH3 detection,* Sensors and Actuators B: Chemical **101**, 373 (2004).

[15] L. Morelli, F. Ricciardella, M. Koole, S. Persijn, and S. Vollebregt, *Functionalisation of multi-layer graphene-based gas sensor by au nanoparticles,* in *4th International Conference nanoFIS 2020 - Functional Integrated nanoSystems* (MDPI, 2020).

[16] K. Bonroy, J.-M. Friedt, F. Frederix, W. Laureyn, S. Langerock, A. Campitelli, M. Sára, G. Borghs, B. Goddeeris, and P. Declerck, *Realization and characterization of porous gold for increased protein coverage on acoustic sensors,* Analytical Chemistry **76**, 4299 (2004).

[17] I. Mannelli, M. Minunni, S. Tombelli, and M. Mascini, *Quartz crystal microbalance (QCM) affinity biosensor for genetically modified organisms (GMOs) detection,* Biosensors and Bioelectronics **18**, 129 (2003).

[18] V. Marple, K. Rubow, G. Ananth, and H. Fissan, *Micro-orifice uniform deposit impactor,* Journal of Aerosol Science **17**, 489 (1986).

[19] S. V. Hering, *Calibration of the QCM impactor for stratospheric sampling,* Aerosol Science and Technology **7**, 257 (1987).

[20] M. Chen, F. J. Romay, L. Li, A. Naqwi, and V. A. Marple, *A novel quartz crystal cascade impactor for real-time aerosol mass distribution measurement,* Aerosol Science and Technology **50**, 971 (2016).

[21] X. Huang, Q. Bai, J. Hu, and D. Hou, *A practical model of quartz crystal microbalance in actual applications,* Sensors **17,** 1785 (2017).

[22] N. S. Tabrizi, M. Ullmann, V. A. Vons, U. Lafont, and A. Schmidt-Ott, *Generation of nanoparticles by spark discharge,* Journal of Nanoparticle Research **11,** 315 (2008).

[23] T. Pfeiffer, J. Feng, and A. Schmidt-Ott, *New developments in spark production of nanoparticles,* Advanced Powder Technology **25,** 56 (2014).

[24] J. Feng, L. Huang, L. Ludvigsson, M. E. Messing, A. Maisser, G. Biskos, and A. Schmidt-Ott, *General approach to the evolution of singlet nanoparticles from a rapidly quenched point source,* The Journal of Physical Chemistry C **120,** 621 (2015).

[25] A. Schmidt-Ott, *Spark Ablation: Building Blocks for Nanotechnology*, 1st ed., edited by A. Schmidt-Ott (Jenny Stanford Publishing, 2020).

[26] J. Feng, G. Biskos, and A. Schmidt-Ott, *Toward industrial scale synthesis of ultra-pure singlet nanoparticles with controllable sizes in a continuous gas-phase process,* Scientific Reports **5** (2015), 10.1038/srep15788.

[27] J. F. de la Mora and A. Schmidt-Ott, *Performance of a hypersonic impactor with silver particles in the 2 nm range,* Journal of Aerosol Science **24,** 409 (1993).

[28] G. J. Lindquist, D. Y. Pui, and C. J. Hogan, *Porous particulate film deposition in the transition regime,* Journal of Aerosol Science **74,** 42 (2014).

[29] L. Mädler, A. A. Lall, and S. K. Friedlander, *One-step aerosol synthesis of nanoparticle agglomerate films: simulation of film porosity and thickness,* Nanotechnology **17,** 4783 (2006).

[30] C. Peineke, *Production and deposition of well defined aerosol nanoparticles for studies of basic properties*, Ph.D. thesis, Delft University of Technology (2008).

3

4

PRINTED CONDUCTING NANOPARTICLE FILMS

Measure what is measurable, and make measurable what is not so.

Galileo Galilei

Printed conducting films can be applied in several areas. In this chapter, several such applications are explored with a particular focus on the conductive properties of nanoporous gold films. Spark ablation has an advantage in this field because of its flexibility in printed materials and surfaces it can print on. This makes it a versatile method with good potential to be scaled up and used for printed electronics or additive manufacturing.

Section 4.3 has been published in H.J. van Ginkel et al. *High step coverage interconnects by printed nanoparticles*, EMPC conference, 2021. [1] Section 4.4 has been published in X. Ji et al. *Patterning of fine-features in nanoporous films synthesized by spark ablation*, IEEE NANO Conference, 2022. [2]

4.1. INTRODUCTION

THIS chapter first showcases the capability of the impaction printer to print lines of Au nanoparticles and analyses their electric performance. It then follows with an application of these lines as interconnection technology for packaging or vertical integration. Lastly, it shows a method to further miniaturize the deposits when the eventual limit of a printer is reached. Every printer has a resolution limit, so lithography is still the best way to reach sub-micrometer dimensions.

PRINTED ELECTRONICS

Closely related to die attach materials is the printing of conducting lines. Here, nanoparticles are deposited using a printing system to create conducting traces on printed circuit boards, chips, or other (flexible) substrates to connect components. Printed electronics is particularly interesting as an additive manufacturing technology to print circuits, antennas, or interconnects on soft or flexible substrates, uneven or rough surfaces, or chip packages. [3–6] Examples of such printed devices are shown in Figure 4.1. Additionally, integration with 3D printing technology could enable electrical components in 3D printed parts. [3, 7]
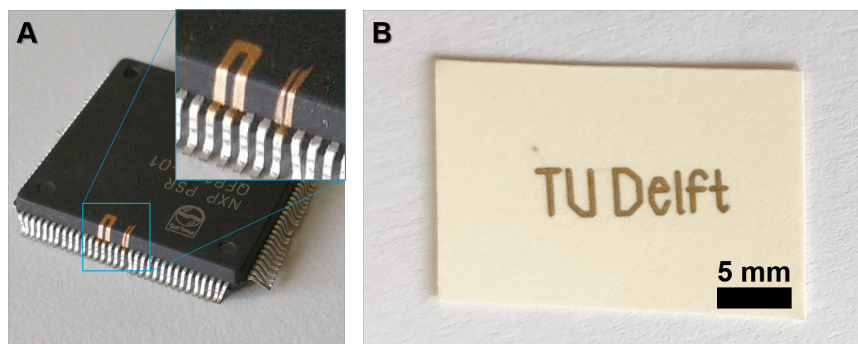

Figure 4.1: Printed structures made by spark ablation and impaction printing. A) Au lines printed on a packaged chip. B) 'TU Delft' printed on paper.

The most popular materials for printed electronics are the noble metals Cu, Ag, and Au due to their high conductivity and low oxidation rate and carbon-based materials like graphene or graphite. They are primarily applied in inks or pastes that protect them from agglomerating and oxidation. A simple and old method to print large areas with ink is screen printing, where you press a nanoparticle paste into a mould (screen) placed on the substrate. This is then cured, and after the removal of the mould, the pattern remains. This works well on flat surfaces and can coat large surfaces efficiently. The drawback is the large feature size, but using a photoresist as a screen, one can improve this.

Using nanoparticle inks makes this technology compatible with ink-jet printing, an already mature technology. Ink-jet printing is cheap, scalable and precise but requires careful formulation of the inks. Viscosity, drying rate, surfactant amount and other parameters need to be tailored for the ink to perform as desired. This limits what can be

printed, but with the correct ink, printing is fast. A gas-based jet printing method has the same capability as ink-jet printing but can print pure particles and will not wet the surface.

4.2. PRINTED CONDUCTING FILMS

4.2.1. PRINTING GOLD

As one of the easiest metals to ablate and because it does not oxidize, gold is one of the most popular metals to experiment with in spark ablation. It is also one of the most conducting metals, only surpassed by copper and silver. All of this makes it a prime subject to print conductive lines with. The only downside is its prize, but due to the small masses needed in research, this is of no concern. For large scale production, it is lucrative to develop Cu-based materials, which is cheaper and would perform better (provided it does not oxidize significantly).

One parameter to include is the cross-sectional area of printed Au lines. Figure 4.2 shows the relation between the nozzle distance and the line shape. The lines all have a Gaussian profile that grows wider but lower with increased nozzle distance due to the conical shape of the jet. The cross-sectional area stays the same for all heights because the mass deposition rate stays the same at these printing heights.
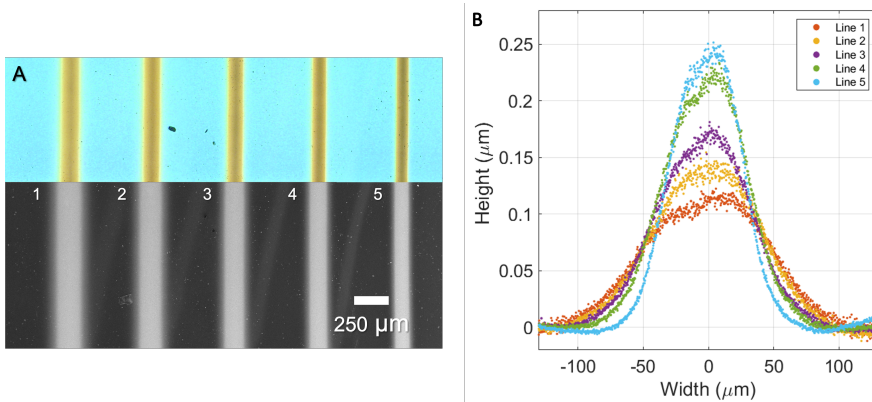

Figure 4.2: A) Overlay of optical (top) and SEM (bottom) micrographs of five printed Au lines printed with different nozzle heights ranging from 1.0 mm (line 1) to 0.2 mm (line 5) with 0.2 mm increments. B) The height profile of these five lines. Th profiles match a Gaussian fit and with increasing height, the width of the line increases, but the height of the line decreases. Lines printed with 8 mA under $1 \, \mathrm{l \, min.^{-1}}$ N_2 flow using the $0.1 \, \mathrm{l}$ $\mathrm{min.^{-1}}$ nozzle and $1 \, \mathrm{mm \, min.^{-1}}$ nozzle speed.

Table 4.1 shows the cross-sectional area and conductivity of eight lines with various settings. A few trends can be observed from this data. Firstly, a higher printing speed logically decreases the thickness of the line and its conductivity. Secondly, the nozzle height has little effect on the line area, but as seen in Figure 4.2, it does change the shape. Towards the edges of a line it gets so thin that at some point, the nanoparticles are less connected with each other and the conductive path becomes longer until there is no percolating path. In other words, the edges have a higher resistance than the core of a line.

Line with identical area can thus have different resistivities depending on their shape. We can see this in line 6, which is less wide and has a much lower resistivity. Lastly, making the lines thicker does not significantly affect the resistivity. This can be explained by the reduced contribution of the film's edges when printing thicker films. The resistivity of the core starts to dominate, which, with the settings used here, is around $5.3 \times 10^{-7}\Omega$ m. Compared to the resistivity of bulk Au of $2.44 \times 10^{-8}\Omega$ m, this is roughly 22 worse.

Line	Nozzle distance (mm)	Writing speed (mm s^{-1})	Line stacks	Area unannealed (μ^2)	Area annealed (μ^2)	Area change	ρ unannealed (Ω m)	ρ annealed (Ω m)	ρ change
1	1	1	1	34.0	-	-	$5.3 \times 10^{-7} \pm 5.4 \times 10^{-8}$	-	-
2	1	2	1	19.7	-	-	$1.1 \times 10^{-6} \pm 2.0 \times 10^{-7}$	-	-
3	1	5	1	-	-	-	-	-	-
4	1	1	1	33.7	32.7	−3%	$5.8 \times 10^{-7} \pm 6.8 \times 10^{-8}$	$5.5 \times 10^{-7} \pm 1.7 \times 10^{-7}$	−6%
5	1.5	1	1	32.7	34.5	5%	$5.6 \times 10^{-7} \pm 6.7 \times 10^{-8}$	$4.9 \times 10^{-7} \pm 7.4 \times 10^{-8}$	−13%
6	0.5	1	1	31.3	33.2	6%	$4.8 \times 10^{-7} \pm 2.8 \times 10^{-8}$	$3.7 \times 10^{-7} \pm 3.0 \times 10^{-8}$	−23%
7	1	1	2	54.7	46.9	−14%	$5.2 \times 10^{-7} \pm 6.6 \times 10^{-8}$	$2.1 \times 10^{-7} \pm 2.2 \times 10^{-8}$	−60%
8	1	2	4	55.1	43.4	−21%	$5.1 \times 10^{-7} \pm 4.0 \times 10^{-8}$	$2.0 \times 10^{-7} \pm 2.0 \times 10^{-8}$	−60%

Table 4.1: Results of 8 Au lines printed with varied nozzle heights, writing speeds, or with multiple lines stacked on top of each other. Lines 4, 5, and 6 have been annealed at 100 °C for 1 minute, and lines 7 and 8 at 200 °C for 1 minute. Resistance was measured at 4 points on the line and averaged. Cross-sectional area was measured at three points along the line and averaged. The profile of line 3 was too thin to be accurately measured with the profilometer.

4.2.2. EFFECT OF ANNEALING
The samples made using this spark ablation setup have a porosity of 0.18, so the porosity of the film has a disproportionately large effect on the resistance of the film. [8] Counteracting this effect can be beneficial for many applications where higher conductivity is required. This can be achieved by annealing to improve the interparticle contact or even partial melting of the film. Lines 4 to 8 in table 4.1 have been annealed at 100 or 200 °C and show significant improvement in their conductivity. Lines 4, 5, and 6 were annealed at 100 °C and show no significant change in their cross-sectional area, so they have not melted. The reduction in resistance is entirely due to better interparticle contact. Interestingly, both the closer and further nozzle distance show a better conductivity change than the 1 mm nozzle distance line (line 4). For line 6, this is expected since its smaller and higher profile should give a denser and better-connected nanoparticle network when annealed. The wider line 5 should not exhibit this, but it can be speculated that the edges are conducting better after annealing, so annealing might improve line 5 more than line 4.

100 °C annealing does not change the area significantly and SEM images support this. There is no discernible difference in microstructure between image A and B in Figure 4.3. However, in Figure 4.3C, we can clearly see that annealing at 200 °C nearly fully fuses the particles together. Annealing at 200 °C therefore changes the area significantly due to partial melting or coalescence of the nanoparticles. This has a directly proportional effect on the conductivity, but the conductivity change is higher with 60%, so the interparticle connection is now drastically improved too. The conductivity of lines 7 and 8 are only eight times worse than bulk Au, comparable to lead. This comes at the cost of the special properties of nanoporous materials, so annealing to this extent is only recommended when conductivity is the crucial property to maximize.
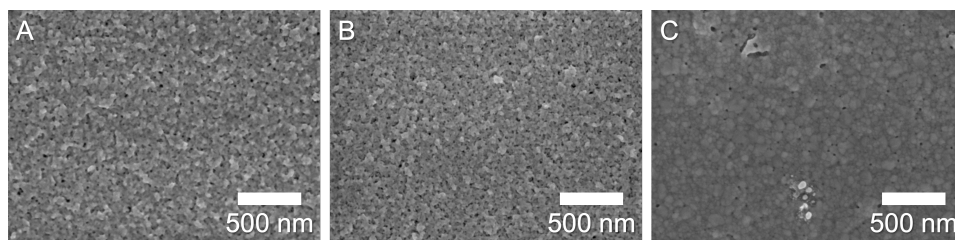
Figure 4.3: SEM images of the lines 1 (A), 4 (B), and 7 (C) of table 4.1. We can see no clear difference between A and B, but the nanoparticles in C have nearly fully coalesced.

4.3. INTERCONNECT PRINTING

Interconnects, the components that connects chips to their packaging or chips below are an integral part of any semiconductor packaging process. Due to the increased versatility in microelectronic materials and applications, there is a need for interconnection technologies in niche applications. Flexible electronics, harsh environment electronics and bioelectronics provide unique interconnection challenges.

The most common interconncet technology is wire-bonding. This process uses a wire to connect the top of the chip to its surrounding. Wire-bonding requires temperatures above 150 °C or ultrasonic power to create a good weld on the bond pad. Flexible materials (often polymer or paper based) do not survive such temperatures and are too soft for ultrasonic pressure. [9–11] Alternative, more gentle methods are required to work with such materials. Spark ablation with impaction printing is one potential candidate. Here, we show the successful deposition of a conducting line on the side of a chip connecting it to the material it is bonded to.

4.3.1. MATERIALS AND FABRICATION

SUBSTRATE PREPARATION

To fabricate the stacked samples, Si wafers were insulated with 300 nm SiO_2 by thermal oxidation. After lithography, a 10/100 nm Cr/Au layer was deposited, and lift-off was performed to finish the patterning. The wafers were then diced in 10 × 10 or 20 × 20 mm dies and cleaned with acetone, isopropanol, and demineralised water.

The interconnection process is demonstrated on two substrates: polished Si wafer dies and paper (PowerCoat HD, Arjowiggins Creative Paper. The 10 mm dies were thermocompressively fabricated dies were bonded on the 20 mm pieces using SU-8 bonding polymer. [12] They were cured at 120 °C and 1 kN for 2 hours. These samples will be referred to as silicon-on-silicon (SoS) samples. For the silicon-on-paper (SoP) samples, the 10 mm dies were bonded to 15 × 15 mm pieces of paper using cyanoacrylate adhesive (3M). No additional curing was required for this adhesive. The resulting structure are shown in Figure 4.4 Both top substrates have identical structures to connect two sides of the die. This simplifies probing during conductivity measurements.

Au NPs were generated at 8 mA and 1 kV under N_2 atmosphere and printed using the 0.1 L min.$^{-1}$ nozzle. The samples were placed at a constant 0.5 to 2.0 mm distance to the
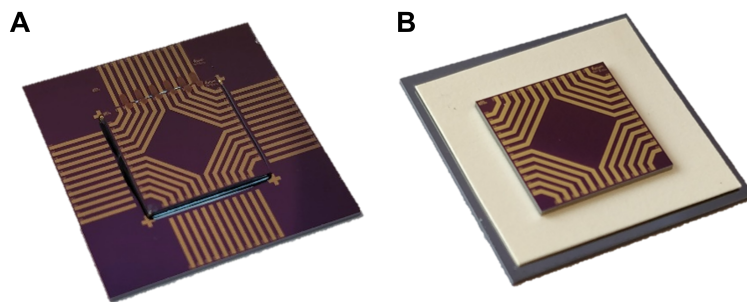
Figure 4.4: Photographs of the substrates. A) Silicon on silicon with a few printed lines on the top edge. B): Silicon on paper sample taped to a 20 × 20 mm silicon die for easier handling.

4

nozzle at a 20° or 45° angle to print all sides in one deposition. This is shown in Figure 4.5, the nozzle adjusts for the change in height to ensure nozzle-to-substrate distance is constant. Writing speed was 1 mm min.$^{-1}$.
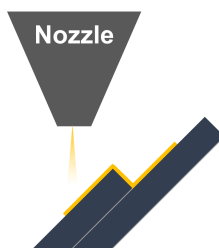

Figure 4.5: Schematic of printing at a 45° angle.

4.3.2. Results

Structure and morphology

Figure 4.6 shows the final products with printed conducting lines on some pads. The lines show good surface conformity and most notably, are continuous at the die edge, a 90° corner, as best visible in the SEM images of Figure 4.7B and C. The film is sensitive to the surface morphology and features caused by the dicing are visible in the film. The dicing grooves left by the blade on the side of the top die create a tilted layered pattern in the nanoparticle film. Figure 4.7A also shows an excess of SU-8, which resulted in a curved surface at the gap between the two dies. This creates a smoother path for the film, which helps the film's continuity. The microstructure of the printed films is identical to the ones shown in chapter 3 and can be expected to have similar density. Although this was not verified for this process, the generation and deposition conditions are almost identical.

The SoP samples showed similar conformity and structures as the SoS samples, with
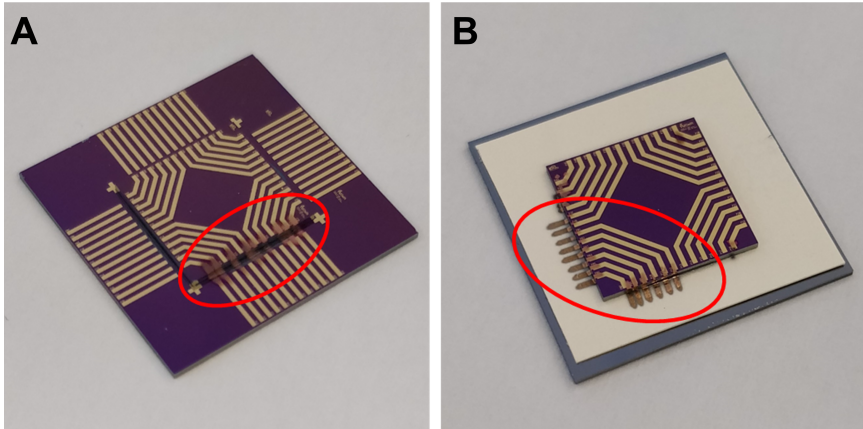
Figure 4.6: Photographs of SoS (A) and SoP (B) samples with printed Au deposits circled in red.
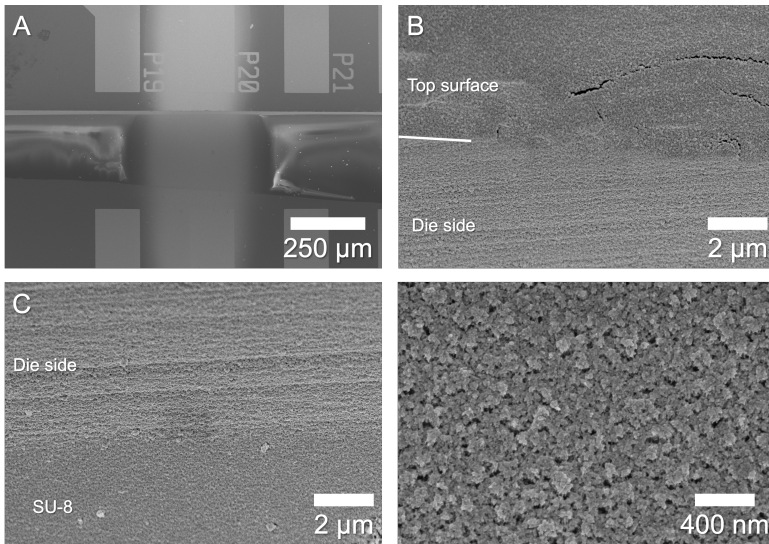

Figure 4.7: SEM images of SoS samples taken at a 25° angle, fabricated with a 20° tilt. A) A SoS interconnect line. B) Close-up of the top die edge showing the dicing grooves. The white line marks the exact location of the edge. C) Close-up of the die edge to the Su-8 transition area. D) Top view of the Au nanoparticle film on Si showing a dense surface.

logically identical morphology at the top die edge, as visible in Figure 4.8A and B. The conformity of the nanoparticle film is so high that, as seen in Figure 4.8D, it coats the fibres of the paper uniformly. This ensures a continuous and conducting film on the paper.
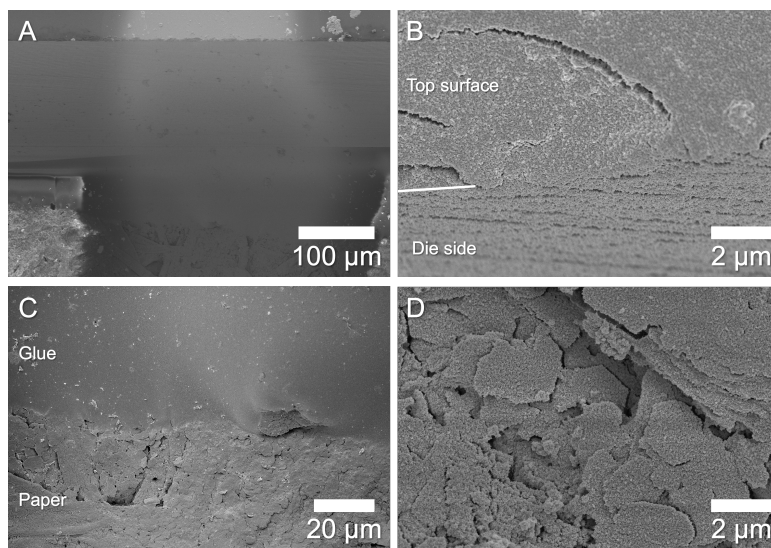

Figure 4.8: SEM images of SoP interconnects taken at a 25° angle fabricated with a 20° tilt. A) A SoP interconnect line. B) Close-up of the top die edge showing the dicing grooves. The white line marks the exact location of the edge. C) Close-up of the glue to the paper transition area. D) A section of the paper showing the high nanoparticle film conformity on the fibers.

Conductivity

The lowest resistance was found on SoS samples with a 0.5 mm printing distance and a 20° sample tilt, with a resistance of 2.97±0.72 Ω. With a mean cross-sectional area of $168\mu m$, this gives a resistivity of 8.3×10^{-5}, so 34 times worse than bulk Au. Compared to the lines printed in section 4.2, this is a nearly 50% degradation in the performance, which must be attributed to the tilted samples. In almost every aspect, the Au nanoparticle lines in this experiment are synthesized identically as the lines described earlier in this chapter. As established in chapter 3, the porosity of these lines should thus be similar too. Due to this, we expect similar conductive behaviour and resistivity inside the film. Printing at an angle should not change the microstructure of the film significantly since compaction is too high for Au under these conditions (see chapter 3). Still, at the sharp corners of the die, the slope changes direction with respect to the printing direction. This could affect the conductivity of the film around the corners. Additionally, the side of the die shows grooves left by the dicing, which could create bottlenecks in the conductive path, reducing the effective conducting cross-sectional area on the die egde.

Broken devices show either an open connection when measured at a single electrode or IV behaviour typical for varistors. This is due to the two opposing Au-Si Schottky diodes that form on the side of the die, as illustrated in Figure 4.9. If a crack forms in

the Au film, the conductive path goes through the silicon, giving a similar response as probing neighbouring electrodes. Despite the high resistance of these Au-Si contacts, all lines on the side of a die are connected through the silicon.
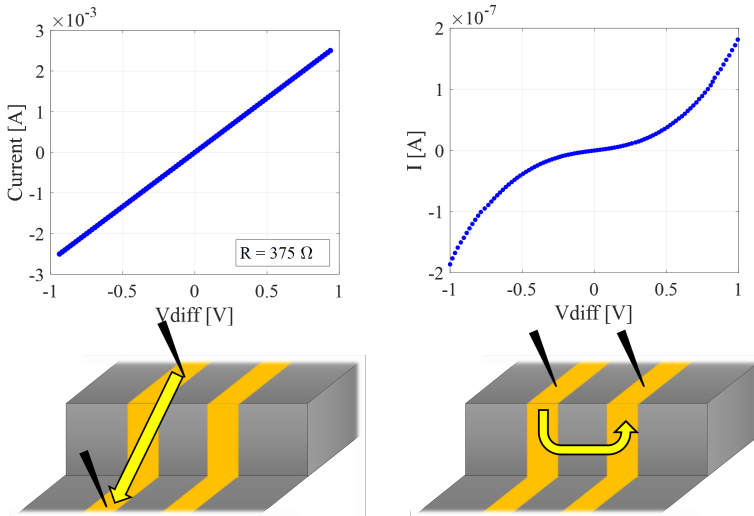

Figure 4.9: IV-curves and diagram of the conductive path across the interconnect for different probing points. A working interconnect shows Ohmic behaviour when probed at the bottom and top line (left two images). Measuring two neighbouring lines gives varistor behaviour due to the Si-Au contacts at the die edge. Although the resistance of these contacts is high, it shorts all contacts on the die edge.

For SoP samples, it was challenging to reliably measure the resistance because probing directly on the NP line on the paper gives unreliable contact. However, repeated measurements on various lines have given a range of 250 to 750 Ω, two orders of magnitude worse than the SoS samples. One factor is that there are no probe pads on the paper, necessitating probing the line directly, which damages it. Secondly, due to the high conformity to the nanoparticle film in combination with the fibrous structure of the film, the conductive path across the paper is significantly longer than on the flat silicon.

FAILURE MODES

SoS interconnects could be reliably manufactured, with a 82% of the 18 fabricated tracks showing good Ohmic behaviour. This is due to the reliable connection to the Au tracks on the die and rigid, flat surface. The main cause of failure was therefore caused by cracking in the SU-8 film or at the transition between the polymer-Si interface, as shown in Figure 4.10A and B. This can be improved with a better bonding process.

For SoP, the adhesive also proved to be a source of failure by, besides the aforementioned failure modes, causing cracking of the silicon of the top die. The cyanoacrylate adhesion to the silicon is so strong that when it shrinks during curing, it causes high enough stress to crack the silicon that no printed interconnect could bridge. Off all SoP interconnects, only 20% showing good Ohmic behaviour.
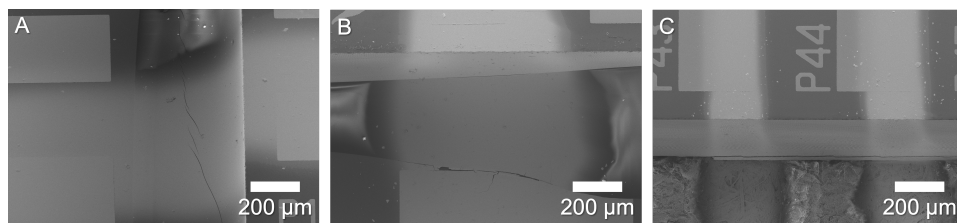
Figure 4.10: SEM images of three failure modes. A) Cracking in the SU-8 adhesive polymer propagating through the Np film. B) Crack at the polymer-to-Si interface. C) Cracking of the Si due to stress caused by the cyanoacrylate adhesive.

DISCUSSION

Impaction printing of spark ablation nanoparticles is a feasible alternative to wirebonding for connecting a die to a package or die below it. The major difficulty for this technology at the moment appears to be a reliable connection at the Si-Si or Si-paper interface. At that 90° corner, the bonding adhesive needs to fill the gap between the two substrates and preferably create a rounded corner. More controlled adhesive application and curing is the straightforward solution to solve this.

A second issue is that conducting substrates can short two printed interconnects due to the absence of an insulating layer. One proposed solution is to coat the edges after dicing with an insulating material. This might be an oxide, but a polymer such as parylene would work too. To characterize the electrical performance without any influence of the substrate, future work should use non-conducting substrates like glass or sapphire. Additionally, patterning contact pads on the SoP samples could improve the resistance measurement quality on the paper samples.

The line width is variable by changing the nozzle distance and nozzle diameter. With the available setup it is currently not possible to go below 100 µm in width, but this is possible with further development. Tilting the nozzle to allow printing at a constant angle (i.e. 0°) relative to the sample surface can improve the coverage of the surface and create more homogenous printing on an edge. This would require extensive upgrades to this setup, but such technology is already applied in conventional 3D printing or robotic coating technology. Our setup is a prototype and although fully functional, improvements on the printing accuracy and reproducibility will improve yield. Newer versions of this nanomaterial printer already have significantly higher accuracy and printing speed.

CONCLUSION

A novel process is demonstrated to complement wire-bonding or VIAs on a wide range of substrates. The process is entirely at room temperature, making it especially suitable for temperature-sensitive and soft substrates. Its high conformity and substrate flexibility allow for application on rough or uneven surfaces. The resistance is not yet high enough for high-fidelity signal transport, but by printing on insulated surfaces or by a short anneal of the nanoparticle film, this can be improved.

4.4. PATTERNING PRINTED FILMS

The application of nanostructured films using deposition methods such as ink-jet printing or aerosol jet printing is cheap and versatile. However, due to fluid dynamics, aerodynamics and printing technology limits, the resolution that such methods can reach is limited. Patterning methods are therefore needed to scale down devices made with nanoporous deposits. Lift-off is a tested method in microfabrication and is a cheap and reliable method to pattern thin films. [13, 14] It works by first patterning a photoresist, then coating the wafer with a film, and finally dissolving the resist, as shown in Figure 4.11. The resolution limit of this method can theoretically the limit of the lithography process, thus making it suitable to scale down nanoporous deposits too. Although lift-off has been applied to nanoporous films, the reliability and reproducibility are still poor. [15]
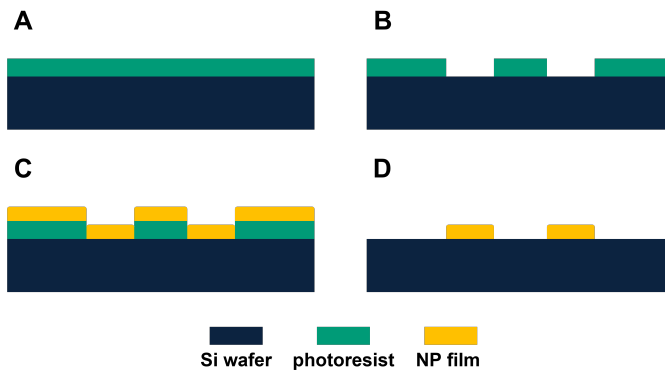

Figure 4.11: Diagram showing the lift-off process. A) Photoresist application; B) Patterning using lithography; C) Nanoparticle film deposition; D) Lift-off of the photoresist.

In these experiments, Au and ZnO nanoparticle deposits made by spark ablation were patterned using lift-off. The lithographically defined patterns were tested down to 0.5 μm resolution. The effect of the process on the film was analysed and the conductivity of a patterned structure was measured.

4.4.1. MATERIALS AND METHOD

The experiments were done using silicon wafers with a 190 nm SiO_2 layer. A 25 nm Ti film was sputtered on this for adhesion. After oxidation in air, this layer oxidizes to TiO_2. 8.5 μm AZ 12XT-20PL photoresist was spin-coated on the wafer and patterned. The nanoparticles were generated using 99.999% Au electrodes or using 99.95% Zn with 0.05% Al. Zn nanoparticles will oxidize quickly, making the final product ZnO. [16] Al doping was used to increase the conductivity of the ZnO film. G1 settings were 1 kV and 8 mA or 4 mA for the Au and Zn electrodes, respectively. The deposition was done using the largest (0.99 L min.$^{-1}$) at our disposal at 1 mm nozzle distance with 1 mm per minute writing speed. Parallel lines were printed with 0.1 mm spacing between them to create rectangular deposits with a relatively uniform height profile. Finally, the lift-off procedure was performed by dissolving the photoresist in n-methyl-2-pyrrolidone (NMP) in

an ultrasonic bath for 30 seconds. The wafers were then rinsed in a demi water bath for several minutes and left to dry in air.

4.4.2. RESULTS

RESOLUTION

After lift-off, no photoresist residue can be seen on the wafer. The figures 4.12 and 4.13 show the patterns before (left side) and after (right side) lift-off. A and B in both figures are resolution checking patterns with decreasing widths and spacing. The gold patterns in Figure 4.12B have fraying around the edges caused by deposition on the side of the photoresist. This phenomenon is called fencing and is problematic because these thin frays frequently bridge the gap between the rectangles. Fencing is not clearly visible in the ZnO patterns, but on closer inspection, the edges show inward curves. The ZnO is considerably thicker than the Au, so the frays are much shorter.

Figure 4.12: SEM images of various Au structures before (left) and after lift-off (right). A and B show resolution check patterns, while D to F show Van der Pauw structures used to measure electrical conductivity.
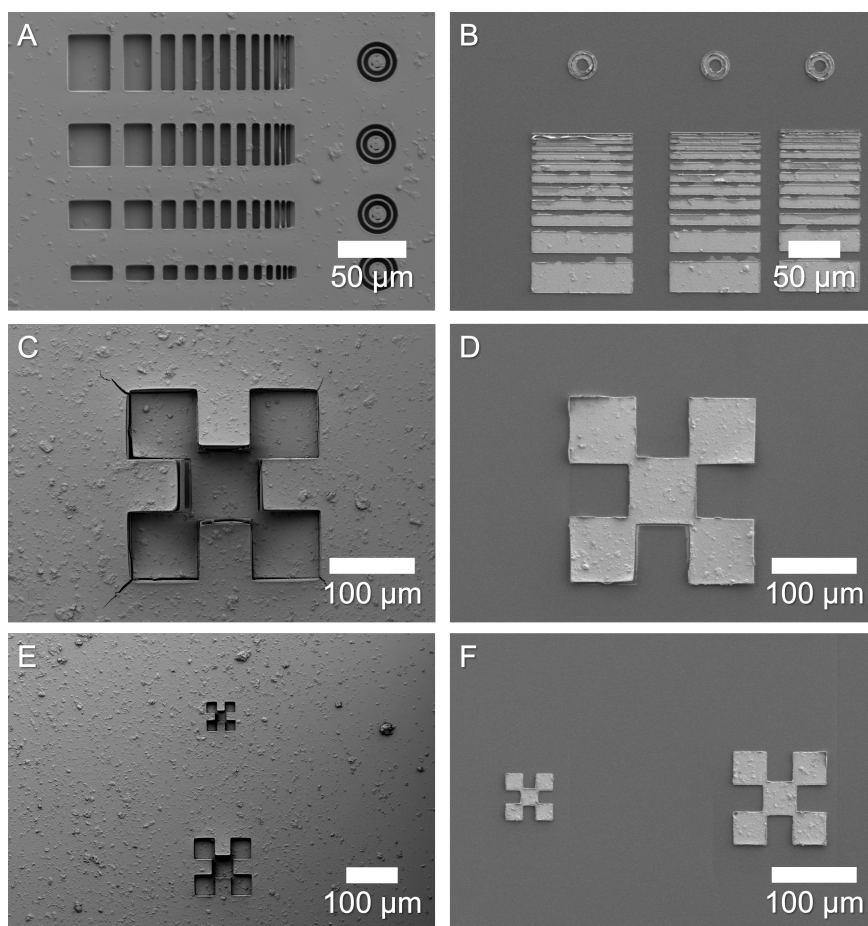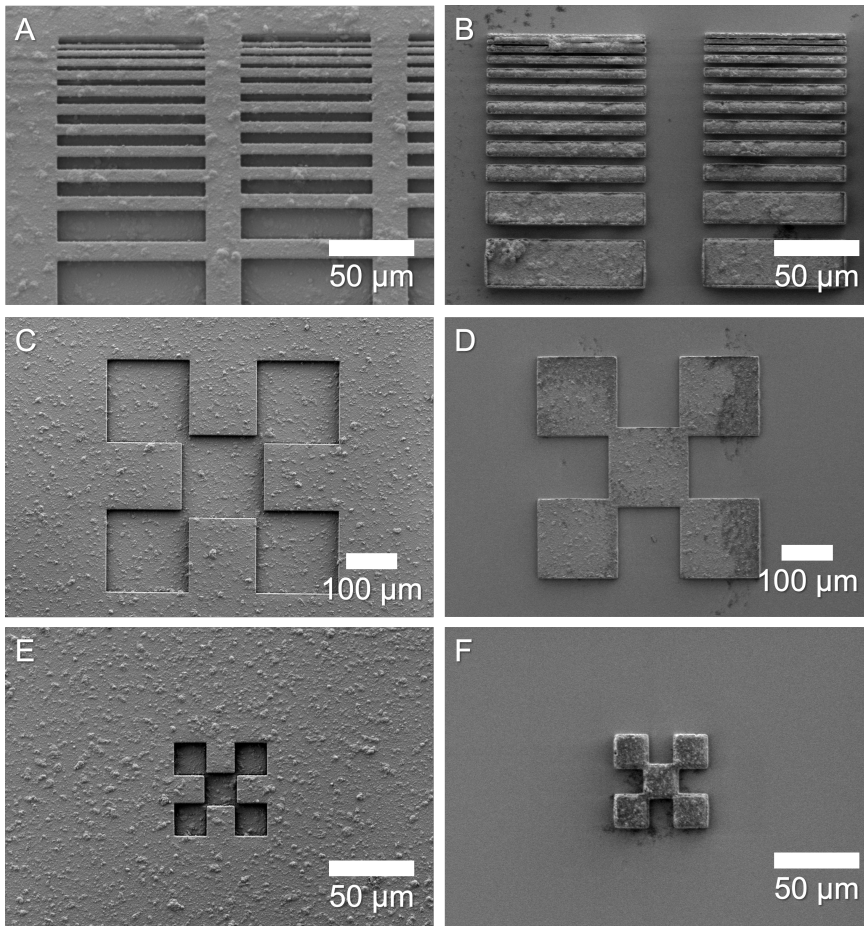
Figure 4.13: SEM images of various ZnO structures before (left) and after lif-off (right). A and B show resolution check patterns, while D to F show Van der Pauw structures used to measure electrical conductivity.
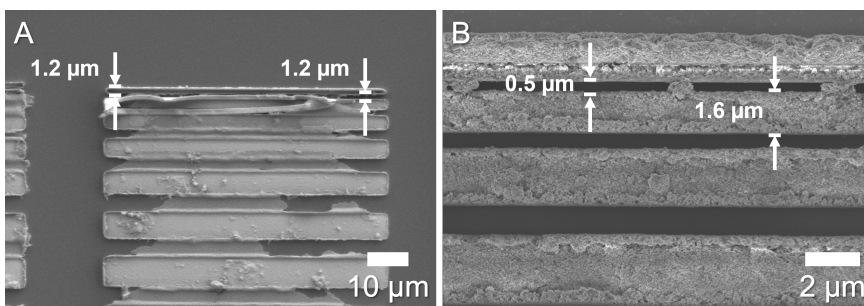

Figure 4.14: SEM images of resolution check patterns showing the minimal achieved resolution after lift-off. A) shows Au patterns, B) shown ZnO

If we zoom in on the resolution check patterns (Figure 4.14), we see that although the gaps are largely covered by the frays that fell over, the smallest features are actually well-defined. The minimal feature size we can identify in the Au patterns is around 1.2 μm and in the ZnO even slightly smaller, at 0.5 μm. It must be noted that the 1.2 and 1.6 μm in these two samples are actually the same feature on the mask, which was drawn to be 1.0 μm wide.

The top strip in this Au sample has washed away due to the poor adhesion of such a thin structure. Thus, The pattern is wider than drawn, which we attribute to fencing obscuring the real edges.

The profile of the Van der Pauw (VDP) structures to measure the conductivity is relatively flat with the exception of large clusters that decorate the surface (see Figure 4.15. These clusters are a byproduct of long depositions and can be minimized by frequent cleaning of the tubing and nozzle or high-speed printing with many repetitions. These clusters are more noticeable in the Au sample since it is much thinner than the ZnO one. The thicker ZnO film is a result of the much higher ablation rate of Zn. The edges of the devices are sharp and straight which is useful for high aspect-ratio structures and achieving high patterning accuracy. We attribute the sharp edges of the resulting structures to a special feature of the impaction printing process applied. As previously shown, impaction printing leads to preferred particle sintering in the vertical direction. [17]

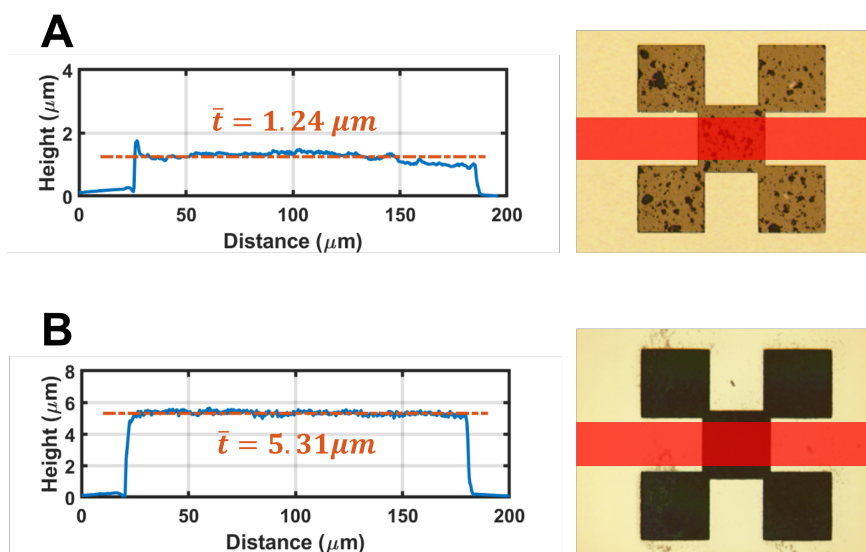Figure 4.15: Cross section height profile of an Au (A) and of a ZnO (B) VDP structure. The data is the average of 100 line profiles in the red area of the micrographs (measured with a Keyence VKX 250 optical profilometer).

Effects on the film

In order for these films to be applied in the same manner as the freshly printed films, it is crucial their nanostructure and purity is preserved. First, the effect of the lift-off process

	Before (μm^2)	After (μm^2)
Au	943 ± 22	922 ± 35
ZnO	404 ± 31	389 ± 31

Table 4.2: Mean cross-sectional area of Au and ZnO lines measured three times on three locations before and after lift-off (measured using a Bruker Dektak 150).

on the cross-sectional area was quantified on printed lines that were not patterned. Table 4.2 shows the cross-section before and after the lift-off process described before. For both Au and Zno lines, the change is minimal: −4% and −2% changes, respectively. This is within the standard deviations of both before and after measurements, so we conclude that the process has no measurable effect on the film cross-sectional area. SEM inspection supports this. Figure 4.16 shows the microstructure of ZnO and Au films before and after lift-off, with no noticeable changes in the structure. The rough, microporous structure of printed nanoparticle films is still intact.
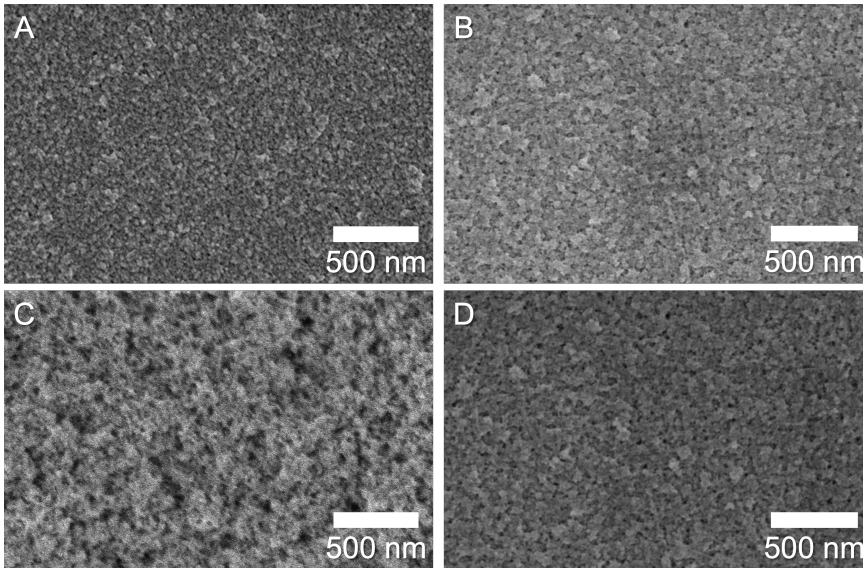
Figure 4.16: SEM images of the microstructure of Au (A and B) and ZnO (C and D) before and after lift-off. Changing due to the bad conductivity of ZnO distorts image C.

CONDUCTIVITY

Lastly, the electrical performance of these films was measured to show the ability to pattern conducting films without performance loss. Since there was no annealing step in this process, the ZnO samples were hardly conducting and the results are not been included here. By applying equation 4.1 to calculate the resistivity of VDP structures with this geometry and filling in thickness $t = 1.24 \mu$m, we can directly measure the resistivity. Using the four-point-probe technique as shown in Figure 4.17, the resistivity was found to be 2.07×10^{-5} Ω cm^{-1}. This is 8.5 times as high as bulk Au (2.44×10^{-6} Ω cm^{-1}, and

not far above that of annealed printed lines (see section 4.2). The similarity to annealed films suggests that the particles have now better electrical contact caused by the lift-off step even though the samples were not heated. The ultrasonic energy might have annealed the samples, but we must also note that these patterns have a high aspect ratio. This means that there are no poorly conducting edges, like the samples in section 4.2, so these patterned samples should already perform better than those.

$$\rho = 4.532 \cdot t \cdot R_A [18] \tag{4.1}$$
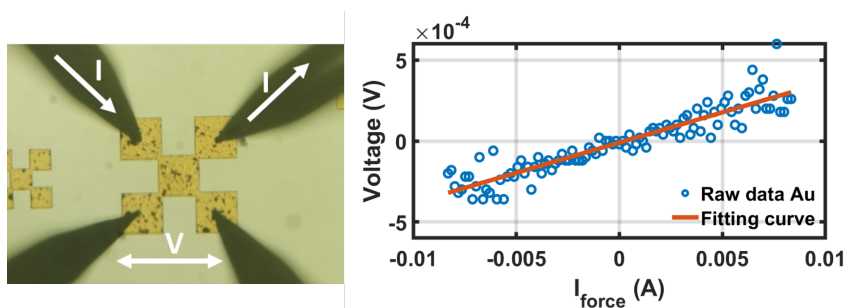
Figure 4.17: Probing setup and corresponding IV curve on the Au VDP structure in Figure 4.15A

CONCLUSIONS
The fabricated nanoporous films were patterned using a conventional lift-off process and a minimal feature size of 1.2 μm was achieved; the effective minimal resolution of the lithography system in this laboratory. The influence of the wet lift-off process on microstructure and thickness was found to be insignificant. Furthermore, the resistivity of the resulting Au nanoporous film was higher than freshly printed features, so mild annealing of the nanoporous film might have occured. Due to the compatibility with modern microfabrication processes, this process provides a solution for the mass production of highly miniaturized nanoporous film-based devices from various materials. It enables the application of these films in integrated devices by creating a large surface-to-volume ratio in a small area.

4.5. SUMMARY
This chapter has shown the applicability of spark ablation generated printed nanoparticle films as a feasible material for printed electronics. In its simplest form, it makes conductive paths that are 22 times less conducting than bulk Au, but after annealing, this can be reduced to 8 times lower. This technology can be employed as an additive manufacturing technique to print conducting lines on a wide range of materials, such as chip packaging, paper, polymers, silicon, and metals. One potential application is printing interconnects on either very hard materials (alternative to TSVs in SiC) or as an alternative to wire bonds on soft materials like paper. This is demonstrated to work on Si samples bonded to silicon or paper and with some optimisation, it could be a good alternative to both TSVs or wirebonds. Lastly, to be better integrated in microfabrication,

better miniaturization is required for these nanoporous films. This was achieved for Au films using a conventional lift-off process which successfully patterned the films to the resolution limit of the lithography tool in our lab. Spark ablation provides a flexible, precise, and back-end compatible methods to apply conducting films on a wide range of substrates and geometries. It can make an excellent additive manufacturing technology to print circuits or interconnects on substrates or places that would otherwise be challenging to fabricate.

4.6. FUTURE PROSPECTS

Despite the successful proof of concept of the feasibility of printing conducting lines presented in this chapter, there is still room for improvement. First and foremost is the move from Au to Ag or even Cu. These materials are cheaper and perform better than gold as electrical conductors but oxidize. Development of a low-oxidation process could furthermore enable more conducting metals or alloys if contamination or other limitations or specifications require it. Secondly, Au is an excellent model material to work with, but can still be much improved. To create a higher conductivity, annealing is necessary, but a "hot deposition" method, where the substrate is heated during deposition, would anneal the nanoparticles during deposition, creating the densest possible film and the highest conductivity, perhaps even at a lower process temperature.

Another interesting avenue to explore is the mechanical properties of these nanoporous films. Their adhesion strength to the substrate and the brittleness of the film itself are valuable properties to quantify to be able to design more complex structures and do more advanced processing on these films without damaging them.

Improvement of the printing equipment would improve the accuracy, speed, and resolution of the patterning process, but parallel processing lines will be required for the mass production of printed electronics using this process. A writing speed of 2 mm min.$^{-1}$ already halves the conductivity, so this process can only write at roughly 1 mm min.$^{-1}$; much too low for mass production. Higher aerosol loading can improve the printing mass output and more powerful generators are being developed to achieve this. [17] However, parallel nozzles must still be used to achieve a meters-per-minute printing speed. Lastly, the mass deposition rate of the equipment varies based on the electrode orientation and alignment and other parameters. This makes the output too inconsistent for reliable production. Integrated mass deposition rate sensors such as the one presented in chapter 3 are a solution to adjust the process parameters for a constant mass output. Still, a better understanding of the spark ablation process is required to improve the process stability.

REFERENCES

[1] H. J. van Ginkel, J. Romijn, S. Vollebregt, and G. Q. Zhang, *High step coverage interconnects by printed nanoparticles,* in *2021 23rd European Microelectronics and Packaging Conference & Exhibition (EMPC)*, IEEE (IEEE, 2021) pp. 1–4.

[2] X. Ji, H. J. van Ginkel, D. Hu, A. Schmidt-Ott, H. van Zeijl, S. Vollebregt, and

G. Zhang, *Patterning of fine-features in nanoporous films synthesized by spark ablation,* in *2022 IEEE 22nd International Conference on Nanotechnology (NANO)* (IEEE, 2022).

[3] J. J. Adams, E. B. Duoss, T. F. Malkowski, M. J. Motala, B. Y. Ahn, R. G. Nuzzo, J. T. Bernhard, and J. A. Lewis, *Conformal printing of electrically small antennas on three-dimensional surfaces,* Advanced Materials **23**, 1335 (2011).

[4] P. Bezuidenhout, S. Smith, K. Land, and T.-H. Joubert, *Inkjet-printed interconnects for unpackaged dies in printed electronics,* Electronics Letters **55**, 252 (2019).

[5] B. K. Tehrani, B. S. Cook, and M. M. Tentzeris, *Inkjet-printed 3D interconnects for millimeter-wave system-on-package solutions,* in *2016 IEEE MTT-S International Microwave Symposium (IMS)* (IEEE, 2016).

[6] T. Seifert, M. Baum, F. Roscher, M. Wiemer, and T. Gessner, *Aerosol jet printing of nano particle based electrical chip interconnects,* Materials Today: Proceedings **2**, 4262 (2015).

[7] H. W. Tan, Y. Y. C. Choong, C. N. Kuo, H. Y. Low, and C. K. Chua, *3D printed electronics: Processes, materials and future trends,* Progress in Materials Science **127**, 100945 (2022).

[8] H. J. van Ginkel, S. Vollebregt, A. Schmidt-Ott, and G. Q. Zhang, *Mass and density determination of porous nanoparticle films using a quartz crystal microbalance,* Nanotechnology **33**, 485704 (2022).

[9] J. Pan and P. Fraud, *Wire bonding challenges in optoelectronics packaging,* in *Proceedings of the 1st SME Annual Manufacturing Technology Summit* (SME, 2004).

[10] J. Chen, D. Degryse, P. Ratchev, and I. De Wolf, *Mechanical issues of Cu-to-Cu wire bonding,* IEEE Transactions on Components and Packaging Technologies **27**, 539 (2004).

[11] M. Murugesan, T. Fukushima, K. Kiyoyama, J. C. Bea, T. Tanaka, and M. Koyanagi, *High-step-coverage cu-lateral interconnections over 100 μm thick chips on a polymer substrate as an alternative method to wire bonding,* Journal of Micromechanics and Microengineering **22**, 085033 (2012).

[12] Kayaku, *SU-8 3000 datasheet* (accessed on 2 November 2020).

[13] G. Klös, A. Andersen, M. Miola, H. Birkedal, and D. S. Sutherland, *Oxidation controlled lift-off of 3D chiral plasmonic Au nano-hooks,* Nano Research **12**, 1635 (2019).

[14] M. Filippidou, M. Chatzichristidi, and S. Chatzandroulis, *A fabrication process of flexible IDE capacitive chemical sensors using a two step lift-off method based on PVA patterning,* Sensors and Actuators B: Chemical **284**, 7 (2019).

[15] B. Zhang, Y. Carisey, A. Damian, R. Poelma, G. Zhang, and H. van Zeijl, *3D inter-connect technology based on low temperature copper nanoparticle sintering,* in *2016 17th International Conference on Electronic Packaging Technology (ICEPT)* (IEEE, 2016).

[16] A. Schmidt-Ott, *Spark Ablation: Building Blocks for Nanotechnology,* 1st ed., edited by A. Schmidt-Ott (Jenny Stanford Publishing, 2020).

[17] T. Pfeiffer, J. Feng, and A. Schmidt-Ott, *New developments in spark production of nanoparticles,* Advanced Powder Technology **25**, 56 (2014).

[18] M. J. Deen and F. Pascal, *Electrical characterization of semiconductor materials and devices - review,* Journal of Materials Science: Materials in Electronics **17**, 549 (2006).

4

5

THERMOELECTRIC NANOPARTICLES

Economic and technical imperatives - not any preconceived directives - will keep propelling the process of energy transition.

Vaclav Smil

Reducing the thermal conductivity of thermoelectric materials has been a field of intense research to improve the efficiency of thermoelectric devices. One approach is to create a nanostructured thermoelectric material that has a low thermal conductivity due to its high number of grain boundaries or voids, which scatter phonons. Here, we present a new method based on spark ablation nanoparticle generation to create nanostructured thermoelectric materials, demonstrated using Bi_2Te_3. The lowest achieved thermal conductivity was $< 0.1 \, W \, m^{-1} \, K^{-1}$ at room temperature with a mean nanoparticle size of 8 ± 2 nm and a porosity of 44%. This is comparable to the best published nanostructured Bi_2Te_3 films. Oxidation is also shown to be a major issue for nanoporous materials such as the one here, illustrating the importance of immediate, air-tight packaging of such materials after synthesis and deposition.

5.1. INTRODUCTION TO THERMOELECTRIC MATERIALS

T HERMOELECTRIC (TE) materials are materials that produce a potential difference when exposed to a temperature gradient or vice versa. This property can be exploited using a p- and an n-type TE material in a Peltier or a Seebeck module, as drawn in 5.1. Peltier modules apply a potential difference over the TE material to force a heat flow against the temperature gradient, cooling one side and heating the other. Such active cooling can be applied in refrigeration or active cooling of hot surfaces. [2] Seebeck modules use the temperature difference to generate a potential difference, which results in a current. [3–5, 5, 6]
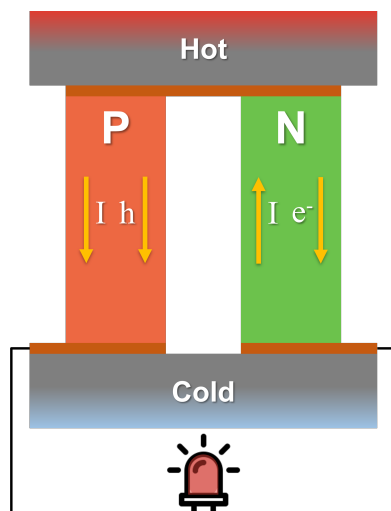
Figure 5.1: Drawing of a Seebeck module, or thermoelectric generator. In this configuration, the temperature difference across the p- and n-type semiconductors create a potential difference that can be connected to a load, here an LED. For a p-type material, the charge gradient is opposite to the n-type with respect to the heat gradient. Placing them electrically in series thus increases the voltage output.

Such modules can recover and convert waste heat generated by hot surfaces or electronic components into electrical energy, potentially boosting the efficiency of LEDs and other microelectronic devices. They could also be used as miniature power generators, called thermoelectric generators (TEGs), harvesting heat from the environment to power small devices such as pacemakers or wearable electronics. [5, 7] Since TE materials are semiconductors and TE devices have no moving parts, they have straightforward integration in IC or MEMS devices. TEGs could replace batteries, especially in applications where regular battery replacement is unwanted and the power requirements are low. Devices can thus be 'made to forget'. Examples are sensors or controllers for internet-of-things or environmental monitoring. [3, 7, 8] On the other end, TE-based solid-state cooling would be highly useful in cryo-TEM or quantum computing electronics. [9]

Unfortunately, due to the low efficiency of TE materials, large-scale application is economically not yet feasible unless costs also drastically decrease. [3, 7, 10–15] The exception is in such niche applications where efficiency is not the major concern (i.e.

space exploration). TEGs have been used for decades by NASA and other space agencies and likely will be for the foreseeable future. [16]

5.1.1. HOW TO IMPROVE THERMOELECTRIC MATERIALS

As mentioned, conversion efficiencies of TE materials are still low, at only a few percent of efficiency. [3, 7, 10–15, 17] To improve energy conversion efficiency, a few properties need to be optimized, which is expressed in a dimensionless figure of merit (FoM):

$$ZT = \frac{S^2 \sigma T}{\kappa_e + \kappa_l} \tag{5.1}$$

Here, S is the Seebeck coefficient in V K^{-1}, σ is the electrical conductivity in S m^{-1}, T the operating temperature in K, and κ_e and κ_l the electrical and lattice contributions of the thermal conductivity in W m^{-1} K^{-1}. $S^2\sigma$ is known as the power factor (PF) and is an expression of the power generation performance of the material. Since all parameters are material dependent (except the operating temperature T), it is possible to optimize the material properties. Evidently, the ideal TE material has high electrical conductivity, a high Seebeck coefficient, and virtually no thermal conductivity. This concept is known as the phonon glass, electron crystal (PGEC) approach and was first described by Slack. [18] Although this ideal material is highly sought after, it has never been actually made. The central problem for TE material optimisation is that S, σ, and κ all depend on material properties such as carrier mobility, carrier concentration, and crystal structure. [6, 13, 19–21] Optimizing for one parameter will change the performance of another and can result in little to no improvement or even reduction of ZT. This trade-off is the cause of the slow progress in TE materials research over the last decades. Even today, decoupling these parameters is the main challenge in designing new TE materials.

When trying to improve ZT, one approach can be to improve the PF. Both the thermopower and the conductivity depend on the charge carrier count, n, and their mobility μ. These are intrinsic properties of the material and adjusting them requires great control over the band structure, crystal lattice, and composition. The primary method of improving these parameters is doping, and indeed many of the best TE materials are heavily doped to maximize the PF. [17]
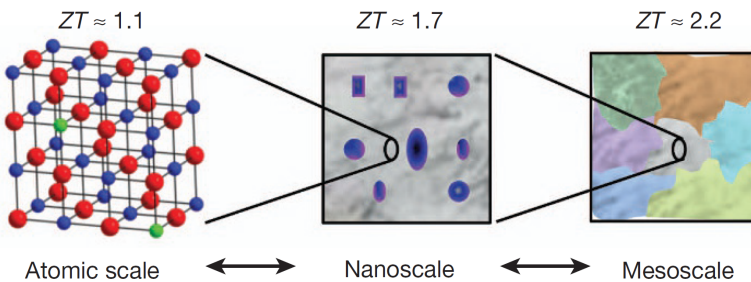

Figure 5.2: Diagram showing the effect of phonon scattering at different size domains. A combination of all domain increases the ZT of SrTe to 2.2. From Biswas et al. 2012. [22]

This brings us to the second way to improve a thermoelectric material, which is to reduce the lattice thermal conductivity, κ_L. Although the thermal conductivity depends also on the electrical thermal conductivity, κ_e, this conductivity is hard to change. κ_e correlates strongly with the electrical conductivity and is hard to tune independently. Consequently, reducing thermal conductivity comes down to minimizing κ_L. Contrary to the other parameters in the FoM, this property can be adjusted without changing the material's intrinsic properties, but by changing its nano- or microstructure.

Heat travels through a crystal lattice as a vibration, called a phonon. These vibrations can be scattered to varying degrees by imperfections in the crystal lattice such as vacancies, dopant atoms, grain boundaries, and voids, depending on the phonon mean free path. [17, 22–26] Figure 5.2 shows several ways phonons are scattered at different size domains. [22] A material that can scatter phonons effectively in all size domains has the lowest κ_L. However, grain boundaries and voids also scatter electrons, making it a difficult trade-off. If done well, the electrical conductivity is minimally affected while reducing the thermal conductivity, creating a PGEC. Creating nanostructured materials is a way to introduce such scattering grain boundaries and many synthesis and methods have been developed to create nanostructured TE materials. [23, 25, 27–34]

SPARK ABLATION FOR NANOSTRUCTURING

Spark ablation can create nanoparticles from any conducting bulk material. We can expect that the nanoporous films this technique can create should be excellent thermal insulators, but we have seen that they are worse conductors than the bulk material (see chapter 4). However, it is worthwhile to investigate to what extent we can reduce the thermal conductivity with this nanostructuring method and see if we can improve the trade-off between electrical and thermal conductivity. The benefit of this technology is that it can take an existing TE material and nanostructure it without any change in composition while simultaneously allowing deposition on many types of surfaces.

This chapter introduces a spark ablation as a method to nanostructure TE materials, demonstrated with undoped Bi_2Te_3. A first attempt to synthesize a TE film using spark ablation is presented here, without any optimization of the material, to demonstrate the feasibility of this technology. The performance is discussed and recommendations on how to improve the process and material are made.

5.2. EXPERIMENTAL

5.2.1. NANOPARTICLE GENERATION AND DEPOSITION

The spark ablation generator was used with a pair of 99.999% Bi_2Te_3 electrodes supplied by VSPARTICLE B.V. The ablation settings were 1 kV and 3 mA with 1.5 l min^{-1} of Ar with 2% H_2 as carrier gas. The addition of hydrogen to the carrier gas is known to suppress oxidation of the metallic nanoparticles, which under normal circumstances oxidize rapidly due to their clean and unprotected surface. [35, 36] The impactor operated at 0.5 mbar with a nozzle throughput of 0.33 l min^{-1}. Printing settings were unless specified differently, 1 mm per minute with a 1 mm nozzle distance.

5.2.2. STRUCTURE CHARACTERISATION

A Bruker D8 Discover diffractometer was used for XRD measurements. Samples were prepared on a Si(100) die. An XL30 SFEG SEM from Thermo Fisher Scientific was used for SEM at 10 kV. TEM images for the size distribution were made with a JEOL 1400, operated at a 120 kV acceleration voltage. For HR-TEM, a FEI cubed Cs corrected Titan TEM was used, operated at 300 kV. The nanoparticles were deposited with a writing speed of 200 mm min^{-1} to create a film of less than a full monolayer in thickness on Si grids with 50 nm AlO$_x$ membranes made in-house. Regular grids of carbon membrane on a Cu mesh would be destroyed by the force of the deposition jet and could not be used. AlO$_x$ membranes are much stronger, but their transparency is not as uniform as a carbon film due to large crystal grains in the AlO$_x$ layers. This made particle size analysis difficult to automate, so particles were measured manually in ImageJ. The porosity was determined using the method described in chapter 3. [37]

5.2.3. THERMOELECTRIC CHARACTERISATION

After the initial synthesis and material analysis, its performance as a TE material had to be tested. First, the Seebeck coefficient was measured using a home-built setup shown in Figure 5.3. The film was printed on a 20 by 5 mm strip of silicon wafer with 100 nm thermally grown SiO$_2$ and four 10/100 nm Cr/Au electrodes for electrical contact.
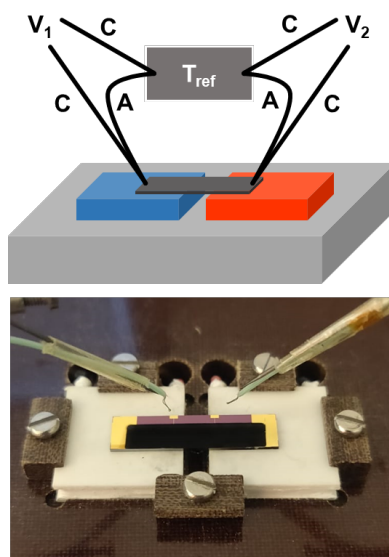
Figure 5.3: Top: schematic drawing of the Seebeck effect measurement setup. The device is placed on two Peltier elements to create a temperature gradient over the device. The voltage and temperature are read simultaneously using type K thermocouples at both ends of the device and the setup contribution is subtracted from the acquired voltage. The thermocouples, made of chromel (C) and alumel (A), are used with a liquid nitrogen bath as the reference temperature. Bottom: picture of a device placed on the Peltier elements with the thermocouples (not in contact). The black strip is the Bi$_2$Te$_3$ film deposited on Au contacts.

Electrical conductivity was measured in situ using 4-point-probe chips wirebonded

to a DIL package, which was mounted on a PCB inside the printing chamber. The PCB was connected to a Keithley 2450 sourcemeter and set at a constant value of 10 mA during readout. During deposition, the nozzle moved over the four electrodes, while the sourcemeter read the resistance, creating a conducting line. For the long-term degradation study, measurements were performed on a Cascade Microtech microprobestation at ambient conditions.

The thermal conductivity of the films was investigated using time-domain thermoreflectance (TDTR) with the Netzsch PicoTR instrument. The measurement parameters of the pump–probe technique can be found in. [2] The samples were measured by using the principle of the bidirectional heat flow approach. [38, 39] For doing so, the films of interest with a thickness of >15 μm were deposited on 1 mm-thick quartz with a 100 nm Al layer on top. Both lasers were focused at the interface between Al and glass, as they pass through the glass substrate according to their wavelengths of 775 nm (probe) and 1550 nm (pump). The Al layer acted here as a reflection layer for the probing and an absorption layer to guarantee uniform heating. The properties of the Bi_2Te_3 were deduced from the cooling curve. Therefore, an analytical model of the cooling was set up that included two heat flows. The first was the interface conductance between Al and glass, as well as through the glass substrate. The second one was the heat flow through the Al layer, the interface conductance between Al and through the Bi_2Te_3, and the Bi_2Te_3 layer. For the analysis of the film, its density of 3.4 kg m^{-3} and its specific heat of 127 J mol^{-1} K^{-1} served as input parameters for the evaluation. Furthermore, the thermal conductivity values of the Al layer, the glass substrate, and the interface conductance between Al and glass were obtained by performing TDTR measurements on the sample without the Bi_2Te_3 films. Because of logistical difficulty in shipping the samples for TDTR measurement, it was not possible to measure the thermal conductivity earlier than presented.

5.3. Results and discussion
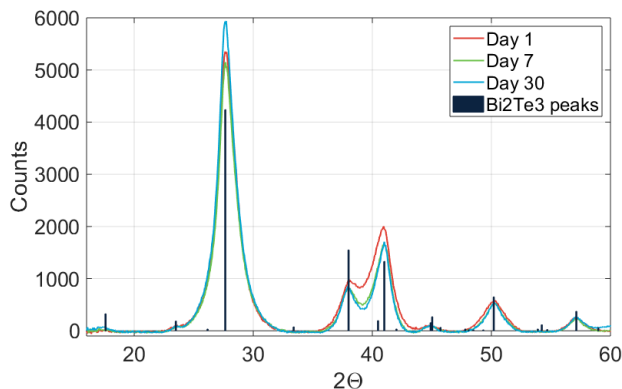
5.3.1. Nanostructure and composition

Figure 5.4: XRD spectrum showing a Bi_2Te_3 sample as freshly deposited (red), after one week (green), and after a month (blue).

Figure 5.4 shows that the deposited material was pure polycrystalline Bi_2Te_3; no other phases were detectable. The grain size could be extracted from an XRD spectrum with the Scherrer equation, which was applied to the highest peak. The full calculation and results are enclosed in appendix C. The fresh sample had an approximate grain size of 5.1 nm, while the week-old and month-old samples were slightly larger, at 5.3 and 5.5 nm. An increase that small can be attributed to measurement error, such as a slightly different measurement location or orientation of the sample. It can therefore be concluded there was no significant change in the Bi_2Te_3 grain size over time. Although it is not accurate to attribute all peak widening to grain size and the calculation assumes perfectly spherical particles, we can confidently say that the grain size was approximately 5 to 6 nm and that there were no large particles in the samples. [40] The existence of a crystalline Bi_2Te_3 phase even after 1 month shows that the samples did not degrade significantly within this timespan.

TEM images, such as the ones in Figure 5.5, showed agglomerated nanoparticles with extensive neck formation or even fusion of particles. The images indicate that the surface of the nanoparticles consisted of highly mobile atoms that fused easily. The size distribution in figure 5.6 shows a log-normal distribution as typically found in spark ablation generation. [40, 41] The mean particle size of 8 ± 2 nm was slightly larger than the mean found by XRD. Two effects can contribute to this: a non-crystalline Bi_2Te_3 outer layer or an amorphous oxide shell. In both cases, XRD would only work on the crystalline core, ignoring the outer layer.

A side view of a printed film, as shown in Figure 5.7a, shows a porous but continuous film similar to compacted powders. The film is 2.1 μm thick and has a high surface roughness, visible in Figure 5.7b.
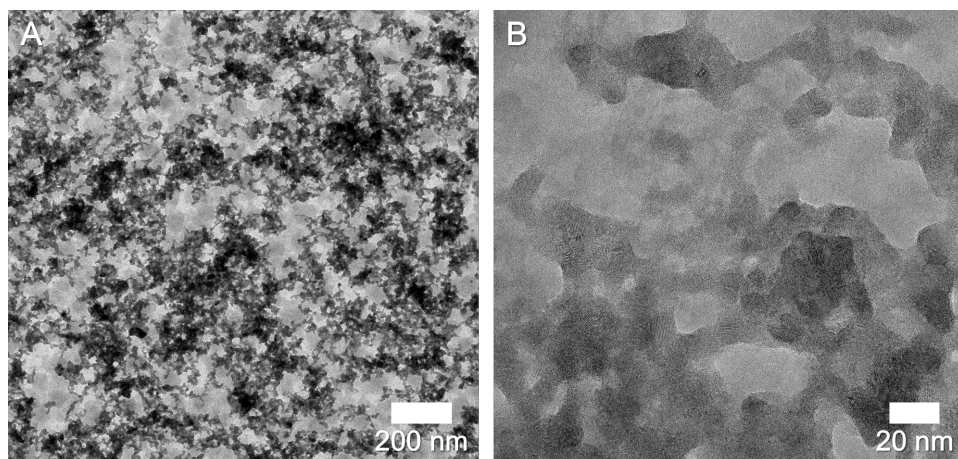
Figure 5.5: A) TEM images of Bi_2Te_3 nanoparticles. B) HR-TEM image. We can observe extensive agglomeration and neck formation between particles in an agglomerate. The background is blurry because the membranes have non-uniform transparency due to processing imperfections during production and crystallinity of the AlO_x substrate. Printing speed was 200 mm min.$^{-1}$. All other settings are as mentioned before.
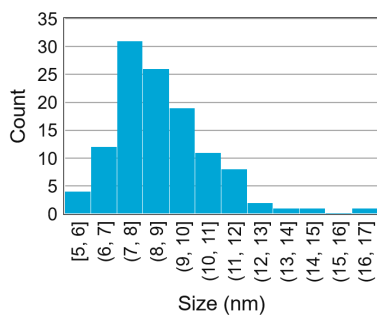
Figure 5.6: Size distribution of the diameter of 116 nanoparticles measured by hand on 4 TEM images. Automated measurements were not possible due to the blurry background. The mean particle size is 8 ± 2 nm.
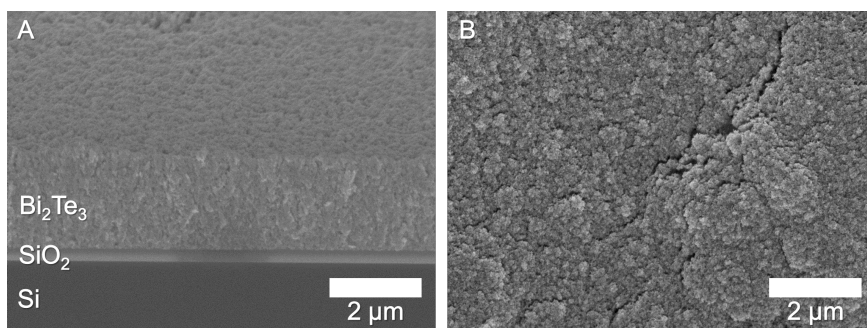
Figure 5.7: A) Side view of a cleaved deposit with the SiO_2 layer visible between the Si and Bi_2Te_3. The printed line is 2.1 μm thick. B) Top view of the same sample showing a rough surface.
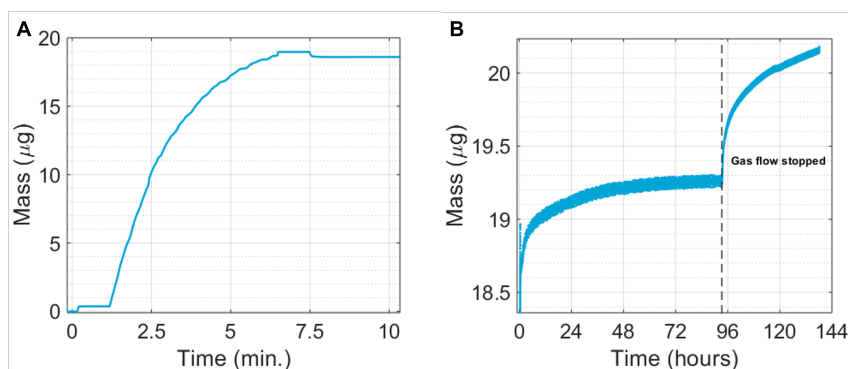
Figure 5.8: A) Mass change over time during deposition as recorded by a QCM. The first step results from the force exerted by the nozzle on the QCM. The decaying mass deposition rate is caused by the printing pattern and non-uniform response of the QCM. Once printing is finished, a step down happens when the nozzle leaves the printing area. The final deposited mass is 18.60 μg. B) Mass change of the same sample after deposition. Initially, the Ar/H$_2$ gas flow was still on with the nozzle next to the QCM. Gas flow was closed off to see the effect of the deposition chamber in an "idle" state.

The mass deposition process can be seen in Figure 5.8A and shows a similar characteristic apparent mass deposition rate as described in Van Ginkel et al. [37] This was due to the decreasing mass sensitivity near the edges of the electrode, resulting in a lower response of the QCM for the same deposition rate. Therefore, the beginning and end points were the only relevant points to determine the total mass change during deposition accurately. As seen in Figure 5.8B, after reaching a mass of 18.60 μg, the deposit mass rapidly increases and stabilizes under the protective Ar/H$_2$ atmosphere at around 19.25 μg. When the gas flow is stopped, the chamber is pumped down, and leaked-in oxygen can react with the deposit, rapidly increasing the reaction rate. However, since the mass increases immediately after deposition, we must conclude that even the 99.999% pure Ar/H$_2$ gas contains enough impurities to begin oxidation and thus, oxidation must have started during deposition.

The experiment was stopped at 20.45 μg, a total mass increase of 9.9%. Total oxidation of the sample, consisting of pure Bi$_2$O$_3$ and TeO$_2$, would increase the mass by 18%: from 800.74 u to 944.76 u. [42, 43] Bando et al. (2000) also found that even after long term exposure to air at room temperature, the oxide layer does not exceed 2 nm even after 5700 hours. [43, 44] In contrast to their experiment on a solid monocrystalline Bi$_2$Te$_3$, the nanoparticles here were in contact with oxygen residuals in all directions. Yet, the oxidation reaction appeared to still be slow. Oxidation was not finished, but all mass increase could not solely be attributed to oxidation, particularly after closing the clean gas flow over the sample. Water or organic compounds in the air could have adsorbed on the surface, which, due to the high surface area of the nanoporous film, could have been in significant quantities. This was, however, not visible on the SEM or TEM images, since they formed a thin film and were volatile, desorbing in high vacuum systems and under electron beam irradiation.

Using three QCMs, a mean deposition rate of $2.93 \times 10^{-3} \pm 4.81 \times 10^{-4}$ mg min^{-1} was

measured. Combining this result with a one-minute deposition volume of 8.89×10^{-7} cm^3 gave a mean density of 3.40 ± 0.33 g cm^{-3}, or a 0.44 ± 0.04 porosity. This is significantly lower than previously found for Au [37] due to the lower malleability of Bi$_2$Te$_3$, leading to less restructuring upon impact during deposition. It was also previously found that the density of Au films is insensitive to variation in the synthesis parameters, as tested by van Ginkel et al., giving a constant value for all syntheses within the operating conditions of the setup. [37] It is therefore assumed that all samples here had the same density (and porosity) too because the synthesis conditions were nearly identical.

5.3.2. THERMOELECTRIC PERFORMANCE

The key metric for a TE material is its figure of merit ZT (equation 5.1), which can not be measured directly but is calculated from several measurements. A negative Seebeck coefficient of -88.3 ± 1.2 μV K^{-1} was obtained (see fig. 5.9, indicating that we had n-type Bi$_2$Te$_3$. Bulk Bi$_2$Te$_3$ grown from a melt is, by its nature, usually p-type, while n-type Bi$_2$Te$_3$ is made by either doping with, for example, I or Br, or by having an excess of Te. [15] Most nanostructured Bi$_2$Te$_3$ is also n-type, possibly due to vacancies or surface states that act as dopants. [29, 34, 45, 46] Interestingly, ageing the sample in the air seemed to improve the Seebeck coefficient, which stabilised at -105.1 ± 1.6 μV K^{-1}. This value is lower than most reported values for Bi$_2$Te$_3$, at -100 to -250 μV K^{-1}, but is not unusual for low conductivity samples. [11, 29, 47–49] It must be noted that the Bi$_2$Te$_3$ used here was undoped, and no attempts were made to optimise the material's Seebeck coefficient.
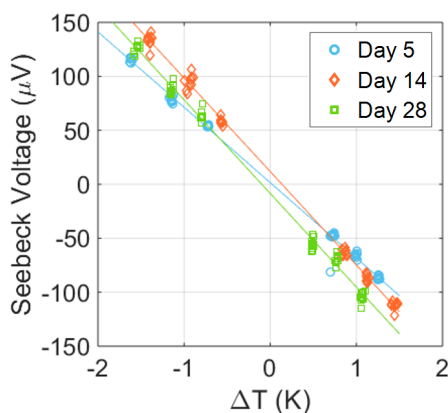
Figure 5.9: Seebeck voltage determined using the setup in Figure 5.3 on a sample measured at several points after synthesis. Repeated measurements were taken at room temperature with a ΔT created using Peltier elements. The slope of a least squares fit gave the Seebeck voltage. The first measurement had $S = -88.3 \pm 1.2$ μV K^{-1}, which increased to $S = -105.1 \pm 1.2$ μV K^{-1} and did not increase further after two more weeks, reaching $S = -105.2 \pm 1.6$ μV K^{-1}.

The electric conductivity was measured during deposition in vacuum on packaged and wirebonded samples. The four electrode devices could only create a measurement when the nozzle had deposited on all four electrodes, after which an initial resistance was measured and a sharp drop in resistance occurred while the nozzle moved over the
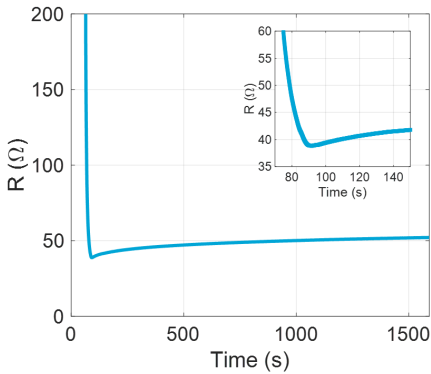
Figure 5.10: Resistance of a single wirebonded device during deposition. Until deposition, an open circuit is measured (not shown), after which a sharp decrease in the resistance is seen until the deposition area has passed entirely over the four electrodes and deposition ends, after which we see an increase due to oxidation and restructuring of the film. Inset: close-up at the deposition time. The lowest measured value was 38.82 Ω. The film was kept under deposition conditions for the duration of the measurement.
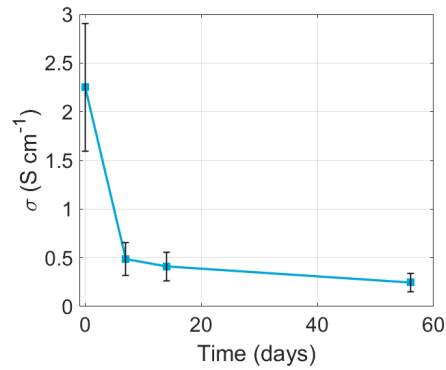
Figure 5.11: Decay of the mean conductivity of six deposited lines with 61 measurement points each. Measurements were done within hours of deposition, so some degree of oxidation must be assumed at day zero. After a fast decrease of nearly a factor 5 in the first week, conductivity decay slows down.

last electrode. We can see this exact behaviour in Figure 5.10, with a resistance minimum of 38.82Ω. After deposition, there was an immediate increase in resistance that slowed down gradually, but did not come to a complete halt. After 25 min, the resistance already increased by 34% and measurements using a four-point-probe system, as seen in Figure 5.11, showed that the degradation in the first week was fast, but levelled off after this. However, the conductivity did reduce further and did not seem to have reached the minimum, even after 56 days. These results show that it is critical that a deposit is protected immediately after deposition, or the electrical performance will deteriorate rapidly.

As introduced earlier, the primary aim of the experiments presented here was to reduce the thermal conductivity of the Bi_2Te_3 by nanostructuring and improve the figure of merit. Figure 5.12 shows the thermal conductivity of three samples (S1 to S3). S1 and S2 had identical settings (1 kV, 3 mA, $1.5\,l\,min^{-1}$ Ar/5% H_2), while S3 was made with a spark at 0.8 kV. All samples showed low thermal conductivity $<0.4\,W\,m^{-1}\,K^{-1}$, with the lowest value well below $0.2\,W\,m^{-1}\,K^{-1}$, comparable to the lowest values reported in the literature, and a nearly tenfold reduction compared to the bulk thermal conductivity. [11] This reduction can be attributed to the nanostructure of the film, introducing grains in the $<10\,nm$ range where phonons are scattered at the grain boundaries, as demonstrated before for Bi_2Te_3. [24, 25, 45, 47, 50–52] The porosity introduces further boundary scattering of the phonons in addition to the grain boundaries. [24, 45] The 0.8 kV sample was expected have a slightly smaller mean particle size, which would have contributed to a lower κ. However, the value spread between the three samples made it impossible to attribute the lower value to a smaller particle size alone.
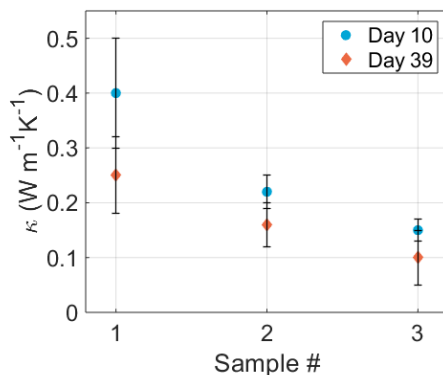
Figure 5.12: Thermal conductivity of three samples measured by LFA, measured 10 and 49 days after deposition. Each datapoint consists of two measurements at different positions on the film, using a density of 56% that of bulk Bi_2Te_3, or 3.51 g cm^{-3}. A significant reduction of thermal conductivity can be observed for two out of three samples after ageing in the air.

One month later, a further reduction in κ could be observed. This was likely due to degradation of the film by oxidation. An oxide shell around the nanoparticles will thermally insulate the nanoparticles. The samples were all prepared in the same batch and had an identical history, so the different κ values were not readily explainable. Thickness was accounted for in the analysis, and measurements were performed on three locations per sample to account for local differences. Considering that the porosity should be the same (see chapter 3), the differences between them must have been due to other minor process deviations that were not readily identifiable. The ageing also decreased the differences between samples, suggesting that the initial state of each sample may not have been equal.

The power factor (PF) and zT of the material were not determinable at any given point in time due to the different timing of each measurement. However, we could calculate approximate theoretical values at day 7 after synthesis by using the nearest datapoint for each variable. This gave a PF of 3.7×10^{-4} W m^{-1} K^{-1} and a zT of 4.2×10^{-4}. Compared to other nanostructured n-type Bi_2Te_3, this is low, but the difference is predominantly caused by the greater than thousandfold lower electrical conductivity [29, 34, 45]. The zT increased slightly at day 30 due to an improvement in S and κ, even though this was largely negated by a further degradation of σ.

5.4. DISCUSSION

Nanostructuring has reduced the thermal conductivity of Bi_2Te_3 by one order of magnitude. Unfortunately, the electrical conductivity has been reduced by over two orders of magnitude and decreases further over time. This degradation can partly be ascribed to oxidation, which forms an insulating shell around the nanoparticles. The QCM measurements indicate that this can happen directly after synthesis, so for the optimal synthesis process, more measures should be taken to prevent oxidation. Examples are a

higher concentration of reducing gas (e.g. H_2) [35], the addition of moisture and oxygen filters, or longer runtime before the deposition to purge the system. [53] Furthermore, it is crucial to protect these reactive nanoparticles after production. The results in this work suggest that a protective atmosphere can protect the deposits for the first few minutes, but in the end, this only slows down the degradation. This can be expected for any nanoporous material, as air can penetrate deeply into the film and oxidize it throughout. Immediate further processing or packaging is thus required for nanoporous films to maintain their initial performance.

Considering these experiments were not aimed at producing the optimal material but at demonstrating the production method by using a common material, the Bi_2Te_3 performance can be improved in several ways. Firstly, the Bi_2Te_3 used in the experiments here was undoped, while it is known that doping or even alloying significantly improves the performance of TE materials. [11, 49] Secondly, the porosity helped reduce the thermal conductivity, but was also detrimental to the electrical conductivity. Changing the deposition conditions or particle size to change the porosity is possible, but the film will remain highly porous. It is common to compress and sinter nanopowders, using spark plasma sintering (SPS), into pellets, to increase the electrical conductivity while maintaining the nanosized grains. [24, 54, 55] SPS requires larger quantities to enable pelletising, which this printing method cannot yet produce, but future versions of this equipment could. Compression by other means can be an alternative. By sandwiching the material between the two contacts of a thermopile, it can be simultaneously protected, packaged, and contacted. A roll-to-roll or flip-chip process could be developed with spark ablation and impaction printing to achieve this.

Lastly, this method can produce other TE materials. For example, producing oxides for high-temperature applications makes oxidation problems irrelevant. ZnO, a thermoelectric oxide, has been successfully deposited this way, and the first experiments have been conducted to assess its performance. Alternatively, but not performed here, one could use this process to find new compositions that do not exist as bulk alloys. [56] A combination of two or more spark generators in series or parallel can even create mixtures of nanoparticles, introducing inclusions and complex materials.

5.5. CONCLUSIONS AND RECOMMENDATIONS

In conclusion, the synthesis of TE materials using spark ablation is possible, and the fabrication of nanostructured TE devices was demonstrated using impaction printing. The one-step approach and direct writing capability make it a simple, clean, and versatile method for producing TE materials. The technology was demonstrated using undoped Bi_2Te_3 because it is the most common TE material. It exhibited n-type behaviour. The lowest found κ was 0.2 W m^{-1} K^{-1} at room temperature, comparable to state-of-the-art nanostructured Bi_2Te_3, but this came at the cost of the electrical conductivity. The material showed degradation over time, starting immediately after deposition: 37% reduction in conductivity was already observed within the first 25 minutes. This can be attributed to mild oxidation and adsorption of contaminants on the nanoparticle surface. To retain its performance, further protection of the film or immediate, air-tight packaging of the device is required. Although the method presented here can synthesise

and deposit a wide range of TE materials without developing new synthesis processes, the process requires further optimisation. Its performance was lower than comparable nanostructured films, predominantly due to the low electrical conductivity. Improved material composition and synthesis parameters, perhaps combined with compression or annealing to reduce porosity, will improve the TE performance further.

REFERENCES

[1] H. J. van Ginkel, L. Mitterhuber, M. W. van de Putte, M. Huijben, S. Vollebregt, and G. Zhang, *Nanostructured thermoelectric films synthesised by spark ablation and their oxidation behaviour,* Nanomaterials **13,** 1778 (2023).

[2] W. Lee and J. Lee, *Development of a compact thermoelectric generator consisting of printed circuit heat exchangers,* Energy Conversion and Management **171,** 1302 (2018).

[3] J. He and T. M. Tritt, *Advances in thermoelectric materials research: Looking back and moving forward,* Science **357** (2017), 10.1126/science.aak9997.

[4] A. J. Minnich, M. S. Dresselhaus, Z. F. Ren, and G. Chen, *Bulk nanostructured thermoelectric materials: current research and future prospects,* Energy Environ. Sci. **2,** 466 (2009).

[5] L. Yang, Z.-G. Chen, M. S. Dargusch, and J. Zou, *High performance thermoelectric materials: Progress and their applications, Advanced Energy Materials,* Adv. Energy Mater. **8,** 1701797 (2018).

[6] D. Rowe, ed., *Thermoelectrics Handbook* (CRC Press, 2018).

[7] J. Yan, X. Liao, D. Yan, and Y. Chen, *Review of micro thermoelectric generator,* Journal of Microelectromechanical Systems **27,** 1 (2018).

[8] H. Bottner, J. Nurnus, A. Schubert, and F. Volkert, *New high density micro structured thermogenerators for stand alone sensor systems,* in *2007 26th International Conference on Thermoelectrics* (2007) pp. 306–309.

[9] S. Waldrop and D. Morelli, *Low-temperature thermoelectric properties of PtSb2 for cryogenic peltier cooling applications,* Journal of Electronic Materials **44,** 1562 (2015).

[10] Y. Yin, B. Tudu, and A. Tiwari, *Recent advances in oxide thermoelectric materials and modules,* Vacuum **146,** 356 (2017).

[11] I. T. Witting, T. C. Chasapis, F. Ricci, M. Peters, N. A. Heinz, G. Hautier, and G. J. Snyder, *The thermoelectric properties of bismuth telluride,* Advanced Electronic Materials **5,** 1800904 (2019).

[12] Y. Feng, X. Jiang, E. Ghafari, B. Kucukgok, C. Zhang, I. Ferguson, and N. Lu, *Metal oxides for thermoelectric power generation and beyond,* Advanced Composites and Hybrid Materials **1,** 114 (2018).

[13] W. Liu, Q. Jie, H. S. Kim, and Z. Ren, *Current progress and future challenges in thermoelectric power generation: From materials to devices,* Acta Materialia **87**, 357 (2015).

[14] Y. Ouyang, Z. Zhang, D. Li, J. Chen, and G. Zhang, *Emerging theory, materials, and screening methods: New opportunities for promoting thermoelectric performance,* Annalen Der Physik **0**, 1800437 (2019).

[15] T. M. Tritt, *Thermoelectric phenomena, materials, and applications,* Annual Review of Materials Research **41**, 433 (2011).

[16] C. S. R. Matthes, D. F. Woerner, T. J. Hendricks, J. Fleurial, K. I. Oxnevad, C. D. Barklay, and J. F. Zakrajsek, *Next-generation radioisotope thermoelectric generator study,* in *2018 IEEE Aerospace Conference* (IEEE, 2018) pp. 1–9.

[17] Q. Yan and M. G. Kanatzidis, *High-performance thermoelectrics and challenges for practical devices,* Nature Materials **21**, 503 (2021).

[18] G. A. Slack, *CRC Handbook of Thermoelectrics,* edited by D. Rowe (CRC Press, 1995).

[19] W. G. Zeier, A. Zevalkink, Z. M. Gibbs, G. Hautier, M. G. Kanatzidis, and G. J. Snyder, *Thinking like a chemist: Intuition in thermoelectric materials,* Angewandte Chemie International Edition **55**, 6826 (2016).

[20] E. Witkoske, X. Wang, J. Maassen, and M. Lundstrom, *Universal behavior of the thermoelectric figure of merit, zT, vs. quality factor,* Materials Today Physics **8**, 43 (2019).

[21] T. Zhu, Y. Liu, C. Fu, J. P. Heremans, J. G. Snyder, and X. Zhao, *Compromise and synergy in high-efficiency thermoelectric materials,* Advanced Materials **29**, 1605884 (2017).

[22] K. Biswas, J. He, I. D. Blum, C.-I. Wu, T. P. Hogan, D. N. Seidman, V. P. Dravid, and M. G. Kanatzidis, *High-performance bulk thermoelectrics with all-scale hierarchical architectures,* Nature **489**, 414 (2012).

[23] M. G. Kanatzidis, *Nanostructured thermoelectrics: The new paradigm?* Chem. Mater. **22**, 648 (2010).

[24] L. Yang, Z.-G. Chen, M. Hong, G. Han, and J. Zou, *Enhanced thermoelectric performance of nanostructured Bi2Te3 through significant phonon scattering,* ACS Applied Materials and Interfaces **7**, 23694 (2015).

[25] C. J. Vineis, A. Shakouri, A. Majumdar, and M. G. Kanatzidis, *Nanostructured thermoelectrics: Big efficiency gains from small features,* Advanced Materials **22**, 3970 (2010).

[26] J. R. Sootsman, D. Y. Chung, and M. G. Kanatzidis, *New and old concepts in thermoelectric materials, Angewandte Chemie International Edition,* Angewandte Chemie International Edition **48**, 8616 (2009).

5

[27] T. G. Novak, K. Kim, and S. Jeon, *2D and 3D nanostructuring strategies for thermoelectric materials,* Nanoscale **11**, 19684 (2019).

[28] S. D. N. Luu, T. A. Duong, and T. B. Phan, *Effect of dopants and nanostructuring on the thermoelectric properties of ZnO materials,* Advances in Natural Sciences: Nanoscience and Nanotechnology **10**, 023001 (2019).

[29] D. Bao, J. Chen, Y. Yu, W. Liu, L. Huang, G. Han, J. Tang, D. Zhou, L. Yang, and Z.-G. Chen, *Texture-dependent thermoelectric properties of nano-structured Bi2Te3,* Chemical Engineering Journal **388**, 124295 (2020).

[30] X. Song, K. Valset, J. Graff, A. Thøgersen, A. Gunnæs, S. Luxsacumar, O. Løvvik, G. Snyder, and T. Finstad, *Nanostructuring of undoped ZnSb by cryo-milling,* Journal of Electronic Materials **44**, 2578 (2015).

[31] P. Jood, R. J. Mehta, Y. Zhang, G. Peleckis, X. Wang, R. W. Siegel, T. Borca-Tasciuc, S. X. Dou, and G. Ramanath, *Al-doped zinc oxide nanocomposites with enhanced thermoelectric properties,* Nano Letters **11**, 4337 (2011).

[32] P. K. Nguyen, K. H. Lee, J. Moon, S. I. Kim, K. A. Ahn, L. H. Chen, S. M. Lee, R. K. Chen, S. Jin, and A. E. Berkowitz, *Spark erosion: a high production rate method for producing Bi0.5Sb1.5Te3 nanoparticles with enhanced thermoelectric performance,* Nanotechnology **23**, 415604 (2012).

[33] K. Park, J. S. Son, S. I. Woo, K. Shin, M.-W. Oh, S.-D. Park, and T. Hyeon, *Colloidal synthesis and thermoelectric properties of La-doped SrTiO3 nanoparticles,* J. Mater. Chem. A **2**, 4217 (2014).

[34] J. Qiao, Y. Zhao, Q. Jin, J. Tan, S. Kang, J. Qiu, and K. Tai, *Tailoring nanoporous structures in Bi2Te3 thin films for improved thermoelectric performance,* ACS Applied Materials and Interfaces **11**, 38075 (2019).

[35] R. T. Hallberg, L. Ludvigsson, C. Preger, B. O. Meuller, K. A. Dick, and M. E. Messing, *Hydrogen-assisted spark discharge generated metal nanoparticles to prevent oxide formation,* Aerosol Science and Technology **52**, 347 (2017).

[36] M. Seipenbusch, A. Weber, A. Schiel, and G. Kasper, *Influence of the gas atmosphere on restructuring and sintering kinetics of nickel and platinum aerosol nanoparticle agglomerates,* Journal of Aerosol Science **34**, 1699 (2003).

[37] H. J. van Ginkel, S. Vollebregt, A. Schmidt-Ott, and G. Q. Zhang, *Mass and density determination of porous nanoparticle films using a quartz crystal microbalance,* Nanotechnology **33**, 485704 (2022).

[38] D. G. Cahill, *Analysis of heat flow in layered structures for time-domain thermoreflectance,* Review of Scientific Instruments **75**, 5119 (2004).

[39] A. Schmidt, M. Chiesa, X. Chen, and G. Chen, *An optical pump-probe technique for measuring the thermal conductivity of liquids,* Review of Scientific Instruments **79**, 064902 (2008).

5

[40] N. S. Tabrizi, M. Ullmann, V. A. Vons, U. Lafont, and A. Schmidt-Ott, *Generation of nanoparticles by spark discharge*, Journal of Nanoparticle Research **11**, 315 (2008).

[41] A. Schmidt-Ott, *Spark Ablation: Building Blocks for Nanotechnology*, 1st ed., edited by A. Schmidt-Ott (Jenny Stanford Publishing, 2020).

[42] D. Music, K. Chang, P. Schmidt, F. N. Braun, M. Heller, S. Hermsen, P. J. Pöllmann, T. Schulzendorff, and C. Wagner, *On atomic mechanisms governing the oxidation of Bi2Te3*, Journal of Physics: Condensed Matter **29**, 485705 (2017).

[43] H. Bando, K. Koizumi, Y. Oikawa, K. Daikohara, V. A. Kulbachinskii, and H. Ozaki, *The time-dependent process of oxidation of the surface of Bi2Te3 studied by x-ray photoelectron spectroscopy*, Journal of Physics: Condensed Matter **12**, 5607 (2000).

[44] L. V. Yashina, J. Sanchez-Barriga, M. R. Scholz, A. A. Volykhov, A. P. Sirotina, S. N. Vera, M. E. Tamm, A. Varykhalov, D. Marchenko, G. Springholz, G. Bauer, A. Knop-Gericke, and O. Rader, *Negligible surface reactivity of topological insulators Bi2Se3 and Bi2Te3 towards oxygen and water*, ACS Nano **7**, 5181 (2013).

[45] Y. Wang, W.-D. Liu, H. Gao, L.-J. Wang, M. Li, X.-L. Shi, M. Hong, H. Wang, J. Zou, and Z.-G. Chen, *High porosity in nanostructured n-type Bi2Te3 obtaining ultralow lattice thermal conductivity*, ACS Applied Materials and Interfaces **11**, 31237 (2019).

[46] M. Goto, M. Sasaki, Y. Xu, T. Zhan, Y. Isoda, and Y. Shinohara, *Control of p-type and n-type thermoelectric properties of bismuth telluride thin films by combinatorial sputter coating technology*, Applied Surface Science **407**, 405 (2017).

[47] B. Hamawandi, H. Batili, M. Paul, S. Ballikaya, N. I. Kilic, R. Szukiewicz, M. Kuchowicz, M. Johnsson, and M. S. Toprak, *Minute-made, high-efficiency nanostructured Bi2Te3 via high-throughput green solution chemical synthesis*, Nanomaterials **11**, 2053 (2021).

[48] R. Werner, J. S. Matejka, D. Schönauer-Kamin, and R. Moos, *From thermoelectric powder directly to thermoelectric generators: Flexible Bi2Te3 films on polymer sheets prepared by the powder aerosol deposition method at room temperature*, Energy Technology **10**, 2101091 (2022).

[49] M.-K. Han, Y. Jin, D.-H. Lee, and S.-J. Kim, *Thermoelectric properties of Bi2Te3: CuI and the effect of its doping with Pb atoms*, Materials **10**, 1235 (2017).

[50] Y. Wang, Y. Sui, J. Cheng, X. Wang, and W. Su, *Comparison of the high temperature thermoelectric properties for Ag-doped and Ag-added Ca3Co4O9*, Journal of Alloys and Compounds **477**, 817 (2009).

[51] B. Poudel, Q. Hao, Y. Ma, Y. Lan, A. Minnich, B. Yu, X. Yan, D. Wang, A. Muto, D. Vashaee, X. Chen, J. Liu, M. S. Dresselhaus, G. Chen, and Z. Ren, *High-thermoelectric performance of nanostructured bismuth antimony telluride bulk alloys*, Science **320**, 634 (2008).

5

[52] K. K. Choudhary, U. Sharma, P. D. Lodhi, and N. Kaurav, *Size effect on thermoelectric properties of Bi2Te3 nanoparticles,* in *AIP Conference Proceedings* (2018).

[53] V. Vons, A. Anastasopol, W. Legerstee, F. Mulder, S. Eijt, and A. Schmidt-Ott, *Low-temperature hydrogen desorption and the structural properties of spark discharge generated Mg nanoparticles,* Acta Materialia **59**, 3070 (2011).

[54] Z.-H. Ge, B.-P. Zhang, Y.-X. Chen, Z.-X. Yu, Y. Liu, and J.-F. Li, *Synthesis and transport property of Cu1.8S as a promising thermoelectric compound,* Chem. Commun. **47**, 12697 (2011).

[55] M. Y. Tafti, S. Ballikaya, A. M. Khachatourian, M. Noroozi, M. Saleemi, L. Han, N. V. Nong, T. Bailey, C. Uher, and M. S. Toprak, *Promising bulk nanostructured Cu2Se thermoelectrics via high throughput and rapid chemical synthesis,* RSC Adv. **6**, 111457 (2016).

[56] J. Feng, D. Chen, P. V. Pikhitsa, Y. ho Jung, J. Yang, and M. Choi, *Unconventional alloys confined in nanoparticles: Building blocks for new matter,* Matter **3**, 1646 (2020).

5

6

ZNO NANOPARTICLE BASED UV SENSORS

Do. Or do not. There is no try.

Yoda - Star Wars: Episode V — The Empire Strikes Back

Sensing ultraviolet (UV) light is important to protect people from exposure to this harmful radiation. Manufacturing of such devices has been possible for a while, but simple, printable, and biodegradable devices are still far off. In this chapter, spark ablation generated nanoparticles are used to detect UV-C light. A photoresistor was fabricated using wide-bandgap ZnO nanoparticles. Due to the wide bandgap of ZnO, the device is blind to visible light and exclusively responds to UV light. They show a hundredfold decrease in resistance when exposed to UV light compared to darkness.

6.1. INTRODUCTION

ULTRAVIOLET (UV) light is light with a wavelength between 10 to 400 nm. This high-energy light is invisible to the naked eye and harmful to the skin. UV-A (315 to 400 nm) and, in particular, UV-B (280 to 315 nm) are causes of sunburn and skin cancer and should be protected against by using sunscreen. At even lower wavelengths, the UV-C range (100-280 nm), UV light is mutagenic, and exposure to this light should be avoided entirely. Fortunately, the ozone layer blocks most harmful UV radiation emitted by the sun, or the earth would be sterilized. However, the sterilizing property of UV-C can be used to disinfect surfaces, water, or air. [2, 3] This application has been of particular interest since the outbreak of the COVID-19 pandemic in 2020, and many publications have since been made on the effectiveness of UV-lamps in sterilizing our environment. Products are now on the market for businesses and consumers to disinfect indoor air and surfaces. [4–6]
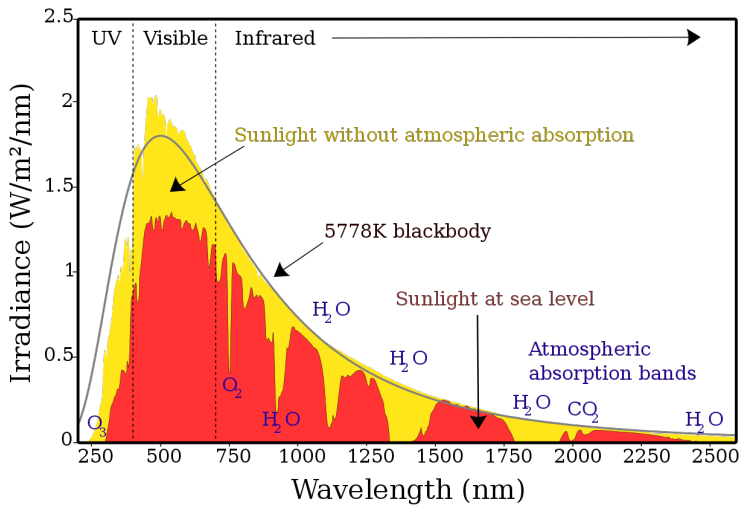
Figure 6.1: The solar spectrum showing the regions of ultraviolet, visible and infrared light and the absorption bands of certain molecules in the atmosphere. [7]

It is important to have the correct dosage of this light to passivate or kill any microbes or viruses effectively. Too low irradiance will not sterilize enough, while a too high dosage might degrade the surfaces exposed to the light (and consume too much power). Additionally, because humans can not see UV light, we can not detect if a UV lamp is on, so a UV sensor must always be present to prevent accidental exposure. More accurate, sensitive, and cheaper UV sensors are therefore desirable to ensure that the decontamination is effective and safe.

6.2. THEORY ON PHOTODETECTORS

Photodetection using semiconductors is based on the phenomenon that photons with sufficient energy can excite electrons from the valence band to the conduction band.

The energy of an incoming photon is inversely proportional to its wavelength, λ:

$$E = \frac{h * c}{\lambda} \tag{6.1}$$

Where h is Planck's constant and c the speed of light. A photon with a wavelength of 350 nm can thus excite electrons by 3.54 eV. If the bandgap of the material is higher than the incoming photon energy, no excitation occurs and the photodetector is blind to any light above that wavelength. Excitation and decay have various pathways, depending on the incoming photon energy, the bandgap, band structure, trap states in the bandgap, amongst others. The various ways in which an electrode can be excited or decayed are illustrated in Figure 6.2. If the photon has enough energy, the excitation can cause the electron to be ejected from the material entirely, known as the photoelectric effect, for which Einstein received the Nobel prize. [8] This principle can be used for photodetection (using a photocathode), but a milder version is used in microelectronic devices.
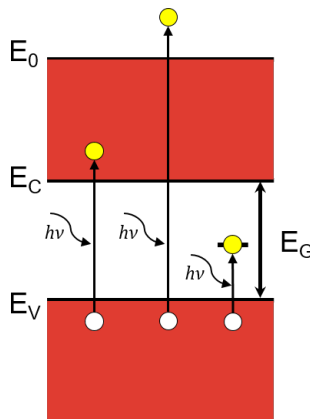
Figure 6.2: Diagram showing excitation of electrons from the valance band (E_V) to the conduction band (E_C) in a semiconductor by incoming photons with energy $h\nu$ (frequency $\nu = \frac{c}{\lambda}$. The vacuum energy level, E_0, and bandgap, E_G, are indicated. From left to right: excitation to the conduction band, electron emission (photoelectric effect), excitation to a trap state between the bands.

Here, the excited electrons stay within the material and thus increase the number of charge carriers, lowering the resistance. This resistance change can be measured, as done in a photoresistor, the simplest device. In a photodiode, exposing a p-n junction or rectifying metal-semiconductor junction to light separates the photogenerated charge carriers due to the electric field across the junction, changing the depletion layer width and, with it, the threshold voltage. Depending on the metal-semiconductor contact characteristic, a two terminal device is either a resistor or a photodiode. Photon-induced charge carrier generation can also be used in a three-terminal device to create a phototransistor since the bias depends on the number of charge carriers in the channel.

The photodetectors fabricated here are metal-semiconductor-metal (MSM) devices. Such devices consist of two metal contacts and a semiconductor connecting them. Metal-semiconductor contacts can be rectifying or not, depending on the work function, Φ_s, of

the semiconductor, and workfunction of the metal, Φ_m. If these two do not match, a barrier is formed, called a Schottky barrier. If the junction is not rectifying, we call it an Ohmic contact. The conditions to form a Schottky or Ohmic contact are summarized in table 6.1. The barrier height, Φ_B, can be approximated by the Schottky-Mott rule: $\Phi_B = \Phi_m - \chi_s$, with χ_s the electron affinity of the semiconductor. The simplified band structures of the different contacts are illustrated in Figure 6.3 for an n-type semiconductor, like ZnO. It follows that $\Phi_B \leq 0$ gives no barrier, so Ohmic contact. Unfortunately, these conditions can only be used as a rule of thumb.

In reality, effects such as Fermi-level pinning, local surface defects, crystal orientation, or diffusion between the two materials at the interface can drastically affect the formation and height of a barrier. Minor process deviations can affect one or more of these factors. Therefore, it is difficult to predict how the contact will behave and what caused this behaviour.

Semiconductor type	Schottky	Ohmic
n-type	$\Phi_m > \Phi_s$	$\Phi_m < \Phi_s$
p-type	$\Phi_m < \Phi_s$	$\Phi_m > \Phi_s$

Table 6.1: Conditions to form a Schottky barrier or not, assuming a simplified ideal case. Local surface states and other effects are ignored.

6

6.2.1. WIDE-BANDGAP SEMICONDUCTORS

Wide-bandgap (WBG) semiconductors have attracted significant interest by the semiconductor industry in the past decades because of their unique properties. [9] This class of materials consists of hard, thermally highly stable materials that can operate at much higher temperatures than silicon-based devices. [9–12] Furthermore, they are insensitive to visible light due to their wide bandgap. These properties make them attractive candidates for transparent conducting electrodes or harsh environment devices.

One application of WBG semiconductors is as UV-photodetector material because of their insensitivity to visible light. Compared to silicon-based devices, this simplifies the sensor design by removing any need to select the correct wavelength (using optical filters or readout electronics). This makes the sensor smaller, more energy efficient, and easier to produce. One of the challenges is that processing WBG semiconductor is difficult because of their mechanical hardness, high melting points, and chemical stability. This makes processing most semiconductors slow and complex, thus increasing costs. The most common WBG semiconductors are SiC and GaN, which recently have found commercial applications in power electronics. Although SiC and GaN are reaching more maturity, their processing is still hard. [12, 13] There is, therefore, room for alternative fabrication methods to create WBG-based UV sensors.

6.2.2. SPARK ABLATION SEMICONDUCTING NANOPARTICLES

In this chapter, we propose to use spark ablation generation to create WBG devices. The advantage of being able to deposit materials at room temperature on most substrates is simple and opens up printed sensors, sensors on paper, and additive manufacturing.

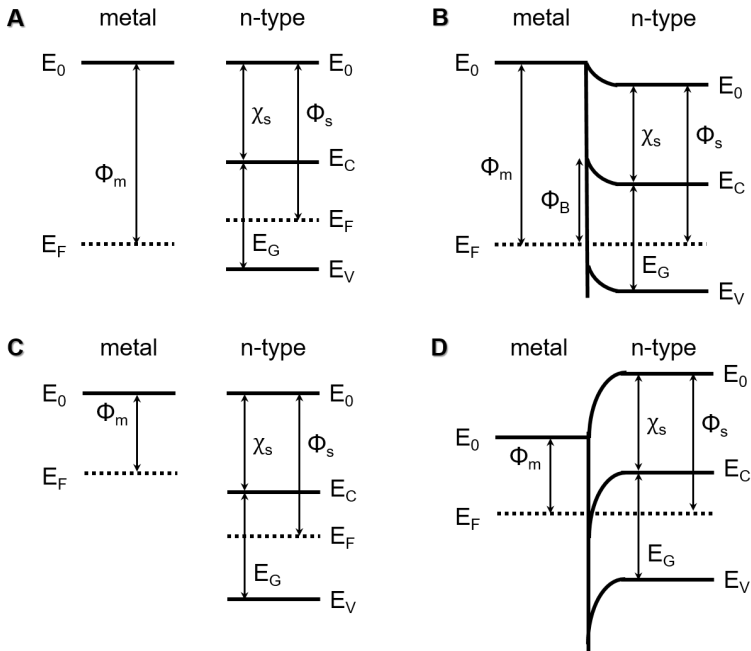Figure 6.3: Band diagram showing a metal and n-type semiconductor junction without contact (A and C) and with contact (B and D). When brought in contact, the Fermi levels, E_F, align, called Fermi level pinning, shifting the energy levels of the semiconductor. This causes band bending at the junction. A Schottky barrier Φ_B is formed with a high Φ_m as shown in B. A small Φ_m creates an Ohmic contact, shown in D.

At the same time, nobody has, to the best of our knowledge, tried to make functional devices using spark ablation generated semiconducting nanoparticles. No transistor or diode has successfully been made using spark ablation so far. Vons et al (2011) have published about the successful synthesis of unoxidized Si nanoparticles using this method but reported pyrophoric behaviour when brought in contact with air, making their application useless. [14]

To create (and apply) semiconducting nanoparticles we need to either protect them from oxygen or create oxidation-resistant semiconductors. It is a challenge to remove all oxygen from a gas-based synthesis method due to impurities in the gas and residual oxygen in the system. Chapter 2 discusses how to synthesize an oxygen-free nanoparticle, so this section will not elaborate on that further. After synthesis, the material must be protected without ever coming in contact with oxygen, another significant challenge. It is much simpler to make a material that is oxidation resistant. Examples of this are nitrides (e.g. AlN and GaN), carbides (e.g. SiC), and sulfides (e.g. Ag_2S, Cu_2S). Unfortunately, getting solid rods of these materials to ablate is difficult and synthesising them by reactive sparking or chemical reactions after deposition negates the simplicity of spark ablation. It is an exciting avenue to explore, but the simplest way of making a material that will not degrade in air after deposition is to lean into the oxidation sensitivity and synthesise an oxide. In the case of WBG semiconductors, the most promising oxide is ZnO.

6.2.3. ZnO FOR UV SENSING

ZnO is an oxide with a wurzite crystal structure and a direct 3.34 eV bandgap. Zinc is a highly abundant and cheap metal and Zn and ZnO products are deemed safe for human consumption and biodegradable. [15] Due to its biodegradability, safety, low cost, chemical and thermal stability, and direct wide bandgap, it has much potential as a WBG material, but it is not easy to create devices with it. ZnO crystals will have relatively many defects in the form of oxygen vacancies, making ZnO a natural n-type semiconductor. Heavy doping is required to create p-type ZnO. [16] Furthermore, metallic Zn is one of the most feared metallic contaminants in vacuum equipment due to its low vapour pressure. Dedicated equipment is therefore required to deposit ZnO without risk of contamination. A back-end compatible deposition process would circumvent this issue.

6.3. EXPERIMENTAL

6.3.1. DEVICE DESIGN AND FABRICATION

The first series of devices was made using the electrode structures shown in Figure 6.4. These four-point-probe structures are designed for simple resistance measurement of printed nanoparticle films. They have been fabricated on Si wafers with 300 nm of thermally grown SiO_2 for electrical insulation. The electrodes were deposited using thermal evaporation of a 10/100 nm Cr/Au layer. Chrome is the adhesion layer for the gold. We will refer to this batch of photoresistors as series 1, or S1.

To create a Schottky diode, we want a device with one Ohmic and one Schottky contact. This can only be achieved by using two different metals. The two masks seen in
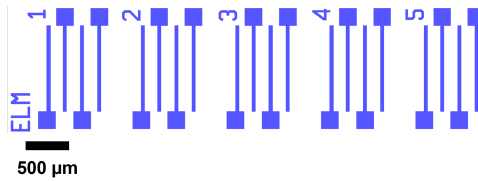
Figure 6.4: Design of the four-point probe electrodes. Spacing between two middle electrodes is 160 μm.

Figure 6.5 are used to make the two- and three-terminal devices in Figure 6.6. Adding a third terminal as in Figure 6.6B with Ohmic contact creates a metaloxide field-effect transistor (MOSFET) when the metaloxide is deposited on top of the source, drain, and gate. These samples made with these masks will be referred to as series 2 or S2.
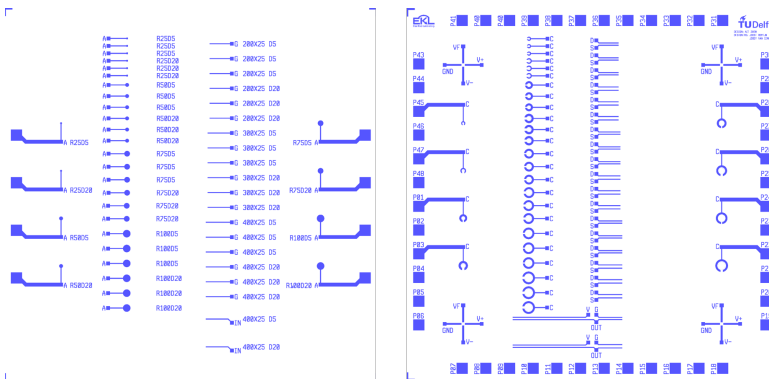
Figure 6.5: Masks for two metal designs with various electrode dimensions. The design contains two- and three terminal devices.

As discussed above, it is challenging to predict which metal will form Schottky contact with ZnO. Processing conditions and crystal quality have a large impact on the barrier. A range of metals was chosen to improve the chances of making the right contacts. The metals tested with these devices were TiN/Au, TiN/Pt, Au/Ag, and TiN/Ag. Since TiN and Ag have low work functions, and Pt and Au have high ones, we should be able to see different behaviour. Based on the review of Brillson and Lu (2011) [17], Pt and Ag should make Schottky contacts, while Au can make Ohmic or Schottky contacts and TiN should make Ohmic contact. 10/100 nm layers of Ta/Pt, Cr/Ag and Cr/Au were evaporated on the wafer, with Ta or Cr as the adhesion layers to SiO$_2$. TiN was sputtered using Ti as adhesion layer, resulting in a 10/100 nm Ti/TiN film. Two versions of these devices have been fabricated, one on silicon wafers, and the other on glass wafers (Corning Glass Wafers). The glass wafers were used specifically for UV responsivity analysis, because they effectively rule out light reflection by the layers below the ZnO film which would doubly expose the nanoparticle film to the light and misleadingly increase the apparent responsivity.

After fabrication, the devices were coated with a line of Zn nanoparticles generated
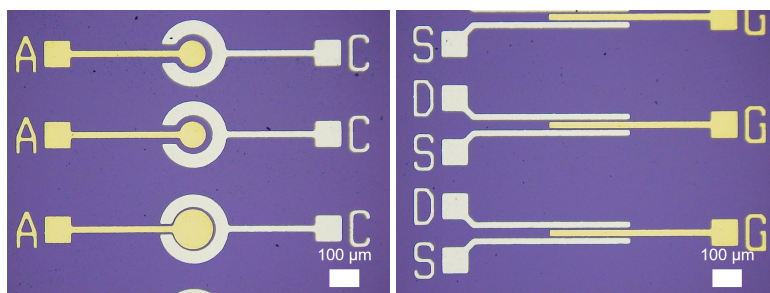
Figure 6.6: Examples of fabricated two terminal (left) and three terminal (right) devices made of Au and Ag using the masks in Figure 6.5.

by the VSP G1 using Zn electrodes with 2% Al as a dopant to increase the conductivity. Although literature shows the optimal Al doping percentage is around 0.8-1.5 %, 2% has a higher conductivity, which was more important for the low conductivity films our synthesis method creates. [18, 19] Generation current and voltage were 3 mA and 1 kV. Higher spark power resulted in excessive production and buildup of much residue in the generation chamber and, in time, irregular sparking. A 1.5 l min^{-1} Ar with 5% H$_2$ carrier gas was used to suppress oxidation during synthesis deposition.

Annealing was required in any case (see section 6.4.1), and increased particle coalescence can be achieved if more oxidation occurs after deposition. Annealing in a ceramic oven at 100 to 600 °C was done to oxidize the Zn. The S1 samples have been annealed at 600 °C, while the S2 samples were heated to a maximum of 400 °C. Annealing times varied depending on the device metallization.

6.3.2. MATERIAL AND DEVICE CHARACTERIZATION

Structure characterization was done by scanning electron microscopy using a Hitachi Regulus 8230 operated at 5 kV acceleration voltage and a XL30 SFEG for EDX, also operated at 5 kV. X-ray diffraction was done using a Brucker D8 diffractometer with Cu Kα radiation.

For electrical characterisation, a Formfactor Summit probe station was used. 5 mW 265 nm LEDs were mounted in the probe station to illuminate the devices for measuring the charging and discharging time under UV-C exposure. To measure the response per wavelength, a spectral responsivity setup was used to measure the response per wavelength. The setup diagram is shown in Figure 6.7. It consists of a combination of a deuterium and a halogen lamp (Bentham D2-QH Deuterium-Halogen Source), whose output is connected to a monochromator (Horiba iHR320). The wavelengths this setup can emit range from 200 to 400 nm. The selected wavelength is focused on the sample by a UV reflective mirror (Thorlabs CM750-200-F01). The relative output of the photodetector is expressed as voltage per wavelength, and a readout circuit has been designed to read out low output voltages. This setup could be operated in two modes: AC and DC. When operating in AC mode, an AMETEK 7225 Dual Phase DSP lock-in amplifier was used to readout the PCB and feed the data to the PC. In DC mode, a Keithley 2450 Source

measure unit (SMU) was used to readout the PCB. Devices were mounted in the PCB after wirebonding to a DIL package.
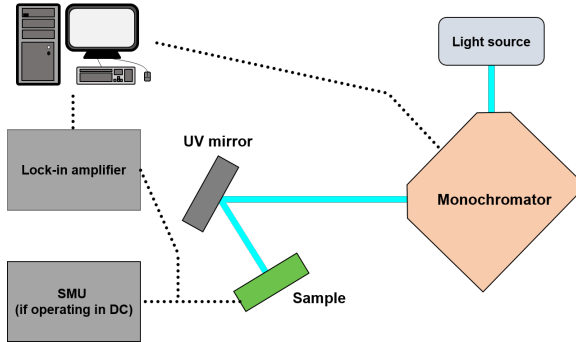
Figure 6.7: Schematic of the UV-measurement setup. The SMU would be used if the setup is used in DC mode, otherwise, the data is recorded on the PC.

Transmittance spectroscopy was performed using a Perkin Elmer LAMBDA 1050+ UV/Vis/NIR Spectrophotometer to characterise the tranparency of the ZnO films and extract the bandgap energy. Pieces of boro-aluminosilicate glass wafer (Corning Glass Wafers, 500 μm thick) of 2.2×2.2 mm were coated completely with a layer of annealed ZnO nanoparticles for these experiments.

6.4. RESULTS

6.4.1. STRUCTURE ANALYSIS
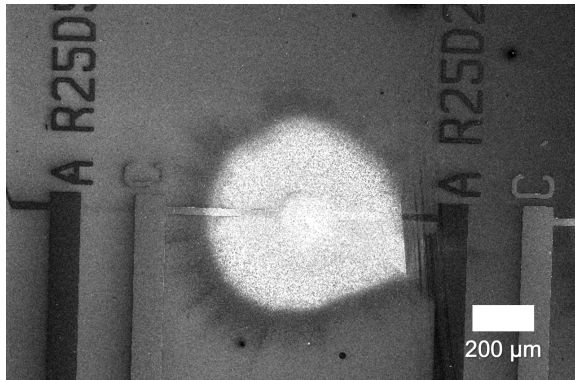
Figure 6.8: Dot on a pair of Au/TiN electrodes after 5 minutes of deposition. The center of the dot is directly on the circular electrodes.

A dot as printed in Figure 6.8 shows good coverage of the device, with the thickest part of the film right above the electrodes. No large cracking is visible in these samples so the film does not crack due to thermal stress during annealing or due to stress induced by the layer thickness. It was discovered that thermal oxidation was necessary to

turn the Zn into ZnO, and a range of temperatures and annealing times were tested to find the optimal annealing temperature. An optimum of 600 °C was found for minimal resistance for the S1 samples. This was the starting point for further optimization with the S2 samples.

The metallization of the electrodes limited the annealing conditions for Ag and TiN devices. TiN is stable at room temperature but begins to oxidize at 500 °C, forming TiN_xO_y and ultimately TiO_2. Silver is highly oxidation resistant, but dewets when heated too much. For these reasons, the optimal annealing temperature for the S2 samples was 400 °C for 2 hours for the Ag-containing devices and for 5 hours for all other devices. Although 5 hours is excessive, it guarantees a thermally stable and fully oxidised film with minimal electrical resistance.

The effect annealing has on the composition can be most clearly seen by EDX. The results displayed in table 6.2 show a nearly 3:1 ratio of Zn to O atoms, indicating that the nanoparticles have a thin oxide shell around them. After annealing at 400 °C, we see a nearly 1:1 ratio, or almost full oxidation. The Si here is in the form of SiO_2 and some oxygen should be attributed to it in the EDX results. There could be oxygen vacancies in the nanocrystals, which can affect the material's UV sensing performance. However, the slight shortage of oxygen found by Zn is within the error of the analysis, so it is hard to quantify how many oxygen vacancies there can be precisely.

	Before annealing			After annealing		
Element	Weight%	Atom%	Error %	Weight%	Atom%	Error %
Zn	89.74	73.76	3.13	56.01	44.60	2.96
O	7.39	24.81	5.72	13.97	45.45	5.33
Si	-	-	-	1.27	2.35	9.75

Table 6.2: EDX results of ZnO film before and after annealing at 400 °C for 4 hours. Only the relevant species are shown, not the metallic substrate underneath, since they do not influence the Zn:O ratio. Si was not detectable in the before spectrum because it was measured at a slightly thicker area and thus the X-rays did not penetrate deep enough.

The microstructure of the nanoparticles seems not to change much. SEM images show no change in porosity or structure before or after annealing, as visible in Figure 6.9. The film is highly porous with large spherical clusters coated with smaller particles. These clusters are present before annealing, so they must be formed during synthesis. It appears they are dense agglomerates of smaller particles. The XRD results agree with this too. Applying the Scherrer formula (see appendix B) to the peaks in Figure 6.10 using the integral breath of the peaks gives a mean grain size of 19 nm. The 102 plane (represented by the 4th peak) has an outlying 7 nm size, suggesting a rod shape. The nanoparticles appear to be round in the SEM images, not rod shaped as suggested by the XRD size estimation. It was thus decided the 102 plane size was excluded from the grain size average. As visible in Figure 6.10, the annealed nanoparticles are crystalline and have a hexagonal crystal structure, and no other phases can be identified. The lack of a wide shoulder underneath the peak areas suggests that there is no amorphous ZnO or phase present and the absence of Zn peaks proves that the nanoparticles have fully oxidized.
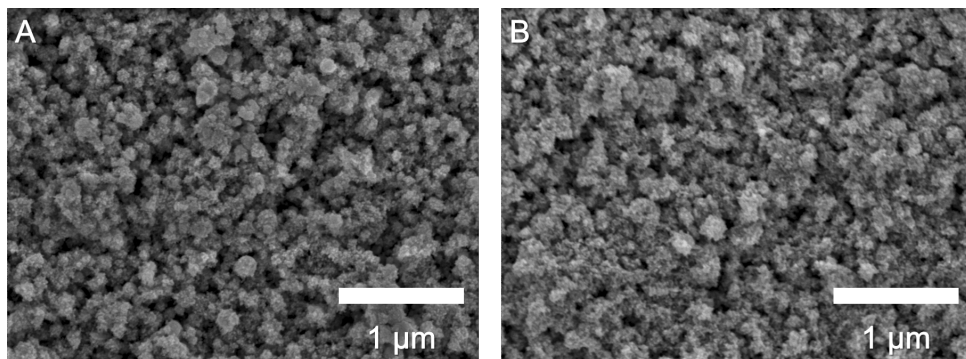
Figure 6.9: SEM images of a sample on an Ag bondpad before (A) and after (B) annealing at 400 °C.

6
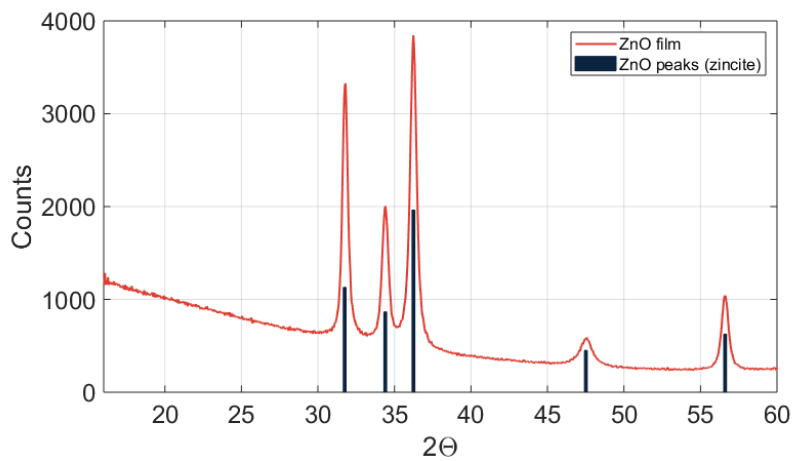
Figure 6.10: XRD result of an annealed ZnO NP film on silicon. The peaks perfectly match the pattern for zincite.

6.4.2. TRANSMITTANCE RESULTS

To confirm that the ZnO film is optically transparent and to what wavelength, transmission spectroscopy was done from 225 nm to 550 nm. As seen in Figure 6.11, the boroaluminosilicate glass is highly optically transparent, with > 90% transparency until 350 nm, after which transparency steeply declines. The 200 nm ZnO coating applied on this substrate absorbs nearly no visible light, lowering transparency only by several percentage points. At 380 nm, around the bandgap of ZnO, a sharp decline of transparency can be observed that plateaus briefly but continues to lower with higher energy light when the glass substrate contributes.
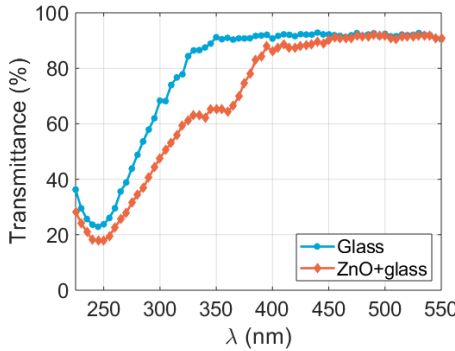
Figure 6.11: Transmittance per wavelength for the glass substrate and a sample of 200 nm thick. The sample barely has lower transparency compared to the glass until the end of the visible spectrum, showing the good transparency to visible light of ZnO.
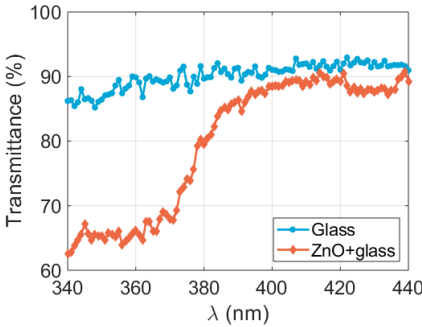
Figure 6.12: Transmission of glass and ZnO coated glass between 340 and 440 nm for extracting the bandgap energy.
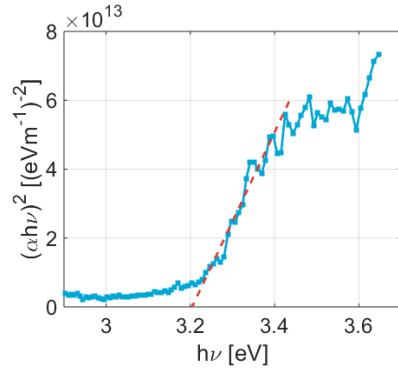
Figure 6.13: $(\alpha h\nu)^2$ as a function of photon energy. The linear fit is plotted and extrapolated to interact the x-axis.

$$\alpha = \frac{1}{d} \ln\left(\frac{100}{I}\right) \tag{6.2}$$

$$(\alpha h\nu)^2 \propto \sqrt{h\nu - E_g} \tag{6.3}$$

It is possible to extract the bandgap from transmittance data using the absorption coefficient α. [20, 21] α is dependent on the transmittance I and film thickness d according to equation 6.2, and can be calculated from the data in Figure 6.11. To get a better value for the bandgap, a higher resolution measurement was done with a smaller spectral range, seen in Figure 6.12. Knowing that α is related to the incoming photon energy $h\nu$ and the bandgap E_g according to equation 6.3, we can plot $(\alpha h\nu)^2$ as a function of $h\nu$, as seen in Figure 6.13. The slope of the linear part of the curve (the dotted line) follows $y = a_1(h\nu) + a_2$, so at the intersection of the x-axis ($\alpha = 0$), we should have $h\nu = E_g$, giving $E_g = -\frac{a_2}{a_1}$. Applying this to our data, we find $E_g = 3.21$ eV. This is close to the literature value for the bandgap of ZnO, which is reported to be 3.3 eV for pure monocrystalline ZnO. [20, 22] The difference can be attributed to crystal imperfections, creating more states within the bandgap, lowering the effective barrier.

6.4.3. ELECTRICAL CONDUCTIVITY

As discussed before, it is hard to predict in advance what the behaviour of a metal-semiconductor junction is, particularly when the material consists of nanoparticles with a new synthesis method. Several metals were tested to see if some combinations reliably make either a photoresistor or a photodiode. However, there was no consistency in the type of contact for a metal, even if the fabrication of the devices was the same. Figure 6.14 shows, for example, three TiN devices with different contacts that contradict each other. All samples are the same device with identical ZnO deposition and annealing, but show different contact behaviours with TiN. In fact, it turned out that all tested metals could have Ohmic contact.
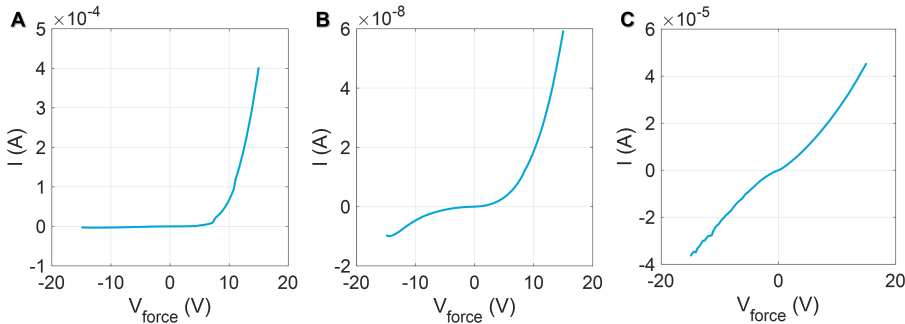
Figure 6.14: Three of the same TiN-Au devices on three different samples showing different behaviour. A) Single Schottky contact (diode), B) double Schottky contact, C) double Ohmic contact.

Several reasons can exist for this unpredictability. First, it matters which atom crystal plane (or phase) is in contact with the metal. In the case of spherical nanoparticles, this is not known, but the random orientation of the particles makes sure that all planes should be making contact if the electrode area is large enough. Secondly, the curvature of the nanoparticles changes the local band structure. Not only are there many defects at

the surface, but the stress in the crystal lattice from the curvature also distorts the band structure. Third, although great care was taken to make the processing of each sample the same, slight changes in the processing or nanoparticle synthesis can change the behaviour at the interface. Surface contamination, slightly different sized ZnO particles or impurities in either the metal or nanoparticle can all affect the junction. Lastly, it can not be excluded that the annealing step changes the junction. Electrode oxidation or nanoparticle structure change can influence how the junction behaves. Ultimately, it is extremely difficult to find why the contact is rectifying or not and it would require extensive characterisation of the metal-semiconductor interface, which was not the goal of these experiments. Due to the unpredictability in the S2 samples, it was decided to fall back on previously fabricated samples with good Ohmic behaviour to study the UV sensing behaviour in more detail. These S1 samples show a resistance of 53 MΩ in darkness, effectively acting as an insulator.

Despite the unpredictability of the S2 results, it was possible to fabricate diodes. Figure 6.15 shows a successful photodiode with a threshold voltage of around 5 V. This is, to our knowledge, the first published diode fabricated using spark ablation generated nanoparticles.
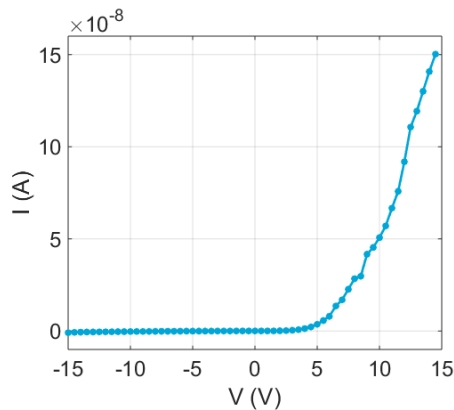
Figure 6.15: IV curve of a TiN/Au Schottky diode in darkness.

6.4.4. UV SENSING RESULTS

Because of a lack of consistency in the S2 devices, it is hard to draw any conclusive results from the data. In successful Schottky diode devices, the response (see Figure 6.16) is higher and peaks around 285 nm. The output voltage is very low (close to the bandgap of ZnO) suggesting good selectivity. However, the responsivity shows a different picture. Figure 6.17 show a significant responsivity in the near UV region, not even a full order of magnitude lower than the peak responsivity at 310 nm and comparable to the response in the UV-C region (100-280 nm). Response in the near UV region suggests there are (local) effects that lower the bandgap.

The older series 1 samples showed a slow, but good reponse to UV exposure. The charging and discharging time have been extracted from Figure 6.19. It takes 79 seconds
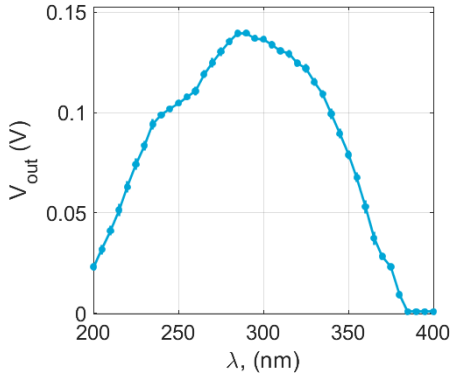
Figure 6.16: Voltage output for a TiN/ZnO/Au Schottky diode. Peak response is at 285-290 nm
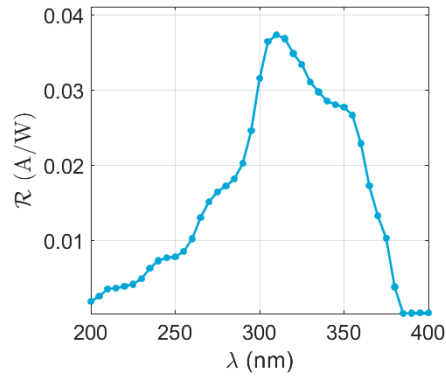
Figure 6.17: Responsivity of the same diode as Figure 6.16. Peak responsivity is at 310 nm.

to reach 90% of the plateau value and 82 seconds to reach 10% above the dark current after switching on the 265 nm UV lamp. This slow response can be explained by their large size in combination with ad-and desorption of oxygen under exposure to UV light. [23] This is a slow process that occurs at the surface of ZnO and radically changes the conduction behaviour. Nevertheless, the resistance reduces by two orders of magnitude under illumination, as seen in Figure 6.18. The charging and discharging is slower than other reported devices, but the two orders of magnitude repsonse is comparable. [10, 11, 24–27] The devices made with this design (fig. 6.4 was not designed to be a fast sensor, but to measure film resistances, so there is definitely room for improvement. Smaller devices with a higher length-over-width ratio should respond faster.
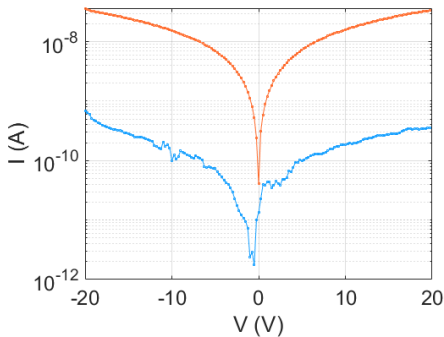
Figure 6.18: Semilogarithmic IV curve of a S1 device in darkness (blue) and under 265 nm illumination (orange). Inset: The same data plotted with a linear y-axis. Data acquired after 5 min. waiting time.
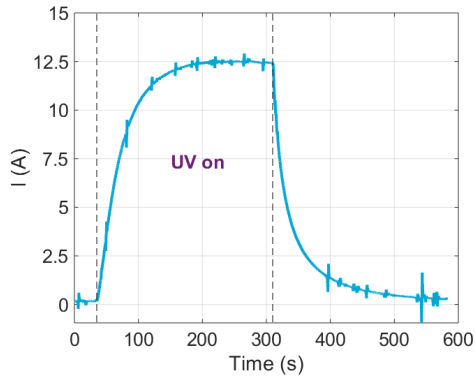
Figure 6.19: Photo-response curve of a S1 device showing charging and discharging behaviour during and after exposure to 265 nm UV light. Measurement done at 5 V.

The generated voltage and responsivity of these S1 devices has been measured too. Figure 6.20 shows the voltage output of three devices made on one sample. They have been measured using 3 electrode distances, so each device has a different exposed area. The largest exposed area generates more charge carriers and, thus, a higher output voltage. The responsivity of the devices (Figure 6.21) peaks at 305 nm, a slightly lower wavelength than the diode described before. The devices show nearly no responsivity in the near-UV region, meaning they are optically blind.
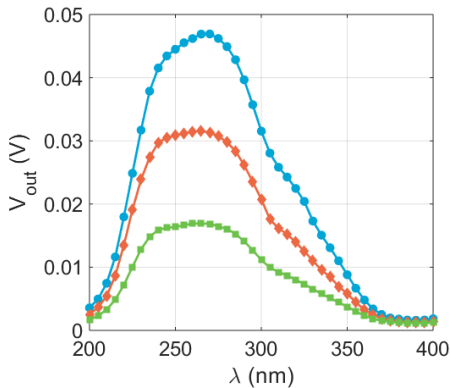
Figure 6.20: Voltage generated per wavelength for three devices on one printed ZnO line at a 5 V bias. Device 1 (green) is 140 μm wide, device 2 (red) is 340 μm wide, and device 3 (blue) is 540 μm wide.
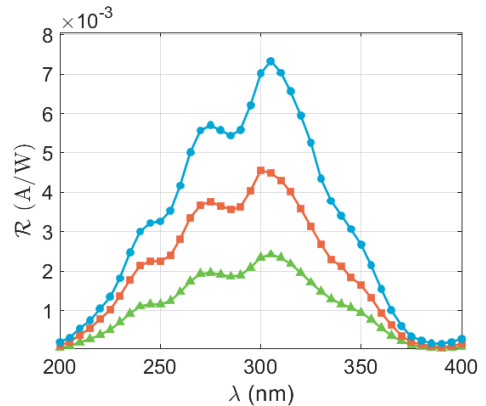
Figure 6.21: Response per wavelength between 200 and 400 nm for the same three devices in fig.6.20. The peaks are at 305 nm and there is a second peak at 275 nm.

6.5. CONCLUSIONS AND FUTURE WORK

This experiment successfully demonstrated the first optoelectronic devices and the first diode made using spark ablation nanoparticles. The nanoparticles have a bandap of 3.3 eV, close to that of bulk ZnO, and are transparent to visible light. An attempt was made to fabricate photodiodes, with mixed results. It proved difficult to reliably create a Ohmic or Schottky contact with the same electrode metals, but a Schottky diode was made. This diode showed blindness to visible light and a peak responsivity of at 310 nm. Older ZnO resistors showed similar visible light blindness and over two orders of magnitude resistance reduction after 265 nm light exposure. The charging time of this device was 79 seconds to reach 90% of the plateau and discharging to 10% above the dark current took 82 seconds. This slow response is known for ZnO and attributed to the adsorption and desorption of oxygen caused by the irradiation. The responsivity of these devices was lower than the diode, but peaked nearly at the same wavelength at 305 nm.

6.5.1. FUTURE WORK

Although these devices work and are blind to visible light, they are far from perfect. The primary issue is their slow response, which makes their practical applicability limited. Because this is due to oxygen adsorption, we can avoid it by air-tight packaging that is optically transparent, like a sapphire window above the sensor. However, this might

reduce the sensitivity, since now charge carrier generation would only be caused by photon induced excitation. Secondly, the devices are large, which helps generate a large current, but also increases resistance. Interdigitated electrodes can give the same amount of charge carriers, but have much lower resistance, making them more sensitive.

Third, a better understanding is required of the metal-semiconductor junction formed with these ZnO nanoparticles. It was impossible to predict if a junction would have a Schottky contact, even with the same synthesis settings and devices, which hampers reproducibility. A more in depth-study on the junction interface, perhaps a different metal selection, or better synthesis and annealing settings are needed. Once it is possible to reliably fabricate ZnO diodes, it becomes attractive to continue to three terminal devices and fabricate transistors. This would open up potential applications in printed electronics by printing the full circuit (traces, electrodes, and semiconductor layers) using spark ablation.

Furthermore, after further optimization of the device, it is interesting to see if the devices can be fabricated on flexible substrates or chip packaging. This would enable low-cost and highly versatile UV exposure monitoring with visible light blind sensors.

REFERENCES

[1] H. J. van Ginkel, M. Orvietani, J. Romijn, G. Q. Zhang, and S. Vollebregt, *ZnO nanoparticle printing for UV sensor fabrication,* in *2022 IEEE Sensors* (IEEE, 2022).

[2] B. M. Andersen, H. Bånrud, E. Bøe, O. Bjordal, and F. Drangsholt, *Comparison of UV-C light and chemicals for disinfection of surfaces in hospital isolation units,* Infection Control and Hospital Epidemiology **27**, 729 (2006).

[3] G. Knight, *Monitoring of ultraviolet light sources for water disinfection,* in *Conference Record of the 2004 IEEE Industry Applications Conference, 2004. 39th IAS Annual Meeting.* (IEEE, 2004).

[4] N. Storm, L. G. A. McKay, S. N. Downs, R. I. Johnson, D. Birru, M. de Samber, W. Willaert, G. Cennini, and A. Griffiths, *Rapid and complete inactivation of SA-CoV-2 by ultraviolet-C irradiation,* Scientific Reports **10** (2020), 10.1038/s41598-020-79600-8.

[5] M. Buonanno, D. Welch, I. Shuryak, and D. J. Brenner, *Far-UVC light (222 nm) efficiently and safely inactivates airborne human coronaviruses,* Scientific Reports **10** (2020), 10.1038/s41598-020-67211-2.

[6] S. Roosegaarde, *World' s first urban sun cleans public space of coronavirus for better human gatherings,* Online (2021).

[7] R. A. Rohde, *Solar spectrum,* commons.wikimedia.org/w/index.php?curid=24648395 (2023).

[8] A. Einstein, *Über einen die erzeugung und verwandlung des lichtes betreffenden heuristischen gesichtspunkt,* Annalen der Physik **322**, 132 (1905).

6

[9] P. R. Wilson, B. Ferreira, J. Zhang, and C. DiMarino, *IEEE ITRW: International tech-nology roadmap for wide-bandgap power semiconductors: An overview,* IEEE Power Electronics Magazine **5**, 22 (2018).

[10] P. Shewale and Y. Yu, *UV photodetection properties of pulsed laser deposited Cu-doped ZnO thin film,* Ceramics International **43**, 4175 (2017).

[11] X. Liu, L. Gu, Q. Zhang, J. Wu, Y. Long, and Z. Fan, *All-printable band-edge mod-ulated ZnO nanowire photodetectors with ultra-high detectivity,* Nature Communi-cations **5** (2014), 10.1038/ncomms5007.

[12] J. Romijn, S. Vollebregt, A. May, T. Erlbacher, H. W. van Zeijl, J. Leijtens, G. Zhang, and P. M. Sarro, *Visible blind quadrant sun position sensor in a silicon carbide tech-nology,* in *2022 IEEE 35th International Conference on Micro Electro Mechanical Sys-tems Conference (MEMS)* (IEEE, 2022).

[13] S. Hou, M. Shakir, P.-E. Hellstrom, B. G. Malm, C.-M. Zetterling, and M. Ostling, *A silicon carbide 256 pixel UV image sensor array operating at 400 °c,* IEEE Journal of the Electron Devices Society **8**, 116 (2020).

[14] V. Vons, A. Anastasopol, W. Legerstee, F. Mulder, S. Eijt, and A. Schmidt-Ott, *Low-temperature hydrogen desorption and the structural properties of spark discharge generated Mg nanoparticles,* Acta Materialia **59**, 3070 (2011).

[15] U. G. Survey, *Mineral Commodity Summaries 2019,* Tech. Rep. (U.S. Geological Sur-vey, 2019).

[16] Y. Wang, C. Zhou, A. M. Elquist, A. Ghods, V. G. Saravade, N. Lu, and I. Ferguson, *A review of earth abundant ZnO-based materials for thermoelectric and photovoltaic applications,* in *Oxide-based Materials and Devices IX,* Vol. 10533, edited by D. J. Rogers, D. C. Look, and F. H. Teherani, International Society for Optics and Photon-ics (SPIE, 2018) pp. 163 – 179.

[17] L. J. Brillson and Y. Lu, *ZnO schottky barriers and ohmic contacts,* Journal of Applied Physics **109**, 121301 (2011).

[18] S. Mridha and D. Basak, *Aluminium doped ZnO films: electrical, optical and pho-toresponse studies,* Journal of Physics D: Applied Physics **40**, 6902 (2007).

[19] J. Hu and R. G. Gordon, *Textured aluminum-doped zinc oxide thin films from at-mospheric pressure chemical-vapor deposition,* Journal of Applied Physics **71**, 880 (1992).

[20] K. C. Park, D. Y. Ma, and K. H. Kim, *The physical properties of Al-doped zinc oxide films prepared by RF magnetron sputtering,* Thin Solid Films **305**, 201 (1997).

[21] D. Zhang, Y. He, and C. Z. Wang, *Structure and optical properties of nanostructured zinc oxide films with different growth temperatures,* Optics & Laser Technology **42**, 556 (2010).

[22] D. Look, C. Coşkun, B. Claflin, and G. Farlow, *Electrical and optical properties of defects and impurities in ZnO,* Physica B: Condensed Matter **340-342**, 32 (2003).

[23] G. Wisz, I. Virt, P. Sagan, P. Potera, and R. Yavorskyi, *Structural, optical and electrical properties of zinc oxide layers produced by pulsed laser deposition method,* Nanoscale Research Letters **12** (2017), 10.1186/s11671-017-2033-9.

[24] H. S. Al-Salman and M. Abdullah, *Fabrication and characterization of undoped and cobalt-doped ZnO based UV photodetector prepared by RF-sputtering,* Journal of Materials Science Technology **29**, 1139 (2013).

[25] S. Panda and C. Jacob, *Preparation of transparent ZnO thin films and their application in UV sensor devices,* Solid-State Electronics **73**, 44 (2012).

[26] Z. Ke, Z. Yang, M. Wang, M. Cao, Z. Sun, and J. Shao, *Low temperature annealed ZnO film UV photodetector with fast photoresponse,* Sensors and Actuators A: Physical **253**, 173 (2017).

[27] A. J. Gimenez, J. M. Yáñez-Limón, and J. M. Seminario, *ZnO-paper based photoconductive UV sensor,* The Journal of Physical Chemistry C **115**, 282 (2010).

6

7

CONCLUSIONS AND RECOMMENDATIONS

Now, here's the meaning of life. Well, it's nothing very special: Try to be nice to people, avoid eating fat, read a good book every now and then, get some walking in, and try and live together in peace and harmony with people of all creeds and nations.

Monty Python's The Meaning of Life

7.1. CONCLUSIONS

THE chapters in this thesis that discussed the scientific findings of my PhD work show a diverse set of applications in which spark ablation generated nanoparticles could be applied. I will briefly summarize the findings of each chapter here. They are as follows:

- Chapter 3 investigated the use of QCM for measuring the mass of a nanoparticle thin film, and derive the porosity from the volume. It was shown that the mass deposition rate scales linearly with spark frequency, despite mass losses in the system. It was also found that the density of deposited Au nanoparticle films is 15.95 g cm^{-3}, giving a porosity of $\Theta_p = 0.18$ and that those values are constant for all tested settings. This was attributed to the restructuring of the film during impaction, making them denser than previous models predicted.

- Chapter 4 showed the applicability of Au nanoparticle lines as printed conducting lines. Freshly printed Au nanoparticle lines have a 22 times worse conductivity than bulk gold. Annealing at 100 °C improves the conductivity slightly, but at 200 °C, the film shrinks due to partial melting and the conductivity increases by 60%. Comparable Au lines were used to fabricate interconnects on the side of a chip, showing promising results on Si-to-Si samples and on Si-to-paper samples too, albeit more unreliably. Printing Au interconnects like this can become a viable alternative to wirebonding or TSVs.

- In the same chapter, a method is demonstrated to further miniaturise nanoporous films by using lift-off. Using this method, 1.2 μm wide structures were fabricated while the impact on the film was small.

- Thermoelectric nanoparticles made of Bi$_2$Te$_3$ were investigated in chapter 5. It was found that the films had a reasonable Seebeck coefficient of $S = -88.3 \pm 1.2$ μV K^{-1}. An excellent thermal conductivity of $\kappa = 0.2$ W m^{-1} K^{-1} at room temperature was obtained, comparable to state-of-the-art nanostructured Bi$_2$Te$_3$ and a tenfold reduction compared to bulk Bi$_2$Te$_3$. This was unfortunately offset by a low electrical conductivity, resulting in an overall loss in thermoelectric efficiency. The change of the sample over time was monitored to study the effect of oxidation on the sample and it was found that the electrical conductivity decreases quickly and immediately after deposition, while the Seebeck coefficient improved and thermal conductivity reduced. This emphasizes the importance of immediate airtight packaging after deposition.

- The closing chapter 6 tested the applicability of using the wide band-gap semiconductor ZnO as UV sensor. This resulted in the first functional microelectronic devices (Schottky diodes) made using spark ablation. ZnO photoresistors showed a 100 times resistance reduction when exposed to UV light. The response time was long, in the order of minutes, due to the slow sensing mechanism of oxygen adsorption and desorption.

7.2. ANSWERS TO THE RESEARCH QUESTIONS

In chapter 1, I formulated several research questions to be answered:

1. What is the effect of the nanoporous structure on the electrical and thermal properties of a nanoparticle film?

2. Are printed nanoparticle lines applicable as interconnect materials?

3. Can we use semiconductor nanoparticles for thermoelectric or opto-electronic devices?

To answer question one, we can conclude that the porosity of a Au film is surprisingly low (see chapter 3), but that it has a disproportionally high effect on the electrical conductivity (see chapter 4. Even annealing did not completely offset this. This is even worse for materials that do not restructure as much during deposition such as Bi_2Te_3, which has an even larger reduced conductivity. From chapter 5 we can also conclude that nanostructuring a bulk material drastically reduces its thermal conductivity but that it also makes the films oxidize faster due to the large surface area. This reduces the electrical conductivity even further, beginning immediately after deposition.

Printed nanoparticle lines are suitable for printed electronics and interconnect materials, as shown in chapter 4. Freshly printed, the conductivity of Au lines is roughly twenty times worse than bulk gold and after annealing, this can be improved to only eight times worse. The conformity of the printed lines to the sample morphology makes it a versatile method. After more optimisation, deposited nanoporous lines generated by spark ablation can be a viable alternative for wirebonds or TSVs with soft or ultrahard substrates.

The last two chapters, 5 and 6, answer the last research question. Thermoelectric nanoparticles are possible and show a tenfold reduction in thermal conductivity but a much more reduced electrical conductivity, resulting in a worse thermoelectric performance. Unless a high Seebeck coefficient material is found that can compensate for this loss in conductivity, it will not be feasible to apply this material. For optoelectronic applications, wide band-gap oxides such as ZnO are simple to synthesise using spark ablation and show promising results as UV sensors. The devices show no response to visible light and a good but slow response to UV light. With some optimization, ZnO photodiodes can be manufactured using spark ablation nanoparticles.

7.3. RECOMMENDATIONS FOR FUTURE WORK

This thesis explored several applications for printed nanoparticles for the first time. As such, many of the presented results can be much improved with some further optimization or research. There are also further research directions possible that build on the groundwork in this thesis. Some recommendations can be made:

- The biggest challenge for the application of most metal nanoparticles is oxidation. Reduced or prevented oxidation opens up the application of non-noble metals and vastly increases the potential for spark ablation. To protect from oxidation after deposition, in-situ packaging solutions must be developed or the nanopar-

ticles must be protected with a coating, which would limit their applicability. In applications where environmental exposure is required (e.g. gas sensing), oxides are unavoidable.

• Although the conductivity of Au is reasonable, the conductivity of semiconductors is much reduced. This thesis has not investigated the cause of this, but it must be investigated for the successful application of semiconductors. In particular, for metal oxides, this is important due to their already low conductivity. Improved deposition recipes or the use of dopants should be explored.

• It has been demonstrated that a Schottky diode can be fabricated, but its behaviour is unpredictable. Better electrode-nanoparticle material combinations need to be selected to reliably create nanoparticle-based microelectronic devices. Potentially, a fully printable transistor can be made using these films.

• Besides the simplicity of spark ablation, its biggest advantage is material flexibility to print with. Operation of several generators, mixed electrodes or with two different electrodes opens up nearly endless possible compositions. Combined with artificial intelligence, it has the potential to become an effective material screening process to optimize compositions or test entirely new ones. This could enable fast screening of materials for, for example, catalysis, gas sensing, and thermoelectricity.

• The flexibility in materials to print on and print with makes the nanomaterial printer a powerful tool for flexible electronics and additive manufacturing of both conducting patterns and functional layers. To make it commercially viable, a high nanoparticle production rate is crucial so meters per second writing speeds become realistic. Both improved generators and printers must be developed to reach this.

7

A

G-CODE EXAMPLE TO WRITE A 3 MM LINE OF NANOPARTICLES

This example is the minimal required code to make a deposit after nozzle alignment.

In the example below, the alignment sequence (line 1-3) begins with the camera above the starting point and the nozzle moves to a 1 mm height in line 3. Calibration has been done before deposition to ensure this path ends at 1 mm. Alignment is performed in absolute coordinates (G90) to make sure it is constant in all deposits. The M9 command (line 5) closes the solenoid valve of the flushing gas and deposition begins. After being set to move in relative coordinates (G91) to make path programming simpler, the nozzle moves 3 mm to the right (X3) at a speed of 3 mm per minute (F3) before deposition ends (M8). The nozzle then moves back to its origin and the camera is brought back in focus on the starting point (line 10).

```
1  G90
2  G92 X0 Y0 Z0
3  G1 X1.95 Y-16.45 Z-1.3 F200
4  G91
5  M9
6  G1 X3 F3
7  M8
8  G90
9  G1 X0 Y0 Z0 F200
```

B

READOUT CODE FOR QCM MEASUREMENT

This appendix includes the Arduino code used to measure the QCM frequency and the Matlab code to read the serial data and generate a live graph of the frequency.

The Arduino code is adapted from the openQCM code supplied with their QCM readout boards. The original code can be found on https://github.com/openQ together with their Java application for easy readout

B.1. ARDUINO CODE

The alterations make the Arduino sample the QCM frequency 5 times per second, resulting in a resolution of 5 Hz, instead of the 1 Hz that is the default. This has been done to get a higher resolution in the time domain to more clearly see the effect of the nozzle location. Typical frequency changes are in the hundreds of Herz, so the readout resolution loss is acceptable. Furthermore, it only sends the frequency over the serial port as a string, not the temperature or other information. This was done to simplify the data processing and speed up the code. The temperature is stable during the entire deposition process, so there is no need to record it.

```
1   /* INTRO
2   * openQCM is the unique opensource quartz crystal microbalance http://openqcm.com/
3   * openQCM Java software project is available on github repository
4   * https://github.com/marcomauro/openQCM
5   *
6   * Measure QCM frequency using FreqCount library developed by Paul Stoffregen
7   * https://github.com/PaulStoffregen/FreqCount
```

```
8     *
9     * NOTE        - designed for 6 and 10 Mhz At-cut quartz crystal
10    *             - 3.3 VDC supply voltage quartz crystal oscillator
11    *             - Thermistor temperature sensor
12    *
13    * author      Marco Mauro
14    * version     1.3
15    * date        May 2015
16    *
17    * Further modifaction by Joost van Ginkel:
18    *    - It now writes only the frequency directly to the serial port
19    *    - Ignores the crystal temperature.
20    *    - It also samplels every 200 ms, instead of 1000 ms
21    */
22
23    // include library for frequency counting
24    #include <FreqCount.h>
25    // include EERPOM library
26    #include <EEPROM.h>
27    #include "Adafruit_MCP9808.h"
28    #include <Wire.h>
29
30    // fixed "gate interval" time for counting cycles
31    #define GATE   200.0 //Set to  200 ms, so 5 samples per seconds
32    // current address in EEPROM series
33    #define ADDRESS_SERIES 0
34    // current address in EEPROM first number
35    #define ADDRESS_NUMBERFIRST 1
36    // current address in EEPROM second number
37    #define ADDRESS_NUMBERSECOND 2
38
39    // QCM frequency by counting the number of pulses in a fixed time
40    // Initialize variables
41    unsigned long frequency = 0.0;
42    unsigned long TrueFreq = 0.0;
43    unsigned long Count2 = 0.0;
44
45    boolean DEBUG = false;
46
47    // print data to serial port
48    void dataPrint(unsigned long frequency){
49
50    // If you want to use the open QCM Java app, uncomment below code.
51    //  Serial.print("RAWMONITOR");
52    //  Serial.print(frequency);
53    // Serial.print("_");
54    //  Serial.print(Count2);
55    //  Serial.print("_");
```

```
56
57  // And comment this custom part when using Java
58  // Calculate frequency based on "Gate" sample time.
59    Count2 = frequency/GATE*1000.0;
60  /*The board has a 16 MHz resonator. Calculate the difference between the
61   *measured frequency and the board frequency to get the resonance frequency.*/
62    TrueFreq = (16E6-Count2);
63    Serial.print(TrueFreq);
64
65  // Serial gate allocation
66  //  Serial.write(255);  // Add this for the Java app
67    Serial.write(13); // Remove this for the Java app
68  }
69
70  void setup(){
71    Serial.begin(115200);
72    // initiate the frequency counter
73    FreqCount.begin(GATE);
74  }
75
76  void loop(){
77    // read the openQCM serial number at the connection and open connection
78    if (Serial.available()) {
79      int val = Serial.parseInt();
80      if (val == 1){
81        byte valueSeries = EEPROM.read(ADDRESS_SERIES);
82        byte valueNumberFirst = EEPROM.read(ADDRESS_NUMBERFIRST);
83        byte valueNumberSecond = EEPROM.read(ADDRESS_NUMBERSECOND);
84        Serial.print("SERIALNUMBER");
85        Serial.print(valueSeries, DEC);
86        Serial.print(valueNumberFirst, DEC);
87        Serial.print(valueNumberSecond, DEC);
88        Serial.write(255);
89      }
90    }
91
92    // read quartz crystal microbalance frequency
93    if (FreqCount.available())
94    {
95      frequency = FreqCount.read();      // measure QCM frequency
96      dataPrint(frequency); // print data
97    }
98  }
```

B.2. Matlab readout

```matlab
1   %% This script is made for readout of OpenQCM micro board with shield.
2   %% Delete old connection from previous run
3   serCheck = exist('ser');
4   if serCheck ==1
5           delete(ser); % Delete serial
6   end
7   clear
8   close all
9   clc
10
11  %% Initialize variables prepare output file
12  % Save the date
13  date = datetime('now','InputFormat','yyyy-MM-dd','Format','yyyy-MM-dd');
14  date = string(date);
15  % Declare some variables.
16  n = 1;
17  nr = 1;
18  j = 0;
19  raw = 1.000555E7;
20  time=datetime('now','InputFormat','HH:mm:ss.SSS','Format','HH:mm:ss.SSS');
21  TIME(1) = time;
22  FREQ(1) = raw;
23  ZeroTime(1) = TIME(1)-TIME(1);
24  ZeroTime.Format = 'hh:mm:ss.SSS';
25  ZeroFreq(1) = FREQ(1)-FREQ(1);
26
27  % Make file for output
28  Dir = cd;
29  name = strcat(Dir,'\Working folder\RawData',date,'_',string(nr),'.mat');
30  save(name,'TIME','ZeroTime','FREQ','ZeroFreq');
31
32  %% Initialize plot
33  x=ZeroTime;
34  y=FREQ;
35  figure(1);
36  h = plot(x,y,'b-');
37  xtickformat('hh:mm:ss.SSS');
38  h.XDataSource = 'x';
39  h.YDataSource = 'y';
40  xlabel('Time');
41  ylabel('Frequency (Hz)');
42  hold on;
43  box on;
44  grid on;
45
```

B

```matlab
46   %% Intialize serial connection to Arduino
47   % Find the right COM port, it is mostly COM3.
48   list=seriallist; % Not needed, but helps to find all open COM ports.
49   ser=serial("COM3",'Terminator','CR');
50   ser.Baudrate = 9600;
51   fopen(ser);
52   raw = fgetl(ser);
53   % Give it a little time to stabilize before going into readout loop.
54   % This makes sure you read a full serial string.
55   pause(1);
56
57   %% Readout loop
58   for i=1:100000000 % essentially until infinity
59   tic;
60   raw = fgets(ser); % Read serial data
61   % Make timestamp immediately after readout
62   time=datetime('now','InputFormat','HH:mm:ss.SSS','Format','HH:mm:ss.SSS');
63   % Store data in arrays
64   TIME(i-j) = time;
65   ZeroTime(i-j) = TIME(i-j)-TIME(1);
66   FREQ(i-j) = str2double(raw);
67   % Update plot
68   x=ZeroTime;
69   y=FREQ;
70   refreshdata;
71   drawnow;
72   % Save data
73   name=strcat(Dir,'\Working folder\RawData',date,'_',string(nr),'.mat');
74   save(name,'TIME','ZeroTime','FREQ','ZeroFreq');
75   % This loops creates new files to store a segment of the data. It cuts when
76   % the frequency is stable. This makes it easier to cut off the beginning
77   % and endings for further processing. It can also be used to terminate the
78   % loop by setting i to a higher number than the loop counter when stable.
79   if i==n*5000+1 % Change the value here to change segment size.
80       n=n+1;
81       stability=abs(mean(FREQ(i-j-99:i-j-80))-mean(FREQ(i-j-20:i-j-1)))
82       if stability<=3
83           nr=nr+1
84           j=i;
85           clear ZeroTime
86           clear TIME
87           clear FREQ
88           clear ZeroFreq
89           TIME(1) = time;
90           ZeroTime(1) = TIME(1)-TIME(1);
91           ZeroFreq(1) =0;
92           % i=100000000000000000;
93       end
```

```
94   end
95   dt(i) = toc;
96   end
97   delete(ser); % Delete serial after measurement to prevent erros.
98
99   %% This is used to plot the dt for all datapoints to see deviations
100  Timeaverage=mean(dt)
101  figure(2);
102  plot(dt);
103  xlabel('Time');
104  ylabel('Interval (s)');
105  box on;
106  grid on;
```

B

C

SIZE DETERMINATION BY THE SCHERRER METHOD

C.1. SCHERRER CALCULATIONS

The Scherrer formula, equation C.1, was used to calculate the grain size, τ, from the XRD measurements. K is the shape farctor, here assumed to be 0.89 as is common for spherical grains. λ is the X-ray wavelength, here 1.54 Å. β is the full width at half maximum of a peak and Θ is the Bragg angle (in radians). All inputs are summarized in table C.1 with the calculated grain size for the highest peak at $2\Theta = 27.64$.

$$\tau = \frac{K\lambda}{\beta cos(\Theta)} \tag{C.1}$$

Table C.1: Input and outputs used for the Scherrer equation.

Day	Θ (rad)	β (rad)	τ (nm)
Day 1	0.4824	0.0304	5.1
Day 7	0.4824	0.0291	5.3
Day 30	0.4838	0.0281	5.5

PERIODIC TABLE

Periodic Table of the Elements

1 IA 1A	2 IIA 2A											13 IIIA 3A	14 IVA 4A	15 VA 5A	16 VIA 6A	17 VIIA 7A	18 VIIIA 8A
1 **H** Hydrogen 1.008																	2 **He** Helium 4.003
3 **Li** Lithium 6.941	4 **Be** Beryllium 9.012											5 **B** Boron 10.811	6 **C** Carbon 12.011	7 **N** Nitrogen 14.007	8 **O** Oxygen 15.999	9 **F** Fluorine 18.998	10 **Ne** Neon 20.180
11 **Na** Sodium 22.990	12 **Mg** Magnesium 24.305	3 IIIB 3B	4 IVB 4B	5 VB 5B	6 VIB 6B	7 VIIB 7B	8 VIII 8	9 VIII 8	10	11 IB 1B	12 IIB 2B	13 **Al** Aluminum 26.982	14 **Si** Silicon 28.086	15 **P** Phosphorus 30.974	16 **S** Sulfur 32.066	17 **Cl** Chlorine 35.453	18 **Ar** Argon 39.948
19 **K** Potassium 39.098	20 **Ca** Calcium 40.078	21 **Sc** Scandium 44.956	22 **Ti** Titanium 47.867	23 **V** Vanadium 50.942	24 **Cr** Chromium 51.996	25 **Mn** Manganese 54.938	26 **Fe** Iron 55.845	27 **Co** Cobalt 58.933	28 **Ni** Nickel 58.693	29 **Cu** Copper 63.546	30 **Zn** Zinc 65.38	31 **Ga** Gallium 69.723	32 **Ge** Germanium 72.631	33 **As** Arsenic 74.922	34 **Se** Selenium 78.971	35 **Br** Bromine 79.904	36 **Kr** Krypton 84.798
37 **Rb** Rubidium 84.468	38 **Sr** Strontium 87.62	39 **Y** Yttrium 88.906	40 **Zr** Zirconium 91.224	41 **Nb** Niobium 92.906	42 **Mo** Molybdenum 95.95	43 **Tc** Technetium 98.907	44 **Ru** Ruthenium 101.07	45 **Rh** Rhodium 102.906	46 **Pd** Palladium 106.42	47 **Ag** Silver 107.868	48 **Cd** Cadmium 112.414	49 **In** Indium 114.818	50 **Sn** Tin 118.711	51 **Sb** Antimony 121.760	52 **Te** Tellurium 127.6	53 **I** Iodine 126.904	54 **Xe** Xenon 131.294
55 **Cs** Cesium 132.905	56 **Ba** Barium 137.328	57-71	72 **Hf** Hafnium 178.49	73 **Ta** Tantalum 180.948	74 **W** Tungsten 183.84	75 **Re** Rhenium 186.207	76 **Os** Osmium 190.23	77 **Ir** Iridium 192.217	78 **Pt** Platinum 195.085	79 **Au** Gold 196.967	80 **Hg** Mercury 200.592	81 **Tl** Thallium 204.383	82 **Pb** Lead 207.2	83 **Bi** Bismuth 208.980	84 **Po** Polonium 209.987	85 **At** Astatine 209.987	86 **Rn** Radon 222.018
87 **Fr** Francium 223.020	88 **Ra** Radium 226.025	89-103	104 **Rf** Rutherfordium [261]	105 **Db** Dubnium [262]	106 **Sg** Seaborgium [266]	107 **Bh** Bohrium [264]	108 **Hs** Hassium [269]	109 **Mt** Meitnerium [268]	110 **Ds** Darmstadtium [269]	111 **Rg** Roentgenium [272]	112 **Cn** Copernicium [277]	113 **Uut** Ununtrium unknown	114 **Fl** Flerovium [289]	115 **Uup** Ununpentium unknown	116 **Lv** Livermorium [288]	117 **Uus** Ununseptium unknown	118 **Uuo** Ununoctium unknown

Lanthanide Series

57 **La** Lanthanum 138.905	58 **Ce** Cerium 140.116	59 **Pr** Praseodymium 140.908	60 **Nd** Neodymium 144.243	61 **Pm** Promethium 144.913	62 **Sm** Samarium 150.36	63 **Eu** Europium 151.964	64 **Gd** Gadolinium 157.25	65 **Tb** Terbium 158.925	66 **Dy** Dysprosium 162.500	67 **Ho** Holmium 164.930	68 **Er** Erbium 167.259	69 **Tm** Thulium 168.934	70 **Yb** Ytterbium 173.055	71 **Lu** Lutetium 174.967

Actinide Series

89 **Ac** Actinium 227.028	90 **Th** Thorium 232.038	91 **Pa** Protactinium 231.036	92 **U** Uranium 238.029	93 **Np** Neptunium 237.048	94 **Pu** Plutonium 244.064	95 **Am** Americium 243.061	96 **Cm** Curium 247.070	97 **Bk** Berkelium 247.070	98 **Cf** Californium 251.080	99 **Es** Einsteinium [254]	100 **Fm** Fermium 257.095	101 **Md** Mendelevium 258.1	102 **No** Nobelium 259.101	103 **Lr** Lawrencium [262]

ABOUT THE AUTHOR

Hendrik Joost van Ginkel was born in Blaricum on November 17th 1993. After he graduated from the Rijnlands Lyceum in Oegstgeest in 2012, he started a B.Sc. Molecular Science & Technology at Leiden University and Delft University of Technology, during which he chose the chemical engineering track.

In 2016, he followed it up with a M.Sc. Chemical Engineering at the same faculty of Applied Science at Delft Univerisity of Technology.

During his internship, he worked at a start-up, VSParticle, through which he came in contact with prof. Andreas Schmidt-Ott, who would supervise his thesis on spark ablation for die attach materials. Joost presented his thesis work in the summer of 2018 and graduated.

His thesis work brought him in contact with students of prof. dr. Zhang of the Electronic Components, Technology & Materials (ECTM) group at the Faculty of Electrical Engineering, Mathematics and Computer Science (EEMCS) in Delft. He encouraged Joost to apply for a PhD position in his group to introduce the spark ablation printing technology to the cleanroom and investigate potential applications in microelectronics. This book is the final product of this research.

After his PhD, Joost started as quality engineer at NXP Semiconductors in Nijmegen in November of 2023.

LIST OF PUBLICATIONS

JOURNAL PUBLICATIONS

4. **H. J. van Ginkel**, L. Mitterhuber, M. W. van de Putte, M. Huijben, S. Vollebregt, and G.Q. Zhang, *Nanostructured thermoelectric films synthesised by spark ablation and their oxidation behaviour* , Nanomaterials **13(11)**, (2023).

3. **H. J. van Ginkel**, S. Vollebregt, A. Schmidt-Ott, G.Q. Zhang, *Mass and density determination of porous nanoparticle films using a quartz crystal microbalance*, Nanotechnology **33(48)**, (2022).

2. M. Shooshtari, L.N. Sacco, **H.J. van Ginkel**, S. Vollebregt, A. Salehi, *Enhancement of room temperature ethanol sensing by optimizing the density of vertically aligned carbon nanofibers decorated with gold nanoparticles*, Materials **15(4)**, (2022).

1. Z. Cui, **H. J. van Ginkel**, X. Fan, G.Q. Zhang, *The interface adhesion of $CaAlSiN_3:Eu^{2+}$ phosphor/silicone used in light-emitting diode packaging: A first principles study*, Applied Surface Science **510**, (2022).

CONFERENCE PROCEEDINGS

7. **H. J. van Ginkel**, M. Orviettani, J. Romijn, G.Q. Zhang, S. Vollebregt, *ZnO nanoparticle printing for UV sensor fabrication*, IEEE Sensors, Dallas, USA, (2022)

6. X. Ji, H. van Zeijl, J. Romijn, **H. J. van Ginkel**, X. Liu, G.Q. Zhang, *Low temperature sapphire to silicon flip chip interconnects by copper nanoparticle sintering*, IEEE 9th Electronics System-Integration Technology Conference (ESTC), Palma de Mallorca, Spain, (2022).

5. X. Ji, **H. J. van Ginkel**, D. Hu, A. Schmidt-Ott, H. van Zeijl, S. Vollebregt, G.Q. Zhang, *Patterning of fine-features in nanoporous films synthesized by spark ablation*, IEEE 22nd International Conference on Nanotechnology (NANO), Palma de Mallorca, Spain, (2022).

4. L.N. Sacco, **H. J. van Ginkel**, S. Vollebregt, *Synthesis of Carbon nanofibers (CNFs) by PECVD using Ni catalyst printed by spark ablation*, IEEE 22nd International Conference on Nanotechnology (NANO), Palma de Mallorca, Spain, (2022).

3. **H. J. van Ginkel**, J. Romijn, S. Vollebregt, G.Q. Zhang, *High step coverage interconnects by printed nanoparticles*, 23rd European Microelectronics and Packaging Conference & Exhibition (EMPC), Gothenburg, Sweden, (2021).

2. H. Avdogmus, **H. J. van Ginkel**, A.D. Galiti, M. Hu, J.P. Frimat, A. van den Maagdenberg, G.Q. Zhang, M. Mastrangeli, P.M. Sarro, *Dual-gate fet-based charge sensor enhanced by in-situ electrode decoration in a MEMS organs-on-chip platform*, 21st International Conference on Solid-State Sensors, Actuators and Microsystems (Transducers), Orlando, USA, (2021).

1. **H. J. van Ginkel**, P. Roels, M.F.J. Boeie, T.V. Pfeiffer, S. Vollebregt, G.Q. Zhang, A. Schmidt-Ott, *3D-impaction printing of porous layers*, European Aerosol Conference, Aachen, Germany, (2020).